

# **Reconstructing paleo-oxygenation in the Arabian Sea over the last 50 ka**

A thesis submitted in partial fulfilment of the requirements  
for the degree of

**Doctor of Philosophy**

by

**Deepak Kumar Rai**

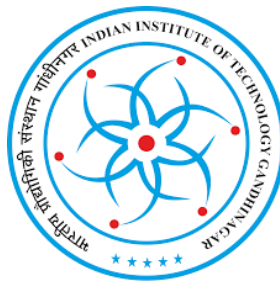
(Roll No. 18330009)

Under the supervision of

**Dr. Arvind Singh**

Geosciences Division

Physical Research Laboratory, Ahmedabad, India



Discipline of Earth Sciences  
Indian Institute of Technology Gandhinagar, India  
2024



*Dedicated to  
my Parents*



# Declaration

I, Deepak Kumar Rai, declare that this thesis report represents my own ideas written, and where others' ideas or words have been included, I have adequately cited and referenced the original sources. I also declare that I have followed all principles of academic honesty and integrity and have not misrepresented, fabricated or falsified any idea/fact/source in my submission. I understand that any violation of the above can cause disciplinary action by the Institute and can also evoke penal action from the sources which have thus not been properly cited or from whom proper permission has not been taken when needed.

**Date:**

Deepak Kumar Rai

(Roll No.: 18330009)





**Discipline of Earth Sciences**

**Indian Institute of Technology, Gandhinagar**

***Gandhinagar, Gujarat - 382355***

---

## **CERTIFICATE**

It is certified that the work contained in the thesis titled **“Reconstructing paleo-oxygenation in the Arabian Sea over the last 50 ka”** by **Mr. Deepak Kumar Rai** (Roll no: 18330009) has been carried out under my supervision and that this work has not been submitted elsewhere for a degree. I have read this dissertation, and I believe it is fully adequate, in scope and quality, for the degree of Doctor of Philosophy.

Dr. Arvind Singh  
(Thesis Supervisor)  
Geosciences Division,  
Physical Research Laboratory,  
Ahmedabad, India



# Acknowledgements

*Completing this PhD has been an incredible journey, filled with challenges, personal growth, and invaluable support from so many people. Reflecting on this journey, I'm reminded of Helen Keller's words: "Alone, we can do so little; together, we can do so much."*

*First and foremost, my deepest gratitude goes to my PhD supervisor, Dr. Arvind Singh. His outstanding guidance, scientific insight, and steadfast support have been the cornerstones of my research. His ability to identify my strengths and areas for improvement early on was crucial in expanding my research horizons and nurturing my scientific curiosity. Additionally, I want to thank Pallavi Ma'am for her warm hospitality and Ira for her cheerful spirit, which brought much-needed comfort and positivity during my visits.*

*I am deeply thankful to my doctoral committee members: Prof. Sanjeev Kumar, Prof. Lokesh Kumar Sahu, and Dr. Megha Upendra Bhatt. Their insightful suggestions and invaluable feedback were essential in refining and enhancing the quality of my work. My sincere thanks also go to Prof. Sanjeev Kumar, Prof. J S Ray, Prof. Ravi Bhushan, and Dr. Yogita Kadlag for providing crucial lab facilities. The stimulating discussions with Dr. Kaustubh Thirumalai, Dr. Babette Hoogakker, and the faculty of the Geosciences division greatly enriched my research.*

*A special mention must be made of Mr. Jitender Kumar, Mrs. Sangeeta Verma, Mr. Ankur Dabhi, Mr. A Shivam, Mr. Mahesh Gaddam, Mr. Rohit Meena, and Lakhan Bhai. Their expertise in instrument handling and our many discussions were instrumental in broadening the scope of my research and successfully executing my experiments. I am also grateful to Mrs. Jaldhi Mehta, Mr. Pradeep Chauhan, and Mr. Saurav Suman for their efficient handling of official processes, which allowed me to concentrate on my research.*

*I owe a debt of gratitude to Dr. Amit Pandey, Dr. Himanshu Saxena, and Dr. Milan Kumar Mahala for their unwavering motivation during the thesis-writing phase. I am also thankful to Ms. Shreya Mehta and Dr. Abul Qasim for their meticulous proofreading, which greatly enhanced the quality of my thesis.*

*I feel fortunate to have the support of wonderful friends: Amit, Yash, Sandeep, Naval, Yogesh, Vikas, Sunil, Siddhartha, Monika, and Deva. Your companionship and support were vital in lightening the emotional burden of this PhD journey. Special thanks also go to my senior-cum-friends: Himanshu, Atif, Abdur, Partha, Ankit, Abhay, Sushant, Niharika Di, and Kiran Bhaiya, as well as my junior-cum-friends: Nazir, Ajayeta, Swagatika, Shreya, Aakash, Ranjan, Goldy, Kamran, and Debashish. My college friends Amit, Shraddha, Arvind, and Ashish have been a constant source of encouragement. Ralph Waldo Emerson captures this perfectly: "The glory of friendship is not the outstretched hand, nor the kindly smile, nor the joy of companionship; it is the spiritual inspiration that comes to one when they discover that someone else believes in them and is willing to trust them with their friendship."*

*As I reflect on my PhD journey, I remember the many ups and downs, especially during the COVID-19 pandemic. This period was filled with uncertainties in life and in my academic pursuits, making it a physically and emotionally taxing time. Yet, it also strengthened my resolve and determination to persevere and complete this thesis.*

*My family has been my unwavering pillar of strength throughout this journey. Their constant support and belief in me were crucial, especially during the toughest times. I am deeply grateful to my parents for their endless encouragement and love. As Michael J. Fox rightly said, "Family is not an important thing. It's everything."*

*This thesis stands as a testament to the collective efforts and support of all these wonderful people and this organization. Each of you has played a vital role in this journey, and for that, I am deeply thankful.*

**Deepak Kumar Rai**

# Abstract

Oxygen (O<sub>2</sub>) is undoubtedly an essential element for all kinds of life. In geological timescales, the ocean has played a pivotal role in oxygenating the Earth's atmosphere. However, in the last fifty years, there has been a concerning decline in the dissolved O<sub>2</sub> content within both open ocean waters and coastal seas. This decline, known as ocean deoxygenation, poses a significant threat to marine ecosystems and the biogeochemical cycling of elements, particularly nitrogen. Nitrogen (N<sub>2</sub>) is fundamental to all living organisms, with its bioavailable forms, such as nitrate and ammonium, being scarce in the sunlit ocean. This scarcity creates a substantial nutritional limitation within marine ecosystems, affecting the overall health and balance of these intricate systems.

Anthropogenically driven global warming is widely recognized as the primary cause of ongoing ocean deoxygenation. This warming trend is expected to intensify denitrification, removing bioavailable nitrogen from the ocean and producing nitrous oxide—a potent greenhouse gas—by expanding oxygen minimum zones (OMZs) and altering nitrate supply routes through changes in ocean circulation. Robust future projections across various climatic scenarios are essential for effective ecosystem management. While the predictions of the current climate models generally align with observations of oceanic dissolved O<sub>2</sub> loss, they only capture about half of the observed decline and exhibit discrepancies in defining the extent of OMZs, challenging the reliability of future predictions. Basin-wide studies of OMZ changes in response to climate variability across different time scales are essential to assess potential intensification. Additionally, the relatively short observational history of oceanic nitrate concentrations compared to the residence time of bioavailable nitrogen limits the detection of climatic trends. In contrast, geological records offer detailed accounts of climate fluctuations, such as glacial-interglacial cycles. Reconstructing past dissolved O<sub>2</sub> levels alongside the nitrogen cycle may provide a comprehensive understanding of variations in dissolved O<sub>2</sub> concentration and its impacts on the nitrogen cycle under different climate scenarios.

The Arabian Sea hosts one of the most intense and perennial OMZ. This OMZ arises from poor ventilation and high surface productivity, resulting in increased respiration rates in the intermediate waters. While surface hydrography changes driven by monsoons govern productivity patterns in the Arabian Sea, alterations in global overturning circulations affect

the thermocline waters. Unlike many other open-ocean OMZs, the Arabian Sea OMZ is particularly noteworthy as it forms in the relatively oligotrophic central-eastern region, away from the highly productive upwelling area along the Oman-Somalia coast. This OMZ in the Arabian Sea accounts for at least one-third of the global marine fixed nitrogen loss. Over decadal to millennial timescales, significant fluctuations in the intensity of the OMZ have been observed, correlating with global climate change. However, the precise mechanisms through which atmospheric and deep-ocean circulations influence the Arabian Sea OMZ across different temporal and spatial scales remain poorly understood.

The iodine to calcium (I/Ca) ratios in planktic foraminifera have emerged as a promising proxy for inferring changes in subsurface dissolved O<sub>2</sub> levels in the ocean. This proxy relies on the redox behavior of iodine in seawater. Although a limited number of core-top calibration studies indicate that higher I/Ca ratios in planktic foraminifera qualitatively correspond to higher dissolved O<sub>2</sub> concentrations in subsurface waters, there has been no regional calibration conducted for the northern Indian Ocean. To address this gap and evaluate the effectiveness of the proxy in this region, we have measured I/Ca ratios on foraminifera tests collected from plankton tows and core-top sediments. We compared the core-top I/Ca values and modern-day dissolved O<sub>2</sub> data from climatological datasets. Our findings reveal that the I/Ca ratios of plankton tow foraminifera are notably low, suggesting low O<sub>2</sub> levels in the water column. This observation is consistent with equally low I/Ca ratios observed in core-top foraminifera samples, even when they may represent different time periods than the plankton tow samples. The agreement between core-top I/Ca values and modern dissolved O<sub>2</sub> data indicates that this proxy effectively captures subsurface O<sub>2</sub> signals. As such, it can be used confidently to reconstruct past dissolved O<sub>2</sub> levels, providing valuable insights into past O<sub>2</sub> variability.

To comprehensively understand dissolved O<sub>2</sub> variations in the Arabian Sea over geological timescales, we generated two new records of I/Ca in planktic foraminifera, along with Mg/Ca ratios and total organic carbon content, and its isotopic composition from sediment cores obtained from northern and southeastern Arabian Sea. Bulk sedimentary δ<sup>15</sup>N was also measured to infer about the paleo nitrogen cycle in this region.

Our observations revealed low O<sub>2</sub> conditions in the northern and southeastern Arabian Sea until the Last Glacial Maxima (LGM). After LGM, O<sub>2</sub> concentrations in both regions gradually increase until Younger Dryas (YD), followed by a decreasing trend in the Holocene.

The dissolved O<sub>2</sub> increase beyond LGM during deglaciation is higher in the southeastern Arabian Sea compared to the northern region, with values >100 μmol kg<sup>-1</sup> in the water column, suggesting a well-oxygenated water column during YD.

The lower dissolved O<sub>2</sub> levels during the glacials are probably due to enhanced primary productivity owing to strengthened winter monsoon-driven convective mixing and increased input of bioavailable nutrients from dust inputs. During this time, high primary productivity-driven O<sub>2</sub> consumption in the intermediate depths was the predominant factor in determining the deoxygenated conditions in the northern and southeastern Arabian Sea. This low O<sub>2</sub> period is accompanied by higher denitrification and high nitrogen fixation rates. The increasing O<sub>2</sub> trend in the deglaciation period is due to the lower primary productivity and intense ventilation of the intermediate waters from southern sourced waters (e.g., Antarctic Intermediate Water). High dissolved O<sub>2</sub> during YD is possibly due to the reduced surface primary productivity and higher subsurface ventilation by the intermediate water masses from the adjacent Red Sea, Persian Gulf, and southern sourced water masses. An increase in the O<sub>2</sub> concentration during this time also supported reduced or absence of denitrification. During the early Holocene, the gradual decrease in the dissolved O<sub>2</sub> levels is best explained by the reduction of ventilation from the southern sources of water masses, along with a prominent role of warmer temperature-related solubility decrease of O<sub>2</sub>. Denitrification in the water column also intensifies during the early Holocene.

This thesis provides a new outlook on the oxygenation changes in the Arabian Sea in the geological past and its impact on the paleo nitrogen cycle. It also emphasises that temperature-related solubility changes, as previously thought, might not always be the dominant factor in controlling dissolved O<sub>2</sub> concentration in the ocean. Our analysis might be insightful for biogeochemical models to explain the future ocean oxygen trends.

**Keywords:** Dissolved oxygen, Ocean deoxygenation, Paleo nitrogen cycle, Oxygen minimum Zone, Arabian Sea, Iodine to Calcium ratios.



# Contents

<b>Abstract</b> .....	i
<b>Contents</b> .....	v
<b>List of Tables</b> .....	ix
<b>List of Figures</b> .....	xi
<b>List of Abbreviations</b> .....	xv
<b>1 Introduction</b> .....	1
1.1 Background.....	1
1.2 Vertical distribution of dissolved oxygen in the ocean .....	2
1.3 Ocean deoxygenation and its causes .....	4
1.4 Nitrogen cycling in the oxygen minimum zones .....	5
1.5 Consequences of ocean deoxygenation .....	7
1.6 Implication to future projections .....	8
1.7 Proxies .....	10
1.7.1 Bulk sedimentary $\delta^{15}\text{N}$ .....	10
1.7.2 Iodine to Calcium ratios in planktic foraminifera .....	12
1.8 Oxygen minimum zone in the Arabian Sea .....	14
1.9 Previous Studies in the Arabian Sea.....	17
1.10 Scope of the present work .....	18
<b>2 Materials and Methods</b> .....	21
2.1 Sample locations .....	21
2.1.1 Deep-sea sediment cores.....	21
2.1.2 Core-top sediment samples .....	21
2.1.3 Multi plankton net (MPN) samples .....	23
2.2 Oceanographic conditions in the study area .....	24
2.2.1 The Arabian Sea .....	24

2.2.2	The Bay of Bengal.....	25
2.2.3	The Andaman Sea .....	25
2.3	Separation of foraminifera tests from bulk marine sediments .....	26
2.4	Description of Planktic foraminifera .....	27
2.5	Radiocarbon dating.....	28
2.6	Elemental and isotopic analysis of Total Organic Carbon and Total Nitrogen .....	32
2.6.1	Sample processing:.....	32
2.6.2	$\delta^{15}\text{N}$ and $\delta^{13}\text{C}_{\text{org}}$ measurements of the bulk sediments .....	33
2.6.3	TOC and TN concentration measurement .....	34
2.7	Element/Calcium ratio measurement on foraminiferal test .....	34
2.7.1	Reagents and labware .....	35
2.7.2	I/Ca and multi-element/Ca standard preparation .....	35
2.7.3	Mass spectrometry.....	36
2.7.4	Cleaning procedure for foraminifera tests .....	38
2.7.5	Foraminifera sample analysis.....	39
2.7.6	Analytical precision and accuracy.....	41
<b>3</b>	<b>Proxy validation of iodine to calcium ratios from plankton tow and core-top foraminifera .....</b>	<b>43</b>
3.1	Introduction.....	43
3.2	Methods .....	45
3.3	Results.....	46
3.3.1	Plankton tow and core-top planktic foraminifera I/Ca .....	46
3.3.2	Core-top I/Ca vs Oxygen concentration .....	48
3.4	Discussion .....	49
3.5	Conclusion .....	51
<b>4</b>	<b>Glacial – interglacial subsurface oxygen variability in the Arabian Sea .....</b>	<b>53</b>
4.1	Introduction.....	53

4.2	Materials and Methods .....	55
4.3	Results.....	57
4.3.1	Chronology and Sedimentation Rate.....	57
4.3.2	Foraminiferal I/Ca variations .....	59
4.3.3	Temperature reconstruction .....	62
4.3.4	Total organic carbon (TOC) variations .....	62
4.4	Discussions .....	62
4.4.1	Oxygen variability during the glacial period .....	62
4.4.2	Oxygen variability during the deglaciation .....	65
4.4.3	Oxygen variability during the early Holocene .....	66
4.5	Conclusion .....	67
<b>5</b>	<b>Paleo-nitrogen cycling in the Arabian Sea .....</b>	<b>69</b>
5.1	Introduction.....	69
5.2	Material and Methods.....	71
5.3	Results.....	71
5.3.1	Variations in $\delta^{13}\text{C}_{\text{org}}$ , and TOC (wt. %)... ..	71
5.3.2	Variations in $\delta^{15}\text{N}$ , and TN (wt %)... ..	71
5.4	Discussion .....	72
5.4.1	No Influence of Terrestrial Organic Input and Diagenetic Changes on $\delta^{15}\text{N}$ ....	72
5.4.2	Nitrogen cycling during the glacial period .....	77
5.4.3	Nitrogen cycling during the deglaciation .....	79
5.4.4	Nitrogen cycling during the early Holocene .....	79
5.4.5	Comparison with previous studies in the Arabian Sea .....	79
5.5	Conclusion .....	82
<b>6</b>	<b>Summary, limitations, and scope for future works .....</b>	<b>83</b>
6.1	Summary.....	83

6.1.1	Proxy validation of iodine to calcium ratios from plankton tow and core-top foraminifera .....	83
6.1.2	Glacial – interglacial subsurface oxygen variability in the Arabian Sea.....	84
6.1.3	Paleo-nitrogen cycling in the Arabian Sea .....	84
6.2	Limitations .....	84
6.3	Scope for future works.....	85
<b>References</b>	.....	<b>87</b>
<b>List of Publications</b>	.....	<b>109</b>
<b>Presentations at Conferences</b>	.....	<b>109</b>

# List of Tables

<b>Table 1.1:</b> The Typical values of oxygen in different oceans. O <sub>2</sub> data from World Ocean Atlas 2018. ....	3
<b>Table 1.2:</b> Reduction potential and redox couples of various elements. The reduction potential values are from Lu et al. (2010). ....	13
<b>Table 2.1:</b> Details of the sediment cores studied in the present work. ....	21
<b>Table 2.2:</b> Details of the core-top sediments from the northern Indian Ocean ....	22
<b>Table 2.3:</b> Details of the locations of multi-plankton net (MPN) Samples.....	23
<b>Table 2.4:</b> ICP-MS settings for measuring Me/Ca and I/Ca. ....	37
<b>Table 2.5:</b> ICP-MS method for Me/Ca analysis in 2% HNO <sub>3</sub> medium. ....	38
<b>Table 2.6:</b> ICP-MS method for I/Ca analysis in basic medium (2 % HNO <sub>3</sub> + 1 % NH <sub>4</sub> OH). ....	38
<b>Table 2.7:</b> Long-term analytical precision of internal consistency standards for Me/Ca in 2% HNO <sub>3</sub> medium.....	41
<b>Table 2.8:</b> Long-term analytical precision of internal consistency standards for I/Ca in basic medium (2 % HNO <sub>3</sub> + 1 % NH <sub>4</sub> OH).....	41
<b>Table 2.9:</b> Mg/Ca ratios of an international standard measured with samples. ....	42
<b>Table 3.1:</b> I/Ca values of the plankton tow derived planktic foraminifera. ....	47
<b>Table 3.2:</b> I/Ca values of the planktic foraminifera from the core-top sediments.....	48
<b>Table 4.1:</b> Radiocarbon age, calibrated age range, and median age of SK-364/03 sediment core. ....	58
<b>Table 4.2:</b> Radiocarbon age, calibrated age range, and median age of SK-364/13 sediment core. ....	59



# List of Figures

- Figure 1.1:** Schematic representation of expanding oxygen minimum zones (in white colour) due to warming-induced changes in the ocean. Modified after Stramma et al. (2010).....5
- Figure 1.2:** Schematic of the marine nitrogen cycle. Modified after Casciotti (2016).....6
- Figure 1.3:** Schematic of the processes in the nitrogen cycle typically recorded in  $\delta^{15}\text{N}$  of marine sediments. The average isotopic enrichment factors (shown in ‰ units) for individual processes are mentioned. The light green shaded region shows a suboxic water column. Figure Redrawn after Robinson et al. (2012)..... 12
- Figure 1.4:** Schematic representation of  $\text{IO}_3^-$  incorporation in planktic foraminifera in different dissolved  $\text{O}_2$  concentration levels. The gradient in blue colour shows the transition from the surface ocean (light colour) to the subsurface (darker colour). ..... 14
- Figure 1.5:** (a) Climatological (2002-2023) summer chlorophyll-a concentration ( $\text{mg m}^{-3}$ ): (b) Climatological (2002-2023) winter chlorophyll-a concentration ( $\text{mg m}^{-3}$ ). Bold arrows represent the wind direction and dashed lines represent the surface circulation directions during the different monsoon seasons. WICC is West India Coastal Current. Chlorophyll-a data source: Aqua/MODIS from 2002 to 2023. .... 16
- Figure 1.6:** Intermediate water masses in the Arabian Sea, superimposed over climatological dissolved  $\text{O}_2$  concentration at 300 m depth. The black dashed curve represents the present-day denitrification zone. Dissolved  $\text{O}_2$  data are taken from World Ocean Atlas 2018. RSW – Red Sea Water, PGW – Persian Gulf Water, ICW – Indian Central Water. .... 17
- Figure 2.1:** Locations of the different types of samples used in the present study superimposed over dissolved  $\text{O}_2$  concentration at 300 m depth. Data source of dissolved  $\text{O}_2$  – World Ocean Atlas 2018. Dissolved  $\text{O}_2$  data is climatological data.....22
- Figure 2.2:** Spade corer (left) and multi plankton net (right) operation onboard ORV *Sagar Kanya* 373 and 374. (Photo Credit: Deepak Kumar Rai). .....23
- Figure 2.3:** Photograph of foraminifera samples under a zoom-type stereo microscope (Photo Credit: Deepak Kumar Rai). .....26

<b>Figure 2.4:</b> Photograph of AMS facility at Physical Research Laboratory, Ahmedabad, India (top). Schematic of the PRL–AURiS (bottom) (Bhushan et al., 2019). .....	31
<b>Figure 2.5:</b> Photograph of Flash 2000 elemental analyzer interfaced with Delta V IRMS through Conflo IV at GeoSIL, PRL, Ahmedabad, India (Photo Credit: Deepak Kumar Rai).32	
<b>Figure 2.6:</b> Thermo® Element XR (HR-ICP-MS) at PRL, Ahmedabad, India used for trace elemental analysis in this study (Photo Credit: Deepak Kumar Rai). .....	35
<b>Figure 2.7:</b> Correlation plots of (a,d) Mg/Ca with Al/Ca; (b,f) Mg/Ca with Fe/Ca; and (c,e) Mg/Ca with Mn/Ca of SK-364/03, and SK-364/13, respectively. Coefficient of variation ( $R^2$ ) and number of samples (n) are shown in each panel. None of the positive correlations are significant at $p < 0.05$ - suggesting effective cleaning of tests. ....	40
<b>Figure 3.1:</b> Map showing the sample locations of the core-top and plankton tow samples superimposed over dissolved $O_2$ concentrations at 300 m depth. The data source for dissolved $O_2$ is World Ocean Atlas 2018. ....	45
<b>Figure 3.2:</b> Plot showing I/Ca ( $\mu\text{mol mol}^{-1}$ ) ratios in plankton tow and core-top foraminifera. ....	47
<b>Figure 3.3:</b> Correlation plot of I/Ca vs minimum oxygen concentration in the water column. The dissolved oxygen data is from World Ocean Atlas 2018. Red squares represent I/Ca data acquired in this study. Blue circles are literature data (Lu et al., 2020; Lu et al., 2016; Winkelbauer, 2022) .....	49
<b>Figure 3.4:</b> Plot of offset of I/Ca ( $\mu\text{mol mol}^{-1}$ ) ratios between core-top and plankton tow foraminifera with depth.....	51
<b>Figure 4.1:</b> Map showing the core locations used in this study superimposed over the climatological dissolved oxygen ( $O_2$ ) concentration at 300 m depth. The Black curve shows the present-day oxygen-deficient zone in the Arabian Sea. Dissolved $O_2$ data taken from World Ocean Atlas 2018. ....	55
<b>Figure 4.2:</b> Vertical profile of dissolved $O_2$ at the core locations. The dark green curve is for the northern Arabian Sea core (SK-364/03), and the dark blue curve represents dissolved $O_2$	

concentrations at the southeastern core location (SK-364/13). Please note the break in the y-axis.....57

**Figure 4.3:** Age-depth model of (a) SK-364/03, and (b) SK-364/13. The upper panels show Markov Chain Monte – Carlo iteration history (left), prior (green lines), posterior (grey histograms), density functions for accumulation rate (middle), and memory (right). The lower panel shows the age-depth model with calibrated  $^{14}\text{C}$  dates in blue. The red line shows the modelled mean age at 95 % confidence interval (grey dotted lines)..... 60

**Figure 4.4:** Sedimentation rate estimated using the data obtained from (a) SK-364/03, and (b) SK-364/13. .... 61

**Figure 4.5:** Temporal variations of (a) I/Ca measured in *Trilobatus sacculifer*; Violet and green dashed horizontal lines indicates I/Ca values corresponding to  $100 \mu\text{mol kg}^{-1}$  and  $7 \mu\text{mol kg}^{-1}$  dissolved  $\text{O}_2$  concentrations, respectively; (b) temperature reconstructed from Mg/Ca measurements in *Trilobatus sacculifer*; filled circles show the data point, and the superimposed curves show the three-point running average; and (c) total organic carbon (TOC) contents. .64

**Figure 5.1:** Temporal variations of (a)  $\delta^{15}\text{N}$  in the bulk sediments; (b)  $\delta^{13}\text{C}_{\text{org}}$  of the total organic carbon in the sediments; (c) total nitrogen (TN) content; and (d) total organic carbon (TOC) content in SK-364/03 (northern Arabian Sea). .... 73

**Figure 5.2:** Temporal variations of (a)  $\delta^{15}\text{N}$  in the bulk sediments; (b)  $\delta^{13}\text{C}_{\text{org}}$  of the total organic carbon in the sediments; (c) total nitrogen (TN) content; and, (d) total organic carbon (TOC) contents in SK-364/13 (southeastern Arabian Sea)..... 74

**Figure 5.3:** Correlation plots of (a)  $\delta^{15}\text{N}$  with TN (wt. %); and (b)  $\delta^{15}\text{N}$  with TOC (wt. %) in the sediment core SK-364/03. Different colours show data points belonging to four different times periods viz. the early Holocene, deglaciation, the last glacial maximum, and those before LGM. .... 75

**Figure 5.4:** Correlations plots of (a)  $\delta^{15}\text{N}$  with TN (wt. %); and (b)  $\delta^{15}\text{N}$  with TOC (wt. %) in the sediment core SK-364/13. Different colours show data points belonging to four different time periods viz. the early Holocene, deglaciation, the last glacial maximum, and those before LGM. .... 76

**Figure 5.5:** Temporal variations of (a) bulk sediments  $\delta^{15}\text{N}$ ; filled symbols (squares and triangles) show the data point, and the superimposed curves show the three-point running average; (b) I/Ca measured in *Trilobatus sacculifer*; Purple and green dashed horizontal lines indicate I/Ca values corresponding to 100  $\mu\text{mol kg}^{-1}$  and 7  $\mu\text{mol kg}^{-1}$  dissolved  $\text{O}_2$  concentrations, respectively; and (c) total organic carbon (TOC) contents.....78

**Figure 5.6:** Map showing the locations of the sediment cores discussed. SK-364/03 & SK-364/13 (this study); MD-04-2876 (Pichevin et al. (2007)); SK177/GC-08 (Banakar et al. (2005)); SK177/11 (Kao et al. (2015)). .....80

**Figure 5.7:** Comparison of our  $\delta^{15}\text{N}$  with other records from the basin.  $\delta^{15}\text{N}$  records are arranged longitudinally with the northernmost record on top. H1, H2 and H3 are the Heinrich events. YD is the Younger Dryas event, and LGM is the Last Glacial Maxima. ....81

# List of Abbreviations

<b>Anammox</b>	Anaerobic ammonium oxidation
<b>AAIW</b>	Antarctic Intermediate Water
<b>BP</b>	Before Present
<b>CO<sub>2</sub></b>	Carbon dioxide
<b>CTD</b>	Conductivity temperature depth
<b>EA</b>	Elemental Analyzer
<b>IAEA</b>	International atomic energy agency
<b>IRMS</b>	Isotope ratio mass spectrometer
<b>LGM</b>	Last Glacial Maxima
<b>N</b>	Nitrogen
<b>NH<sub>4</sub><sup>+</sup></b>	Ammonium
<b>NO<sub>3</sub><sup>-</sup></b>	Nitrate
<b>NO<sub>2</sub><sup>-</sup></b>	Nitrite
<b>NO</b>	Nitric oxide
<b>N<sub>2</sub>O</b>	Nitrous oxide
<b>Me</b>	Multi-element
<b>O<sub>2</sub></b>	Oxygen
<b>OMZ</b>	Oxygen minimum zone
<b>TOC</b>	Total organic carbon
<b>TN</b>	Total nitrogen
<b>YD</b>	Younger Dryas
<b>V-PDB</b>	Vienna-Pee Dee Belemnite

$\delta^{13}\text{C}_{\text{org}}$	Carbon isotopic composition of TOC with V-PDB as standard
$\delta^{15}\text{N}$	Nitrogen isotopic composition with air as standard
%	Percent
‰	Per mil (or parts per thousand)
$\mu$	Micro
$\sigma$	Standard deviation
mg	Milli gram
g	Gram
kg	Kilogram
ka	Kilo annum
yr	Year
ml	Milli liter
$\mu\text{l}$	Micro liter
mm	Milli meter
m	Meter
km	Kilo meter
s	Second
M	Molarity/ molar concentration
Wt.	Weight percent

# Chapter 1

## Introduction

### 1.1 Background

Oxygen (O<sub>2</sub>) is fundamental for all life forms. O<sub>2</sub> is mainly produced through photosynthesis, utilising water and carbon dioxide (CO<sub>2</sub>) in the presence of sunlight to synthesize organic matter by autotrophs. After the formation of the Earth, for nearly 2 billion years, there was negligible O<sub>2</sub> present in our atmosphere. Photoautotrophs evolved around 3.5 billion years ago, at a time when the ocean was primarily anoxic. For more than a billion years, O<sub>2</sub> content remained very low (< 4 %) in the atmosphere (Holland, 2006). During the Great Oxidation Event, around 2.4 – 2.1 billion years ago in the paleo Proterozoic, the Earth's atmosphere and shallow ocean first experienced a rise in O<sub>2</sub> (Lyons et al., 2014). Around 0.85 billion years ago when O<sub>2</sub> concentration began to rise significantly in the atmosphere, it contributed to the biodiversity observed during the Phanerozoic. However, the deep ocean remained largely anoxic till 0.6 billion years ago (Canfield, 2015; Holland, 2006). By the end of the Carboniferous, O<sub>2</sub> constituted around 35 % of air presented in our atmosphere, much higher than its present-day level of 21 %. After this period, many large-scale anoxic events occurred in the deep ocean during the Mesozoic (252-66 million years ago), induced by alterations in climate and deep-water circulation (Jenkyns, 2010). However, it is still unclear why O<sub>2</sub> should have grown prevalent on the Earth. Furthermore, the mechanisms governing O<sub>2</sub> at the current level remain insufficiently understood. The present and past O<sub>2</sub> cycle can at least help us clarify a few fundamental ideas about O<sub>2</sub> generation and loss, and help us to predict its future. Among the most fascinating tales in Earth's history are the rise of O<sub>2</sub> to near-modern levels in the ocean and atmosphere two billion years after it first increased in the atmosphere, its gradual accumulation in the ocean, and its causal relationship with ocean circulation and marine life. Therefore, it is imperative to understand the role of the ocean in producing and regulating O<sub>2</sub> in great detail.

## 1.2 Vertical distribution of dissolved oxygen in the ocean

O<sub>2</sub> production in the ocean occurs mainly in the euphotic layer (depth in the ocean up to where 1 % of the surface sunlight irradiance reaches) through photosynthesis by phytoplankton (Falkowski & Raven, 2007). In this layer, the dissolution of O<sub>2</sub> in the ocean takes place through gas exchange with the atmosphere, driven by differences in O<sub>2</sub> concentration between the atmosphere, and the surface ocean (Garcia & Gordon, 1992). Factors like temperature, wind speed, and wave action influence the rate of gas exchange. Cold water can hold more dissolved oxygen than warm water, so colder regions tend to have higher O<sub>2</sub> concentrations. O<sub>2</sub> can be released in this layer through diffusion and mixing, as well as through breakdown of organic matter. In the intermediate depths (~100-1000 m), the prevalent O<sub>2</sub> respiration through decomposition of sinking organic detritus or bacterial/heterotrophic activities leads to decline in the dissolved O<sub>2</sub> concentration. These zones (~100-1000 m) are known as oxygen minimum zones (OMZ) (Suess, 1980).

If the ocean was fully stagnant and stratified, the exchange of atmospheric O<sub>2</sub> will be restricted to the surface ocean, hence it will subsequently result in complete anoxic conditions in the deeper waters. However, the intermediate and deep ocean is effectively ventilated by water masses usually formed in the polar regions, which are driven by the densification of surface waters due to cooling and increased salinity resulting from evaporation and sea-ice formation. The deep-water masses are usually formed in the North Atlantic (North Atlantic Deep Water) (Dickson & Brown, 1994), and the Southern Ocean (Antarctic Bottom Water) (van Heuven et al., 2011). Additionally, the intermediate depth receives similarly formed water masses near the Polar Front in the southern hemisphere (Antarctic Intermediate Water, Subantarctic Mode Water) (Karstensen & Tomczak, 1997; McCartney & Talley, 1982) and, to a lesser extent, in the marginal seas such as the Red Sea and the Persian Gulf.

The subsurface O<sub>2</sub> supply, driven by the advection of intermediate water masses, compensates for O<sub>2</sub> consumption (McCartney & Talley, 1982; Sverdrup, 1938). However, the balance between the O<sub>2</sub> consumption and the subsurface O<sub>2</sub> supply varies spatially, and is primarily influenced by the temperature and the availability of organic matter. Regions experiencing upwelling-induced high primary productivity exports more organic matter to the deep sea from the surface. In such regions, O<sub>2</sub> consumption surpasses the intermediate ventilation, resulting in the formation of OMZs at intermediate depths (Rixen et al., 2020). Deep sea maintains well-oxygenated conditions due to its high initial O<sub>2</sub> content and low O<sub>2</sub>

demand, while near-surface concentrations remain high due to production in the euphotic zone and air-sea gas exchange. Consequently, a zone of relatively low dissolved O<sub>2</sub> concentrations forms at mid-depths (Diaz & Rosenberg, 2008; Paulmier & Ruiz-Pino, 2009). The vertical distribution of O<sub>2</sub> varies in different oceans, and its typical values are provided in **Table 1.1**.

**Table 1.1:** The Typical values of oxygen in different oceans. O<sub>2</sub> data from World Ocean Atlas 2018.

Ocean	Region/ Depth	Oxygen level (μmol/kg)
Atlantic Ocean	Surface	~ 200 - 310
	Deep	~ 240 - 260
	OMZ	~ 60 - 100
Pacific Ocean	Surface	~ 180 - 300
	Deep	~ 140 - 200
	Eastern tropical north OMZ	<20
	Eastern tropical south OMZ	< 20
Indian Ocean	Surface	~ 200 - 280
	Deep	~ 160 - 190
	Arabian Sea OMZ	<10
	Bay of Bengal OMZ	< 20
Southern Ocean	Surface	~ 260 - 340
	Deep	~ 210 - 260

### 1.3 Ocean deoxygenation and its causes

Ocean deoxygenation refers to the reduction of the dissolved O<sub>2</sub> concentration in the different parts of the ocean. Ocean deoxygenation is one of the most significant changes occurring in oceanic ecosystems in the past few decades (Keeling et al., 2010; Rabalais et al., 2014). It has been observed that the dissolved O<sub>2</sub> content of the ocean has decreased in the past five decades (Keeling et al., 2010; Stramma et al., 2010). Throughout the Earth's history, major extinction events have been linked to warm climates and oxygen-deficient ocean (Norris et al., 2013). Should the present warming trend persist, human activities might lead to widespread O<sub>2</sub> deficiency in the ocean within the next millennium (Watson, 2016).

Consistent decline in the subsurface O<sub>2</sub> concentrations has been observed in the last five decades in the open ocean, particularly within or near OMZs, at a rate of up to 0.34 μmol kg<sup>-1</sup> yr<sup>-1</sup> (Helm et al., 2011; Stramma et al., 2008). This decline has led to an estimated loss of 2% or 4.8 ± 2.1 Pmol (1 Pmol = 10<sup>15</sup> mol) from the ocean's total O<sub>2</sub> content (227.4 Pmol) (Schmidtko et al., 2017). However, the extent of O<sub>2</sub> loss varies geographically. The higher loss rates, around 0.210 ± 0.125 Pmol decade<sup>-1</sup>, are observed in the equatorial Pacific, followed by the North Pacific at 0.173 ± 0.040 Pmol decade<sup>-1</sup>. The Arabian Sea and the Bay of Bengal combined show a low O<sub>2</sub> loss rate of less than 0.055 Pmol decade<sup>-1</sup>, likely due to differences in subsurface circulation (Banse et al., 2014).

The ongoing deoxygenation of the open ocean has been attributed to greenhouse gas-driven global warming (Bopp et al., 2013). The ocean warming results in decrease in solubility of O<sub>2</sub> (**Figure 1.1**); hence, there exists a strong correlation between the ocean deoxygenation and the heat content (Ito et al., 2017). This reduced solubility is estimated to contribute approximately 15 % to the current global O<sub>2</sub> loss and more than 50 % to the O<sub>2</sub> decline in the upper 1000 m of the ocean (Helm et al., 2011; Schmidtko et al., 2017). Additionally, warming increases the metabolic rates, which in turn accelerates the consumption of O<sub>2</sub>. Consequently, the decomposition of sinking particles occurs at a faster pace, and the remineralisation of these particles is shifted toward shallower depths, resulting in a spatial redistribution of low O<sub>2</sub> (Brewer & Peltzer, 2017).

The remaining 85 % of global ocean O<sub>2</sub> loss is attributed to the intensified stratification resulting from the warming of the surface ocean. Warming causes the surface layer to become lighter than the subsurface layer, reducing ventilation and affecting the supply of nutrients crucial for organic matter production and its subsequent sinking from the surface ocean (**Figure**

1.1). In addition, increased stratification also alters the predominantly wind-driven circulation in the upper few hundred meters of the ocean and decelerates the deep overturning circulation (Schmidtko et al., 2017).

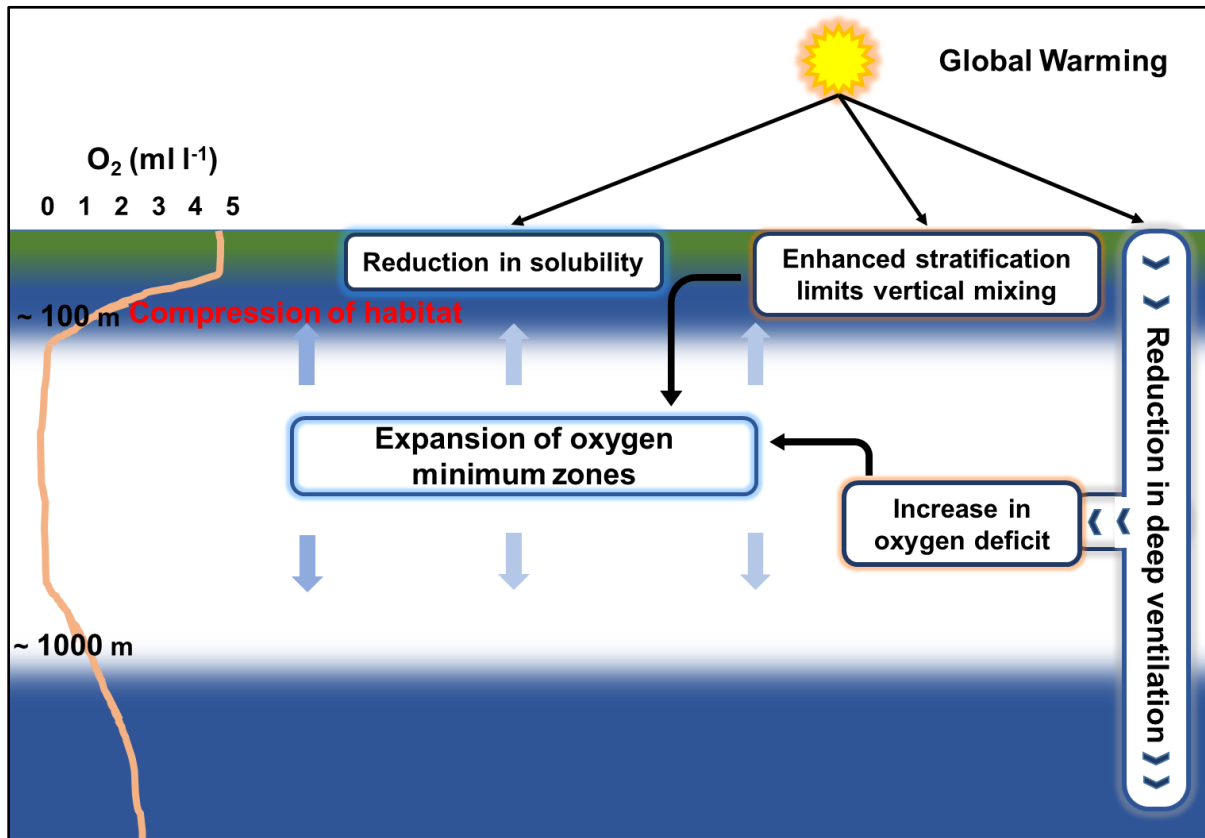


**Figure 1.1:** Schematic representation of expanding oxygen minimum zones (in white colour) due to warming-induced changes in the ocean. Modified after Stramma et al. (2010).

#### 1.4 Nitrogen cycling in the oxygen minimum zones

Nitrogen is a crucial nutrient for photosynthesis and a limiting nutrient for ocean primary productivity (Falkowski & Raven, 2007). Its cycling in the ocean is intimately linked to the availability of dissolved O<sub>2</sub> (Diaz & Rosenberg, 2008; Gruber & Galloway, 2008; Ravishankara et al., 2009). While dinitrogen (N<sub>2</sub>) is abundant in the ocean, it can only be utilised in this form by a group of specialized organisms known as diazotrophs (Zehr & Capone, 2020). The diazotrophs, also known as N<sub>2</sub> fixers, convert N<sub>2</sub> into its bioavailable form, and upon subsequent remineralisation of the biomass, it replenishes the dissolved inorganic or bioavailable nitrogen pools in both surface and subsurface waters (**Figure 1.2**). This process

of biological conversion of  $N_2$  to bioavailable nitrogen (nitrate:  $NO_3^-$  and ammonium:  $NH_4^+$ ) is called  $N_2$  fixation (Zehr & Capone, 2020). The  $N_2$  fixation, on average, produces an isotope effect of  $\sim 0 \text{ ‰}$  (Zhang et al., 2014). The new nitrogen produced by  $N_2$  fixation fuels primary productivity, ultimately playing a significant role in facilitating the net sequestration of  $CO_2$  from the atmosphere (Gruber & Galloway, 2008).

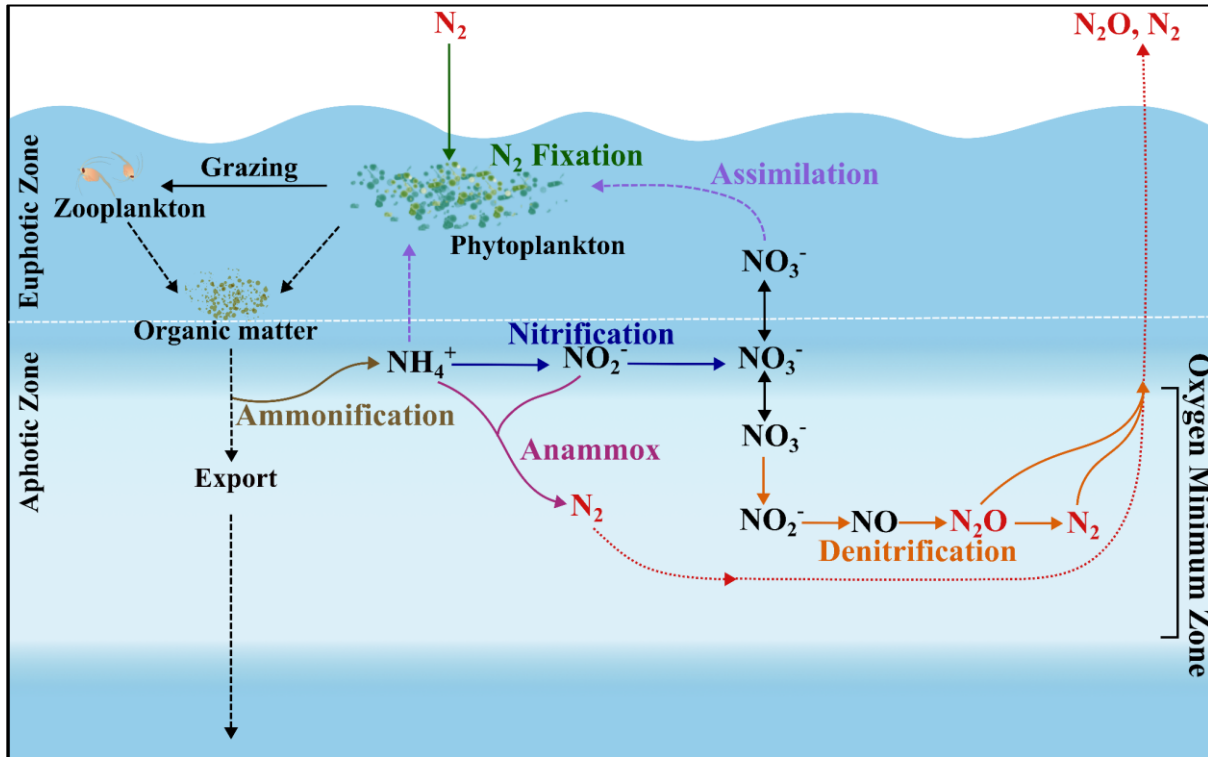


**Figure 1.2:** Schematic of the marine nitrogen cycle. Modified after Casciotti (2016).

In the upper ocean,  $NH_4^+$  produced during remineralisation is converted to  $NO_2^-$  (nitrite) with a nitrogen isotopic fractionation of  $\sim 16 \text{ ‰}$  (Sigman & Fripiat, 2019) and finally to  $NO_3^-$  by nitrifying bacteria through nitrification (Ward, 2008). This bioavailable nitrogen is then utilised by phytoplankton to produce organic matter via photosynthesis (**Figure 1.2**). A significant portion of organic matter decomposes within the euphotic zone to replenish nutrients, while a minor fraction sinks below the euphotic zone. In the subsurface waters, when the dissolved  $O_2$  concentration falls below  $5 \mu\text{mol kg}^{-1}$ , the heterotrophic bacteria utilise the oxygen associated with  $NO_3^-$  and reduce  $NO_3^-$  to  $N_2$  in a multi-step process:  $NO_3^- \rightarrow NO_2^- \rightarrow NO$  (nitric oxide)  $\rightarrow N_2O$  (nitrous oxide)  $\rightarrow N_2$  (**Figure 1.2**). This reduction process is called denitrification (Canfield & Thamdrup, 2009). Denitrification exhibits a strong preference for

the lighter isotope,  $^{14}\text{N}$ , gradually enriching the residual nitrate pool in  $^{15}\text{N}$  as nitrate consumption progresses. Based on a comprehensive review of culture and field studies, the prevailing data indicate an isotopic effect ranging from 15‰ to 25‰ in denitrification processes (Sigman & Fripiat, 2019). Denitrification removes the bioavailable nitrogen from the ocean, thereby limiting primary productivity as well as  $\text{CO}_2$  sequestration (Gruber & Sarmiento, 1997). Additionally, it produces  $\text{N}_2\text{O}$ , a potent greenhouse gas that significantly affects climate (Ravishankara et al., 2009).

In the surface ocean, phytoplankton assimilates various forms of fixed nitrogen (including  $\text{NO}_3^-$ ,  $\text{NH}_4^+$ ,  $\text{NO}_2^-$ , and organic nitrogen compounds) (Bange et al., 2005). Studies conducted in controlled laboratory settings indicate that different forms of fixed nitrogen assimilation exhibit distinct isotope effects, although these effects may vary under physiological conditions (Sigman & Fripiat, 2019). Across all forms studied, phytoplankton show a preference for incorporating  $^{14}\text{N}$  relative to  $^{15}\text{N}$ . Estimates derived from field observations suggest an isotope effect of nitrate assimilation ranging from 4‰ to 10‰, with the majority falling between 4‰ and 7‰ (Sigman & Fripiat, 2019). Other forms of fixed nitrogen assimilated by phytoplankton (such as  $\text{NH}_4^+$ ,  $\text{NO}_2^-$ , and urea) are produced and rapidly consumed within the surface mixed layer of the open ocean, maintaining a balance between production and consumption over short timescales (days or less). Consequently, the isotopic fractionation associated with the assimilation of these nitrogen forms has a lesser impact on nitrogen isotope distributions than nitrate assimilation.

## 1.5 Consequences of ocean deoxygenation

The ocean deoxygenation poses severe consequences to the marine ecosystems (Breitburg et al., 2018). Nearly all higher organisms rely on  $\text{O}_2$  for respiration, so its loss significantly diminishes biodiversity. Reports frequently document large-scale fish deaths resulting from deoxygenation. When  $\text{O}_2$ -depleted subsurface waters reach the euphotic zone, the phytoplankton community structure undergoes significant alteration, leading to cascading effects on food webs (Diaz & Rosenberg, 2008; Stramma et al., 2008). Deoxygenation can also facilitate the proliferation of harmful algal blooms, severely impacting fisheries and resulting in substantial socio-economic repercussions (Kim et al., 2023). The threshold  $\text{O}_2$  concentration, below which behavioural changes occur in marine organisms, is often considered to be  $\sim 61 \mu\text{mol kg}^{-1}$  (Diaz, 2016). However, this threshold varies widely among different groups and even within the same group, e.g., crustaceans being relatively more tolerant and gastropods

more sensitive to O<sub>2</sub> loss (Vaquer-Sunyer & Duarte, 2008). Deoxygenation causes habitat compression for pelagic organisms, making them more vulnerable to predation, and affects the vertical distribution and diurnal migration of zooplankton (Breitburg, 2002; Vaquer-Sunyer & Duarte, 2008). Other effects include reduced growth and reproduction, physiological stress, and disruption of life cycles (Breitburg, 2002; Breitburg et al., 2018; Rabalais et al., 2014).

O<sub>2</sub> availability impacts sources and sinks of nutrients like nitrogen, phosphorus, and iron, influencing their cycling in marine ecosystems (Breitburg et al., 2018). Despite the relatively small size of low-oxygen areas, oxygen-dependent nutrient processes can have far-reaching effects throughout the ocean due to circulation patterns. Consequently, changes in OMZs can influence nutrient budgets, biological productivity, and carbon fixation on a global scale. Anoxic shelves also contribute to the release of methane, a potent greenhouse gas, into the atmosphere (Naqvi et al., 2010). Additionally, hydrogen sulphide, a toxic gas to most aerobic organisms, is produced in anoxic sediments and can be released to the surface waters through upwelling (Wright et al., 2012). Moreover, the global distribution of trace metals like cadmium, copper, and zinc may be affected, as they precipitate as sulphides in anoxic waters (Janssen et al., 2014). These trace elements serve as micro-nutrients and can have a significant effect on plankton growth.

The complete depletion of O<sub>2</sub> from the ocean leads to the emergence of anaerobic microbial communities. These microbes sequentially utilise oxidised forms of various elements to decompose organic matter and produce energy (Naqvi, 1994). Currently, this process is primarily observed in the cores of OMZs in the open ocean. However, the volume of surrounding waters containing traces of O<sub>2</sub> is substantial, and with ongoing intensification, anaerobic transformations of these elements are expected to become more widespread. With the expansion of low-oxygen areas, anaerobic processes like denitrification and anammox remove bioavailable nitrogen from the ocean (Somes et al., 2017), constraining primary productivity in the surface waters (Altabet, 2007). Furthermore, N<sub>2</sub>O produced through denitrification and nitrification in oxygen-depleted ocean may provide positive feedback to climate change (Bange et al., 2010).

## **1.6 Implication to future projections**

Effective management of ecosystems relies on reliable future projections across various scenarios and an understanding of the associated uncertainties. These predictions can be generated with the help of numerical models. Numerical models and observational data

generally agree on the total amount of O<sub>2</sub> loss in the surface ocean (Oschlies et al., 2017). Furthermore, there is consensus that direct solubility effects contribute minimally to the decrease in oceanic O<sub>2</sub> levels (Bopp et al., 2013). Despite this agreement, numerical models consistently underestimate the decrease in the ocean O<sub>2</sub> inventory by roughly half compared to the latest observation-based estimates. Additionally, these models predict diverse spatial patterns of O<sub>2</sub> decline or even potential increase (Bopp et al., 2013; Oschlies et al., 2008; Schmidtko et al., 2017), with the most pronounced disparities observed in the tropical thermocline (Stramma et al., 2012). The existing uncertainties limit our ability to accurately predict the regional impacts of climate warming on open-ocean OMZs and, consequently, on oxygen-sensitive biogeochemical processes like the nitrogen budget.

Moreover, the extent to which alterations in ventilation versus respiration contribute to the decline in ocean O<sub>2</sub> levels remains unclear (Breitburg et al., 2018). It is possible that mechanisms beyond greenhouse gas-driven warming are involved in the observed decline in ocean O<sub>2</sub> concentration, but these mechanisms are not adequately captured by current ocean models. These complexities necessitate the need for further research to better understand and accurately predict the dynamics of oceanic O<sub>2</sub> decline. Enhancing models with more realistic and detailed consideration of mechanisms beyond CO<sub>2</sub>-driven global warming, such as atmospheric nutrient deposition and decadal- to multidecadal-scale climate variability (particularly fluctuations in wind patterns), may enhance consensus among models and thereby improve their predictive accuracy regarding the spatial distribution of low O<sub>2</sub> areas in both past and future scenarios.

Conducting a comprehensive study of this kind requires a long-term data set, which is not available at present. Nonetheless, the geological past offers an alternative approach to investigate the link between climate variability and ocean deoxygenation. The geological past has witnessed many climatic shifts from cold to warm periods (glacial to interglacial), the most recent glacial period being the Last Glacial Maximum (LGM) around 20,000 years ago. Moreover, changes in productivity and ventilation, as well as changes in wind patterns, have also been observed in the geological past (Banakar et al., 2005; Bialik et al., 2020; Hess et al., 2023). Because the dissolved O<sub>2</sub> levels are intricately linked to these factors, reconstructing past dissolved O<sub>2</sub> in relation to these changes could enhance our understanding of O<sub>2</sub> variability amid long-term climatic shifts. Additionally, paleo-reconstruction could serve as a benchmark for numerical models to improve future projections. However, paleo reconstruction requires

the use of proxies - indirect indicators that can provide information about past environmental conditions.

## 1.7 Proxies

Proxies provide indirect information of processes as they are sensitive to climate conditions, whether physical, chemical, or biological, and remain preserved over geological time scales. They offer insights into past climatic conditions, aiding our understanding of how the Earth's climate system has evolved over millennia (Smerdon, 2017). Utilising these proxies to reconstruct past climates requires an understanding of their relationship to various aspects of climate systems. For instance, some proxies, like atmospheric gases (e.g., carbon dioxide and methane) trapped in glacial ice, offer direct measurements of atmospheric chemistry at the time of ice formation. Conversely, other proxies, like stable isotope measurements (e.g., oxygen and carbon isotopes) from marine organism shells, provide indirect indications of climate conditions, such as temperature and salinity. These proxies require calibration studies within the contemporary framework to determine the correlation between climate mechanisms and the proxy.

For understanding the past dissolved O<sub>2</sub> concentration in the ocean water column, mainly two proxies have been used from the marine sediment cores: Bulk sedimentary δ<sup>15</sup>N (Altabet et al., 1995; Suthhof et al., 2001) and iodine to calcium (I/Ca) ratios in planktic foraminifera tests (Hoogakker et al., 2018; Lu et al., 2016).

### 1.7.1 Bulk sedimentary δ<sup>15</sup>N

Nitrogen exists in various redox states in the ocean. It is transformed from one form to another through biologically mediated processes. These transformations are typically accompanied by kinetic fractionation, which leads to variations in the isotopic composition of nitrogen (<sup>15</sup>N/<sup>14</sup>N) in various pools (Altabet & Francois, 1994; Montoya, 1994). The nitrogen isotopic composition of the dissolved inorganic nitrogen in the ocean is affected by various processes: N<sub>2</sub> fixation by diazotrophic bacteria (Karl et al., 1997), surface NO<sub>3</sub><sup>-</sup> assimilation (Altabet & Francois, 1994), nitrification, denitrification (Liu & Kaplan, 1989), and anammox (**Figure 1.3**). Processes like N<sub>2</sub> fixation, denitrification, and anammox regulate the inventory of bioavailable nitrogen in the ocean. The nitrogen isotopic composition is expressed as δ<sup>15</sup>N:

$$\delta^{15}\text{N} (\%) = \left( \left( \frac{{}^{15}\text{N}/{}^{14}\text{N}_{\text{sample}}}{{}^{15}\text{N}/{}^{14}\text{N}_{\text{standard}}} \right) - 1 \right) \times 1000,$$

Where,  $(^{15}\text{N}/^{14}\text{N})_{\text{sample}}$  is the ratio abundances of heavier ( $^{15}\text{N}$ ) to lighter ( $^{14}\text{N}$ ) isotope of nitrogen in a sample, and  $(^{15}\text{N}/^{14}\text{N})_{\text{standard}}$  is the ratio abundances of heavier ( $^{15}\text{N}$ ) to lighter ( $^{14}\text{N}$ ) isotope of nitrogen in standard. The standard for nitrogen is atmospheric  $\text{N}_2$ .

During the assimilation of bioavailable nitrogen by microorganisms to form biomass, the  $\delta^{15}\text{N}$  of their nitrogen source is reflected in the organic matter and is eventually deposited in sediments. The  $\delta^{15}\text{N}$  of the source is influenced by the initial  $\delta^{15}\text{N}$  of the water mass and by any process that adds or removes nitrogen, such as remineralisation or water column denitrification, along its path to the subsurface waters. Changes in the isotopic signal in the surface ocean by the introduction of newly fixed nitrogen by  $\text{N}_2$  fixation or the partial consumption of  $\text{NO}_3^-$  can also alter the source signature of the sub-euphotic zone. In a nutshell, sedimentary  $\delta^{15}\text{N}$  reflects shifts in ocean circulation, the biological pump, and large-scale nitrogen cycling (Brandes & Devol, 2002; Deutsch et al., 2004; R. S. Robinson et al., 2012; Sigman et al., 2010). Additionally,  $\delta^{15}\text{N}$  has been indirectly used as a paleoredox proxy because denitrification - the process where organic matter respire using  $\text{NO}_3^-$  occurs under suboxic conditions (Altabet et al., 1995; Jaccard & Galbraith, 2012; Suthhof et al., 2001). However, as shown previously,  $\delta^{15}\text{N}$  can also be influenced by other processes, limiting its unambiguous use as a proxy for low dissolved  $\text{O}_2$ .

The bulk sedimentary  $\delta^{15}\text{N}$  reflects the  $\delta^{15}\text{N}$  of the sinking flux of organic matter alongside any secondary isotopic changes arising during sinking and burial due to nitrogen removal or addition (**Figure 1.3**). It is essential to accurately constrain the extent of fractionation related to alteration to effectively utilise the nitrogen isotopic composition of bulk sediments as a paleoceanographic proxy. Studies conducted on sinking particles in diverse regions have demonstrated alterations in the  $\delta^{15}\text{N}$  of sinking particles with depth during periods of low export flux or in low-productivity zones. These alterations could result from the addition of nitrogen from alternative sources (Altabet et al., 1991; Altabet & Francois, 2001; Lourey et al., 2003) or the loss of specific organic nitrogen fractions (Macko & Estep, 1984). The observed alterations are not consistently unidirectional, as they include both increases and decreases in  $\delta^{15}\text{N}$ . Nonetheless, during blooms, the  $\delta^{15}\text{N}$  of sinking particulate nitrogen remains stable with depth (Altabet et al., 1991; Altabet & Francois, 1994). Given that the high-flux events contribute to the majority of organic matter accumulating in sediments, organic nitrogen reaching the sediment-water interface generally retains the  $\delta^{15}\text{N}$  signature of surface organic nitrogen.

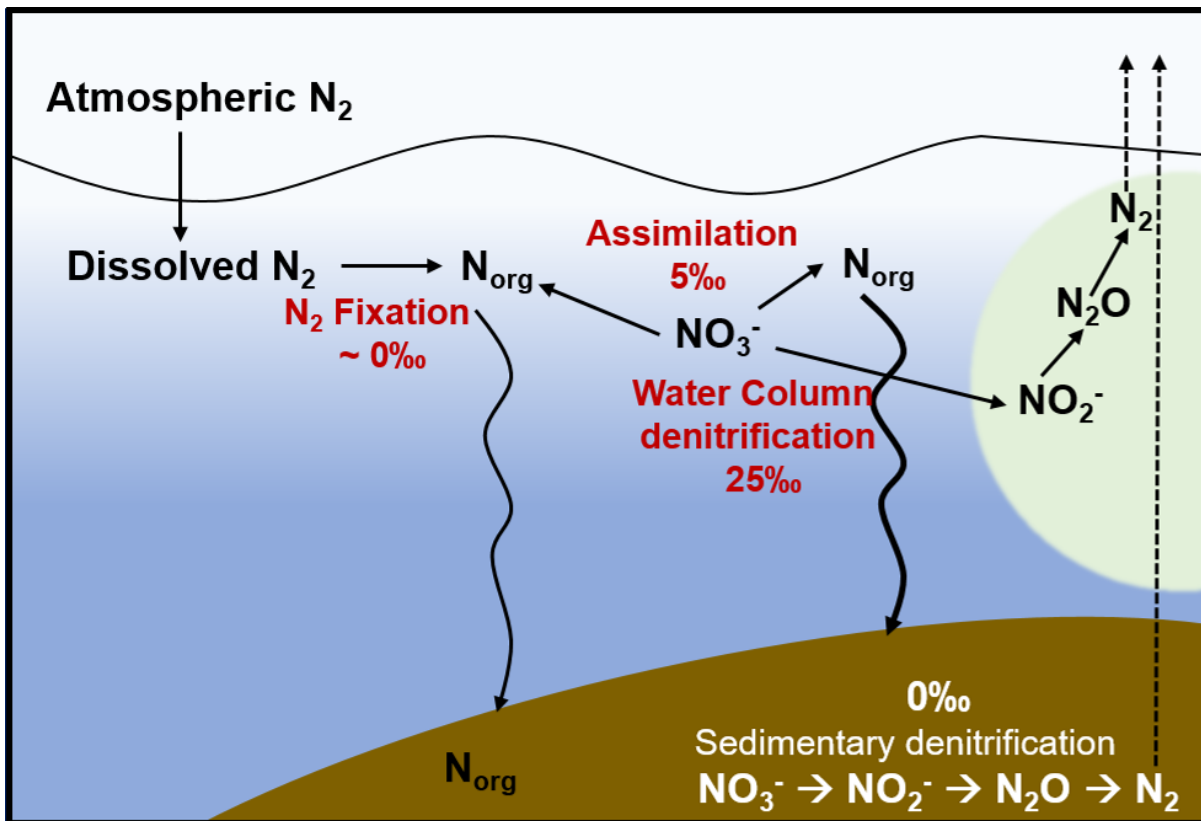


**Figure 1.3:** Schematic of the processes in the nitrogen cycle typically recorded in  $\delta^{15}N$  of marine sediments. The average isotopic enrichment factors (shown in ‰ units) for individual processes are mentioned. The light green shaded region shows a suboxic water column. Figure Redrawn after Robinson et al. (2012).

### 1.7.2 Iodine to Calcium ratios in planktic foraminifera

The I/Ca proxy is based on the speciation of iodine in the ocean. Iodine in the ocean is introduced through various ways: dry deposition of aerosols, through subduction zones, diagenesis of sediments, and terrestrial input. It is removed by sedimentation as organic iodine and escapes to the atmosphere by ozone reaction. There are two thermodynamically stable forms of inorganic iodine in the ocean: iodate ( $IO_3^-$ ) and iodide ( $I^-$ ) (Wong & Brewer, 1977). The speciation of  $IO_3^-$  and  $I^-$  can serve as an indicator of seawater redox potential. The standard reduction potential of  $IO_3^-/I^-$  is similar to  $O_2/H_2O$  (Table 1.2), which implies that iodine is sensitive to the changes in the dissolved  $O_2$  levels (Rue et al., 1997). Iodine has a relatively long residence time of ~300 kyr in seawater, resulting in an invariant total iodine (sum of  $IO_3^-$  and  $I^-$ ) concentration of 0.45  $\mu M$  in modern seawater (Küpper et al., 2011). In oxic conditions,

$\text{IO}_3^-$  is the predominant form of iodine in the water column (**Figure 1.4**) (Truesdale et al., 2000).

With the decrease in dissolved  $\text{O}_2$  concentration, the concentration of  $\text{IO}_3^-$  decreases from the surface waters towards the OMZs as it is converted to  $\text{I}^-$ .  $\text{IO}_3^-$  levels drop less than  $0.05 \mu\text{M}$  within the coastal surface waters under severe hypoxic events (Truesdale & Bailey, 2000). In the anoxic basins below the surface waters,  $\text{I}^-$  is the dominant form of iodine (Wong & Brewer, 1977). The predominance of  $\text{I}^-$  in low  $\text{O}_2$  waters is due to the fast reduction of  $\text{IO}_3^-$  to  $\text{I}^-$  (Rue et al., 1997). However, the oxidation of  $\text{I}^-$  to  $\text{IO}_3^-$  is very slow (Hardisty et al., 2020) and can take up to 40 years, resulting in low concentration of  $\text{I}^-$  in oxygenated waters (Chance et al., 2014).

**Table 1.2:** Reduction potential and redox couples of various elements. The reduction potential values are from Lu et al. (2010).

S.No.	Element	Redox Couple	Reduction Potential, $E^\circ$ (volts)
1	Cerium	$\text{Ce}^{4+} - \text{Ce}^{3+}$	1.44
2	Oxygen	$\text{O}_2 - \text{H}_2\text{O}$	1.23
3	Manganese	$\text{MnO}_2 - \text{Mn}^{2+}$	1.23
4	Iodine	$\text{IO}_3^- - \text{I}^-$	1.21
5	Nitrogen	$\text{NO}_3^- - \text{NO}_2^-$	0.79
6	Iron	$\text{Fe}^{3+} - \text{Fe}^{2+}$	0.68
7	Uranium	$\text{UO}_2^{2+} - \text{U}^{4+}$	0.27
8	Chromium	$\text{CrO}_4^{2-} - \text{Cr}(\text{OH})_3$	-0.12
9	Sulphur	$\text{SO}_4^{2-} - \text{H}_2\text{S}$	-0.66
10	Molybdenum	$\text{MoO}_4^{2-} - \text{MoO}_2$	-0.93

Laboratory calcite synthesis experiments (Lu et al., 2010; Zhou et al., 2014), synchrotron (Podder et al., 2017), and modelling studies (Feng & Redfern, 2018) have demonstrated that  $\text{IO}_3^-$  is incorporated into the calcite lattice, substituting for the carbonate ion, with the charge balance typically occurring through  $\text{Ca}^{2+}$  substitution (e.g.  $\text{Na}^+$ ). In contrast, iodide is likely excluded from the mineral lattice. Synthetic carbonate minerals incorporate  $\text{IO}_3^-$  linearly, suggesting that biogenic carbonate (like foraminifera)  $\text{I}/\text{Ca}$  qualitatively indicates  $\text{IO}_3^-$  availability, assuming analogous behaviour between inorganic and biogenic precipitates (**Figure 1.4**). Therefore, variations in  $\text{IO}_3^-$  concentrations in the water, which is controlled by dissolved  $\text{O}_2$ , is reflected in the  $\text{I}/\text{Ca}$  values of carbonate (Lu et al., 2010; Zhou et al., 2014).

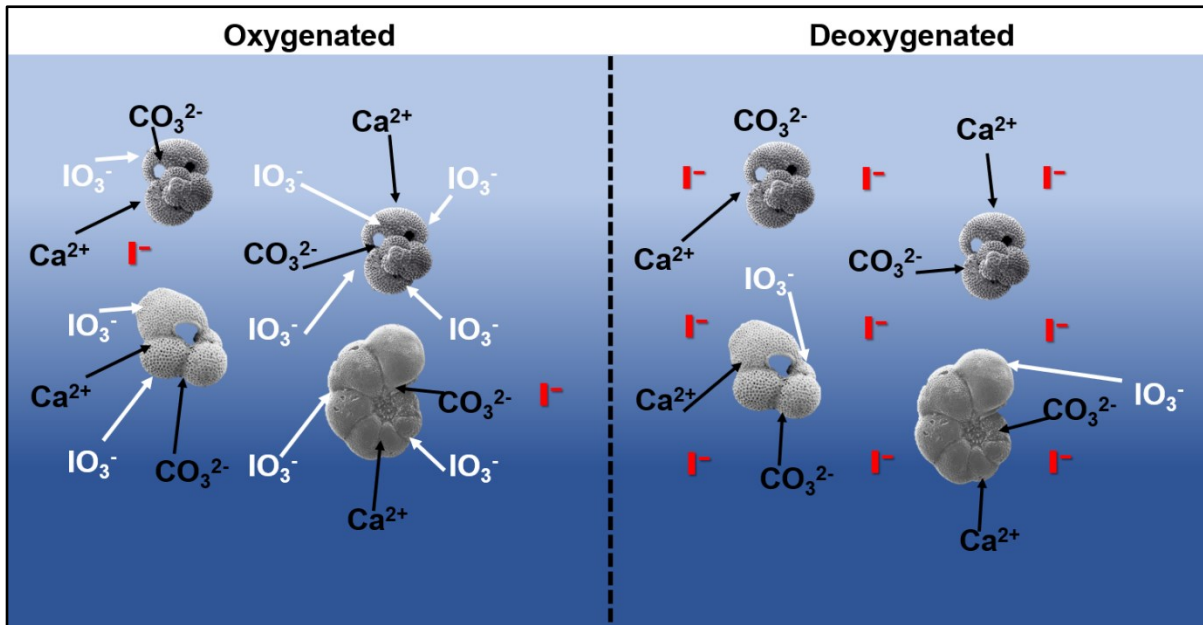


**Figure 1.4:** Schematic representation of  $\text{IO}_3^-$  incorporation in planktic foraminifera in different dissolved  $\text{O}_2$  concentration levels. The gradient in blue colour shows the transition from the surface ocean (light colour) to the subsurface (darker colour).

Planktic foraminifera are found at various depths within the ocean, ranging from the surface mixed layer to the upper thermocline and occasionally within OMZs (Schiebel & Hemleben, 2017). The use of the planktic foraminifera  $\text{I}/\text{Ca}$  ratios enables the assessment of ocean  $\text{O}_2$  levels in the upper water column of the open ocean (Lu et al., 2020; Lu et al., 2016). Current research suggests that  $\text{I}/\text{Ca}$  values exceeding  $4 \mu\text{mol mol}^{-1}$  are associated with  $\text{O}_2$  levels exceeding  $100 \mu\text{mol kg}^{-1}$ , while values below  $1.5 \mu\text{mol mol}^{-1}$  indicate regions with  $\text{O}_2$  concentrations below  $7 \mu\text{mol kg}^{-1}$ , based on comparisons with present-day core-top  $\text{I}/\text{Ca}$  versus minimum  $\text{O}_2$  concentration calibrations (Hardisty et al., 2021; Lu et al., 2020; Lu et al., 2016).

## 1.8 Oxygen minimum zone in the Arabian Sea

The Arabian Sea is a semi-enclosed basin heavily influenced by the Indian monsoon system and is one of the most productive regions in the world ocean. It hosts one of the thickest OMZ worldwide (Kamykowski & Zentara, 1990), characterised by dissolved  $\text{O}_2$  concentrations in the suboxic range ( $\lesssim 5 \mu\text{mol O}_2 \text{ kg}^{-1}$ ) across much of the intermediate depths (150 – 1250 m) in the central-eastern Arabian Sea (Morrison et al., 1998). This extensive suboxia results from markedly high rates of microbial respiration in the water column, compounded by relatively poor ventilation of intermediate waters (McCreary et al., 2013).

Despite covering less than 2 % of the total area of the world ocean, the Arabian Sea contributes up to 20 – 30 % of global water column denitrification (Bange et al., 2005; Dueser et al., 1978; Lachkar et al., 2023; Naqvi, 1994). This process reduces the oceanic supply of bioavailable nitrogen crucial for phytoplankton growth and acts as a source of N<sub>2</sub>O gas (Bange et al., 2005).

The high surface productivity in the Arabian Sea is primarily due to the nutrient influx into the euphotic zone either from the subsurface by wind-driven coastal upwelling or winter convective mixing and/or from surrounding landmasses through the transportation and deposition of aeolian dust (Bali et al., 2019; Lee et al., 2000; Prasanna Kumar & Narvekar, 2005). The seasonal reversal of monsoonal winds plays a crucial role in shaping the upper circulation and stratification of the Arabian Sea, thereby influencing the distribution of nutrients and hence primary productivity (Schott & McCreary, 2001; Wang & Ding, 2008).

During the summer monsoon, the Asian landmass heats up faster than the Indian Ocean, creating a land-sea temperature gradient. This gradient drives strong, moisture-laden southwesterly winds that traverse diagonally across the Arabian Sea, resulting in the formation of a clockwise upper ocean circulation pattern (**Figure 1.5 (a)**). These winds, coupled with Ekman pumping, lead to the development of strong coastal upwelling off Somalia and Oman. This upwelling brings cold, nutrient-rich waters to the euphotic zone, supporting high primary productivity across a wide area extending to the central basin (Bartolacci & Luther, 1999; Kumar et al., 2001; Lee et al., 2000) (**Figure 1.5 (a)**). Conversely, during the winter monsoon, the land-sea temperature gradient reverses, with land cooling faster than the Indian Ocean. This results in dry, cold, northeasterly winds blowing from the Asian continent. These winds drive an anti-clockwise upper ocean circulation pattern, accompanied by convective mixing north of 15°N (**Figure 1.5 (b)**) (Madhupratap et al., 1996). This mixing leads to the resurfacing of cold, nutrient-rich intermediate waters, fueling high primary productivity in the northern part of the Arabian Sea (Prasanna Kumar & Narvekar, 2005; Schott & McCreary, 2001) (**Figure 1.5 (b)**).

The primary source of ventilation for intermediate waters in the northern Arabian Sea is the Indian Ocean Central Water, which is a mixture of aged Antarctic Intermediate Water, Subantarctic Mode Water, and Indonesian Intermediate Water, transported northward by the Somali current (Olson et al., 1993; Resplandy et al., 2012; You, 1998) (**Figure 1.6**). Additionally, dense and highly saline Red Sea Water and the Persian Gulf Water contribute to the ventilation of the intermediate depths in the Arabian Sea (Bower et al., 2000; Prasad et al., 2001) (**Figure 1.6**).

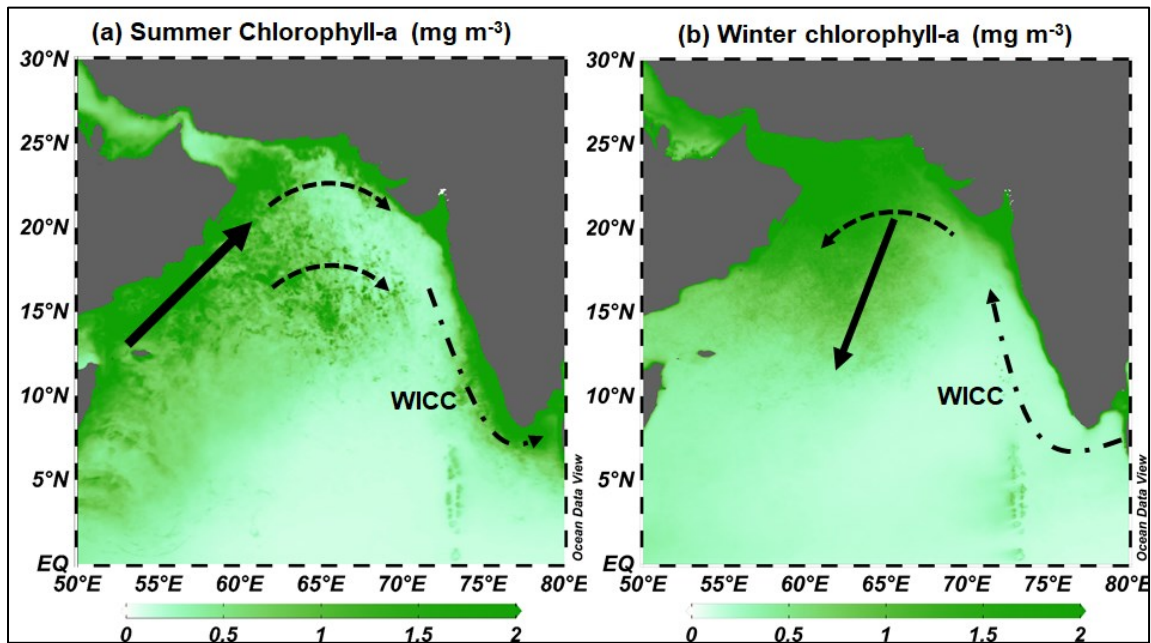


**Figure 1.5:** (a) Climatological (2002-2023) summer chlorophyll-a concentration ( $\text{mg m}^{-3}$ ): (b) Climatological (2002-2023) winter chlorophyll-a concentration ( $\text{mg m}^{-3}$ ). Bold arrows represent the wind direction and dashed lines represent the surface circulation directions during the different monsoon seasons. WICC is West India Coastal Current. Chlorophyll-a data source: Aqua/MODIS from 2002 to 2023.

Recent observations indicate a potential intensification of the Arabian Sea OMZ, particularly in the west, north, and central regions (Banse et al., 2014; Gomes et al., 2014; Piontkovski & Al-Oufi, 2015; Queste et al., 2018). Ito et al. (2017) demonstrated a moderate strengthening of the Arabian Sea OMZ between 1960 and 2010. Gomes et al. (2014) reported a significant shift in dominant species during winter blooms in the northern Arabian Sea, transitioning from diatoms to large, green dinoflagellates like *Noctiluca scintillans*. The dinoflagellates tend to survive in the low  $\text{O}_2$  conditions. They use a combination of photosynthesis from their endosymbionts and prey ingestion, potentially giving them a competitive advantage over diatoms in regions with declining  $\text{O}_2$  concentrations. The strengthening of the Arabian Sea OMZ could have far-reaching impacts, not only on marine ecosystems and habitats but also on denitrification processes, potentially disrupting the broader marine nitrogen budget and carbon cycle. However, a comprehensive understanding of the factors driving the decline in  $\text{O}_2$  levels is still required.

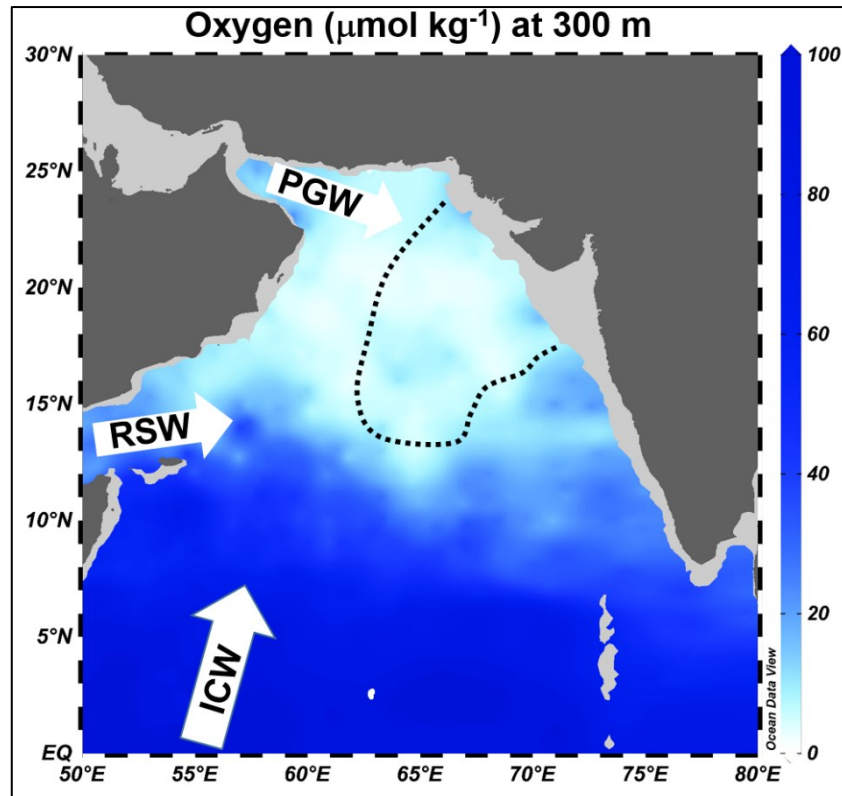


**Figure 1.6:** Intermediate water masses in the Arabian Sea, superimposed over climatological dissolved O<sub>2</sub> concentration at 300 m depth. The black dashed curve represents the present-day denitrification zone. Dissolved O<sub>2</sub> data are taken from World Ocean Atlas 2018. RSW – Red Sea Water, PGW – Persian Gulf Water, ICW – Indian Central Water.

The extent to which atmospheric and deep-ocean circulations influence the Arabian Sea OMZ over various temporal and spatial scales remains unclear. To evaluate the possible expansion and severity of OMZ intensification, it is crucial to examine changes in the OMZ across the basin in response to climate variability occurring at different time intervals.

## 1.9 Previous Studies in the Arabian Sea

To understand the evolution of the Arabian Sea OMZ, some studies have been carried out using various proxies: bulk sedimentary  $\delta^{15}\text{N}$  (Altabet et al., 1995; Kao et al., 2015; Pichevin et al., 2007; Suthhof et al., 2001), benthic foraminiferal diversity (Singh et al., 2015), Pteropod or Aragonite preservation (Böning & Bard, 2009; Klöcker et al., 2006; Naidu et al., 2014). All these proxies are qualitative in nature and have their inherent limitations. As discussed in section 1.7.1, bulk sedimentary  $\delta^{15}\text{N}$  is not an unambiguous proxy for dissolved O<sub>2</sub> reconstruction. Instead, it is a proxy for the nitrogen cycle. Similarly, the faunal proxies can only be applied to core locations bathed by OMZ waters, limiting their use in the open ocean

thermocline. Moreover, all these records are from continental margins, which may be compromised by local/terrestrial processes. Nevertheless, it has been inferred from these studies that the Arabian Sea was better oxygenated (indicated by reduced denitrification) during the LGM, whereas warm interglacials were highly deoxygenated, indicated by intensified denitrification. However, Lachkar et al. (2019) suggest that the Arabian Sea OMZ was more intensified during the LGM.

These studies suggest a lack of a unified understanding of the dissolved O<sub>2</sub> levels in the past. Even after these indirect approaches with their inherent limitations, the relative importance of atmospheric and ocean circulation governing the Arabian Sea OMZ is not well understood. Novel proxies like the I/Ca ratios of the planktic foraminifera, primarily governed by dissolved O<sub>2</sub> concentration in the water column, can offer new insights into the Arabian Sea OMZ in the past. Recently, Hoogakker et al. (2018) utilised I/Ca ratios in planktic foraminifera and suggested that in the eastern tropical Pacific, O<sub>2</sub>-depleted waters expanded during the glacial period, contradicting the inferences drawn from bulk sedimentary  $\delta^{15}\text{N}$ . Despite the interesting oxygen and nitrogen biogeochemistry of the Arabian Sea, only one study has reported I/Ca ratios for planktic foraminifera from a few core-top samples in this region (Winkelbauer, 2022). Therefore, the intense OMZ of the northern Indian Ocean remains relatively unexplored with regard to the applicability of the I/Ca proxy in this basin.

## **1.10 Scope of the present work**

The Arabian Sea is of particular interest because, unlike other open ocean OMZs, the intense oxygen-depleted conditions develop in the relatively oligotrophic central-eastern Arabian Sea, away from the highly productive upwelling zone of Oman. This is primarily due to the better ventilation of the western Arabian Sea by the intermediate water masses. Thus, the Arabian Sea is a suitable candidate for studying the linkage between O<sub>2</sub> variability and oceanic and atmospheric circulation. This can be achieved by understanding the O<sub>2</sub> variability under long-term and abrupt climatic transitions where significant changes in the oceanic and atmospheric circulation took place. In this sense, the last 50 ka provides the unique opportunity to decipher the connection between O<sub>2</sub> variability and oceanic and climatic circulation under transition from the last glacial period to the current interglacial, and also under the influence of abrupt events like the Younger Dryas, Heinrich events, and the Dansgaard-Oeschger events.

Based on the knowledge gap in the present understanding of the efficacy of I/Ca proxy in the northern Indian Ocean, and the precise mechanisms through which atmospheric and

deep-ocean circulations influence the Arabian Sea OMZ across different temporal and spatial scales, with its linkage to the nitrogen cycle, we focused on the three major objectives:

1. Validation of the I/Ca proxy in planktic foraminifera in the northern Indian Ocean.
2. Reconstruction of spatio-temporal variability of the dissolved O<sub>2</sub> concentration in the Arabian Sea over the last 50 ka.
3. Reconstruction of the paleo-nitrogen cycle in the Arabian Sea over the last 50 ka.

To fulfill these objectives, the following work was carried out:

- i. I/Ca ratios were measured on planktic foraminifera from two sedimentary cores: one from the northern Arabian Sea (situated within the core of the present-day oxygen deficient zone) and the other from the southeastern Arabian Sea (outside the present-day oxygen deficient zone). This analysis may provide insights into the spatial and temporal evolution of the dissolved O<sub>2</sub> concentration in the Arabian Sea.
- ii. Magnesium to calcium (Mg/Ca) ratios and Total Organic Carbon (TOC) % were measured on the same sediment cores from the Arabian Sea. This may help decipher the predominant factor controlling the O<sub>2</sub> variability in the Arabian Sea at different times.
- iii. In order to know about the paleo nitrogen cycle in the Arabian Sea, bulk sedimentary  $\delta^{15}\text{N}$  was measured alongside other proxies. This could help gain insights about the nitrogen cycle in response to O<sub>2</sub> changes.
- iv. I/Ca ratios in plankton-tow derived foraminifera were measured to assess the applicability of this proxy in the Arabian Sea.
- v. I/Ca ratios in planktic foraminifera from the core-top sediments from the northern Indian Ocean were measured to investigate the relationship between I/Ca and the dissolved O<sub>2</sub> concentration.



# Chapter 2

## Materials and Methods

To fulfil the thesis objectives, we procured two sediment cores from the Arabian Sea. We measured I/Ca and Mg/Ca of foraminifera tests in these two cores. We complemented this elemental ratio analysis with carbon and nitrogen isotopic composition. Along with the paleo reconstruction of O<sub>2</sub> concentrations of the Arabian Sea, we attempted to better understand the paleo proxy of I/Ca in planktic foraminifera by comparing the I/Ca of the planktic foraminifera shells of the recent marine surface sediments with the I/Ca of the foraminifera shells of the plankton tow samples. In this context, this chapter describes the oceanographic conditions in the study, various materials used and the measurement techniques employed in this thesis work.

### 2.1 Sample locations

#### 2.1.1 Deep-sea sediment cores

We collected two sediment cores using a gravity corer onboard ORV *Sagar Kanya* (SK-364 cruise) (**Figure 2.1**) from 16 December 2019 to 7 January 2020 in the Arabian Sea (**Table 2.1**). One sediment core, SK-364/03, of length 4.2 m, was from the northern Arabian Sea, and the other, SK-364/13, of length 5.16 m, was from the southeastern Arabian Sea. Both the sediment cores were sub-sampled mostly at 1 cm intervals using a non-metallic knife, and wherever 1 cm sub-sampling was not possible, it was sub-sampled at 2-3 cm.

**Table 2.1:** Details of the sediment cores studied in the present work.

S.No	Sample	Latitude	Longitude	Water Depth (m)	Core Length (m)
1	SK-364/03	20°00.004'	64°59.498'	3163	4.12 (1.8*)
2	SK-364/13	11°01.993'	71°02.501'	2825	5.16 (1.4*)

\*represents the length datable by the radiocarbon dating technique.

#### 2.1.2 Core-top sediment samples

We collected nine core-top sediment samples from the northern Indian Ocean (**Table 2.2**) using a spade (**Figure 2.2**) and a gravity corer onboard ORV *Sagar Kanya* on two research

expeditions (SK-373 and SK-374) in the northern Indian Ocean from September 2021 to November 2021 (**Figure 2.1**).

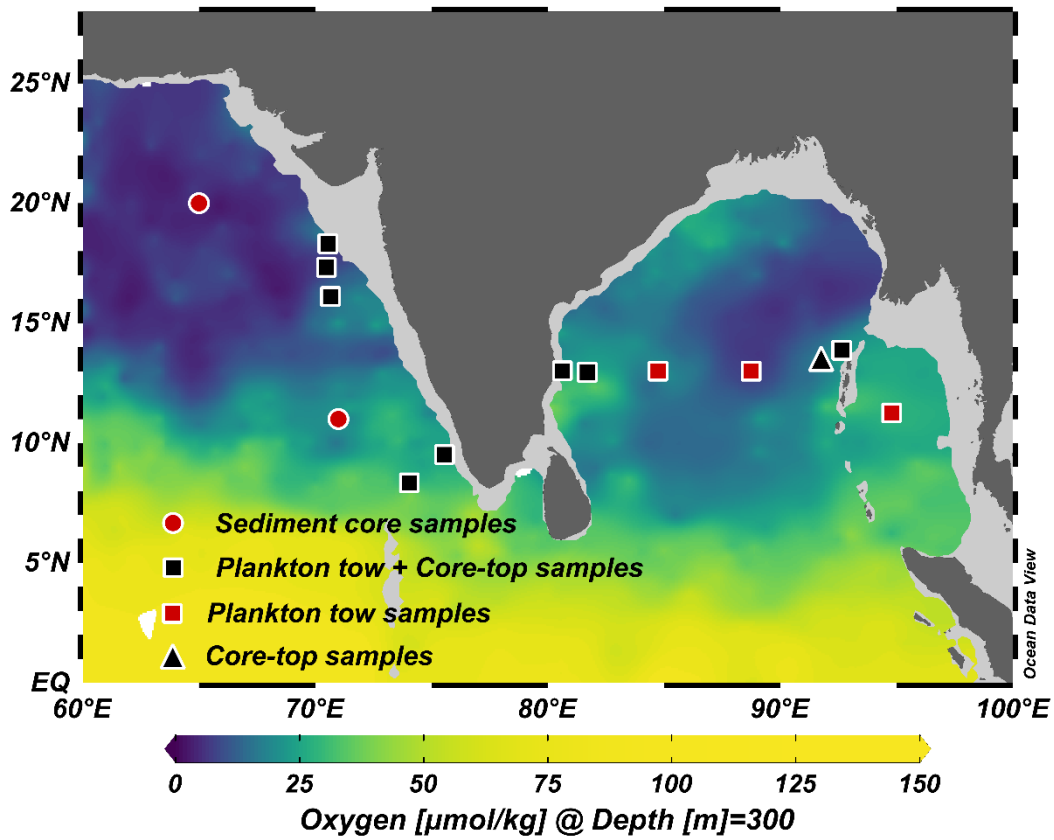


**Figure 2.1:** Locations of the different types of samples used in the present study superimposed over dissolved  $\text{O}_2$  concentration at 300 m depth. Data source of dissolved  $\text{O}_2$  – World Ocean Atlas 2018. Dissolved  $\text{O}_2$  data is climatological data.

**Table 2.2:** Details of the core-top sediments from the northern Indian Ocean

S.No	Sample ID	Corer type	Latitude (N)	Longitude (E)	Water depth (m)
1	SK-373/SP-01	Spade	13° 1.033'	80° 37.612'	196
2	SK-373/SP-02	Spade	13° 0.468'	84° 44.374'	942
3	SK-373/SP-03	Spade	13°0.77'	80°44.940'	804
4	SK-373/GC-02	Gravity	13°24.907'	91°46.137'	3047
5	SK-374/SP-01	Spade	9°30.8166'	75°33.8610'	802
6	SK-374/SP-02	Spade	8°20.1962'	74°2.8896'	2760
7	SK-374/SP-03	Spade	18°18.6094'	70°33.088'	250
8	SK-374/SP-04	Spade	17°19.466'	70°28.8716'	2989
9	SK-374/SP-05	Spade	16°19.6267'	70°39.3769'	2954

### 2.1.3 Multi plankton net (MPN) samples

We collected plankton samples from eleven locations in the northern Indian Ocean (Table 2.3, Figure 2.1). We used a multi-plankton net (Hydro Bios) with five net bags of 200  $\mu\text{m}$  mesh size (Figure 2.2). Plankton samples are collected from five discrete depth intervals (400–200 m, 200–150 m, 150–100 m, 100–50 m, and 50–0 m). After collection, we immediately preserved the plankton samples from individual depths in a 4% formalin solution at 4°C buffered with hexamethyl diamine to a pH of 8.5 (Van Raden et al., 2011). Planktic foraminifera was separated from the bulk plankton samples by wet sieving, drying, and then manually picking the foraminifera shells from the concentrate.

**Table 2.3:** Details of the locations of multi-plankton net (MPN) Samples.

S. No.	Sample ID	Latitude (N)	Longitude (E)
1	SK-373/01	13°1.033'	80°37.612'
2	SK-373/02	13°0.468'	84°44.374'
3	SK-373/03	13°0.281'	88°44.675'
4	SK-373/04	13°52.022'	92°38.107'
5	SK-373/05	11°39.545'	94°46.981'
6	SK-373/06	13°0.77'	80°44.940'
7	SK-374/01	9°30.8166'	75°33.8610'
8	SK-374/02	8°20.1962'	74°2.8896'
9	SK-374/03	18°18.6094'	70°33.088'
10	SK-374/04	17°19.466'	70°28.8716'
11	SK-374/05	16°19.6267'	70°39.3769'

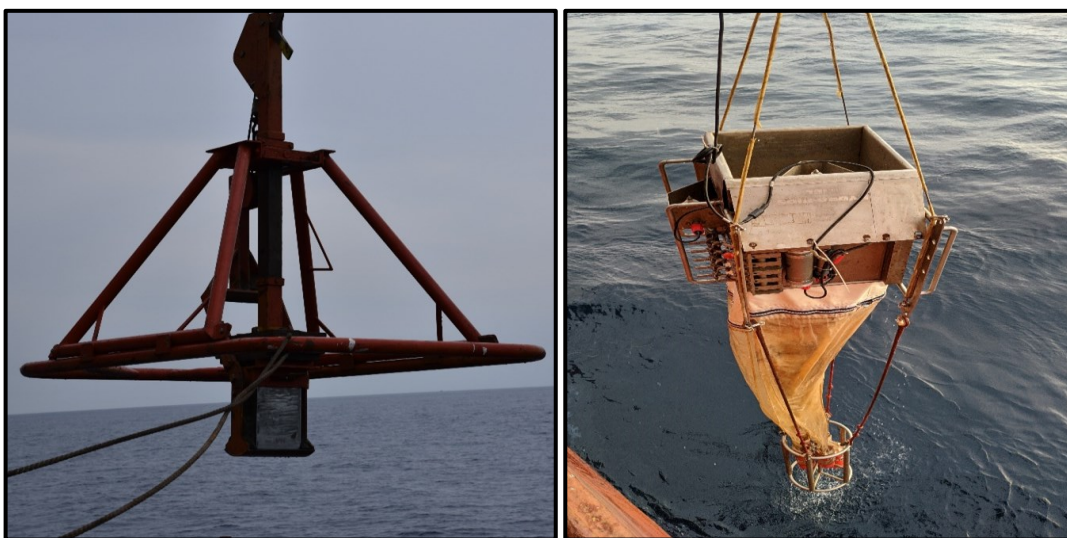


**Figure 2.2:** Spade corer (left) and multi plankton net (right) operation onboard ORV *Sagar Kanya* 373 and 374. (Photo Credit: Deepak Kumar Rai).

## 2.2 Oceanographic conditions in the study area

The northern Indian Ocean, located above the equator, is divided into two distinct regions: the Arabian Sea and the Bay of Bengal. Despite their proximity in latitude, these two basins have unique characteristics. Seasonal wind reversals significantly influence oceanic conditions in the northern Indian Ocean. These winds drive the surface boundary currents, causing them to change directions—clockwise during the southwest monsoon and counter-clockwise during the northeast monsoon. During the southwest monsoon, the West India Coastal Current (WICC) in the Arabian Sea moves equatorward and connects with the East Indian Coastal Current (EICC) in the Bay of Bengal, which flows poleward. This pattern reverses during the northeast monsoon (Kurian & Vinayachandran, 2007; Schott & McCreary, 2001). These changes in the direction of surface boundary currents are crucial in the northern Indian Ocean, as they transport surface waters with different properties between the AS and BoB.

### 2.2.1 The Arabian Sea

In the western part of the northern Indian Ocean, the strong south-westerly winds during the southwest monsoon cause significant wind-induced upwelling along the Oman margin and the Somali Coast (Kumar et al., 2001; McCreary et al., 2013; Schott & McCreary, 2001). This upwelling process brings cold, nutrient-rich water from the subsurface to the surface, boosting primary productivity in the region. During the northeast monsoon, the dry and cold winds enhance evaporative cooling of the surface waters in the northern Arabian Sea, increasing water density and causing vertical mixing. This process, known as 'convective mixing', transports nutrient-rich waters from deeper layers to the surface, leading to an increase in primary productivity during the winter months (Madhupratap et al., 1996; Prasanna Kumar & Narvekar, 2005).

The primary water masses influencing the subsurface waters of the Arabian Sea at depths of 200–1000 meters originate from two main sources: the northwest, characterized by high-density Red Sea Water and Persian Gulf Water, and the south, represented by the Indian Ocean Central Water (You, 1998). The Indian Ocean Central Water is a mixture of Sub-Antarctic Mode Water, Antarctic Intermediate Water, and Indonesian Throughflow. Below 2000 meters, the water mass comprises a mixture of Circumpolar Deep Water and North Atlantic Deep Water (You, 1998). During the summer monsoon season, the southern water mass flows across the western boundary, leading to oxygen replenishment in the western part

of the Arabian Sea. However, as it moves northeastward, the water mass becomes depleted in oxygen, contributing to oxygen-poor conditions in the northeastern region (You, 1998).

### **2.2.2 The Bay of Bengal**

The Bay of Bengal is heavily influenced by numerous rivers fed by monsoonal rains and Himalayan glaciers (Karim & Veizer, 2002; Lambs et al., 2005; Ramesh & Sarin, 1992). These rivers introduce large volumes of freshwater, creating low-salinity conditions in the northern Bay, with salinity increasing gradually equatorward. Additionally, direct precipitation significantly adds to the freshwater input in the Bay of Bengal. This substantial influx of freshwater from both riverine sources and rainfall leads to strong stratification in the Bay of Bengal (Prasad, 1997; Vinayachandran et al., 1999). As a result, wind-induced mixing is insufficient to bring nutrient-rich subsurface waters to the surface, rendering the Bay of Bengal less productive than the Arabian Sea. However, small-scale eddies and vertical mixing during the dry, cold winter months can enhance nutrient availability at the surface at certain times.

Surface waters above 100 m in the Bay of Bengal are a combination of Arabian Sea Surface Water and Bay of Bengal Water (Talley, 2011; Tomczak & Godfrey, 2003). Within the thermocline and intermediate-depth layers, two significant water masses are present: Indonesian Intermediate Water (IIW) and Red Sea Intermediate Water (RSIW). IIW originates from the Pacific Central Water and enters the Bay of Bengal through the Indonesian throughflow. In the Bay of Bengal, IIW circulates clockwise at thermocline levels (You, 1998). On the other hand, RSIW forms from the outflow of water from the Red Sea and Persian Gulf into the Arabian Sea. Due to its high salinity, RSIW can sink to depths of 400–1,400 m, and enter the Bay of Bengal around the southern tip of India and circulate in a clockwise direction (You, 1998). Indian Deep Water (IDW) is found between 1,500 and 3,800 meters. It is formed when the Circumpolar Deep Water mixes with the North Atlantic Deep Water (Tomczak & Godfrey, 2003). Below 3,800 meters, Antarctic Bottom Water only reaches the southern part of the Bay of Bengal (Tomczak & Godfrey, 2003).

### **2.2.3 The Andaman Sea**

The Andaman Sea is a marginal sea located to the east of the Bay of Bengal, separated from it by the Andaman and Nicobar Islands. The Andaman Sea connects to the Bay of Bengal through three main passages: the southern channel (the deepest, at about 1500 m), the middle channel (10 Degree Channel, with a depth of around 700 m), and the northern channel (the shallowest, at about 300 m) (Chatterjee et al., 2017; Rashid et al., 2019; Robinson et al., 2007).

The Andaman Sea has an average depth of about 2000 meters. Its salinity and stratification are influenced by freshwater inputs from the Irrawaddy and Salween rivers, low-salinity water from the BoB, and direct precipitation (Chatterjee et al., 2017; Rashid et al., 2019).

### 2.3 Separation of foraminifera tests from bulk marine sediments

We separated the foraminifera tests from the bulk marine sediments by soaking for 24 hrs, ~10 g of sediments in a solution of 180 ml Milli-Q water with 10 ml 10% sodium hexametaphosphate solution, and 10 ml 30 % hydrogen peroxide solution pH adjusted to ~8.2 with 1 M NaOH solution. We then washed it over a mesh size 63  $\mu\text{m}$  sieve with distilled water. Intermittently, we also applied ultra-sonication to remove the adhered clay particles from the foraminifera tests. Cleaned tests were then transferred to clean glass beakers and dried in a convection oven at 50°C. Dried foraminifera was sieved into size fractions of 63-150  $\mu\text{m}$ , 150-250  $\mu\text{m}$ , 250-355  $\mu\text{m}$ , 355-425  $\mu\text{m}$ , and > 425  $\mu\text{m}$  and kept in cleaned labelled vials. Later, identification and manual picking of the desired foraminifera species (> 250  $\mu\text{m}$  size fraction) was done under a zoom-type stereo microscope (**Figure 2.3**).

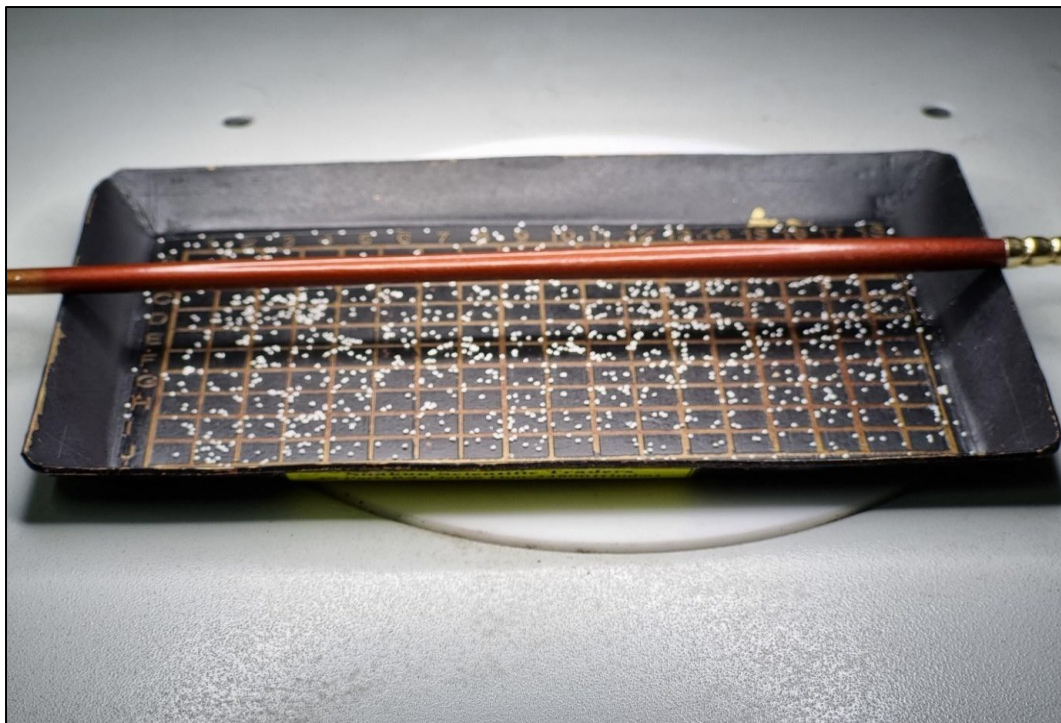


**Figure 2.3:** Photograph of foraminifera samples under a zoom-type stereo microscope (Photo Credit: Deepak Kumar Rai).

## 2.4 Description of Planktic foraminifera

The following is the description of the selected species of planktic foraminifer used in this thesis:

***Globigerinoides ruber*:** *Globigerinoides ruber* is the most common species in tropical and subtropical ocean waters. It hosts dinoflagellate symbionts. They are found in varying ecological conditions, from oligotrophic to eutrophic regions (Schiebel & Hemleben, 2017). It thrives in wide temperature (14-31 °C) and salinity (22-29 PSU) ranges.

***Trilobatus sacculifer*:** It is an abundant tropical to subtropical mixed layer dwelling species that is used extensively in paleoceanographic reconstructions (Schiebel & Hemleben, 2017). It is an euryhaline species thriving in salinities between 24 and 47 PSU and temperatures from 14 to 32 °C. *T. sacculifer* is a symbiont-bearing species, feeding mainly upon calanoid copepods. It reproduces on a synodic lunar cycle (Schiebel & Hemleben, 2017).

***Globorotalia menardii*:** It is a cosmopolitan species found mainly in tropical to sub-tropical waters, having low to medium productivity. The maximum standing stock of *G. menardii* is found at the deep chlorophyll maximum. It has been greatly used as a thermocline species in paleoceanographic reconstructions (Fairbanks, 1989; Schiebel & Hemleben, 2017; Stainbank et al., 2019). The diet of *G. menardii* consists of diatoms and chrysophytes. Its reproduction cycle follows a synodic lunar cycle (Schiebel & Hemleben, 2017).

***Globigerina bulloides*:** It typically resides above the thermocline in the upper 60 m of the water column. It is a non-symbiotic species commonly found in temperate to sub-polar waters and upwelling regions. Its distribution in surface waters can be influenced by hydrologic conditions and prey availability. Its diet mainly consists of algae (Schiebel & Hemleben, 2017).

The vertical distribution of these species depends upon their ecological preferences and behaviour. *Globigerinoides ruber* is a surface-dwelling species, predominantly occupying the top ~50 m. *Trilobatus sacculifer* is also a mixed-layer species but lives slightly deeper than *G. ruber* from ~40 to 130 m. *Globigerina bulloides* has a slightly broader depth range, mainly above the upper thermocline. *Globorotalia menardii* is a deep-dwelling species that predominantly dwells in the thermocline.

## 2.5 Radiocarbon dating

Establishing the chronology of the marine sediment cores is an essential aspect of any paleo reconstruction study as it provides the temporal variations that can be obtained. Depending upon the type of material and extent of age to be determined, various dating techniques can be employed to develop a chronology. In the present study, radiocarbon ( $^{14}\text{C}$ ) dating technique has been used to develop the chronology of the sediment cores from the Arabian Sea. In radiocarbon dating, the age of a sample is estimated by finding the remaining  $^{14}\text{C}$  atoms (radioactive isotope) with respect to its known half-life (Hua et al., 2009; Libby et al., 1949). Radiocarbon dating relies on the equilibrium established between the continuous production of  $^{14}\text{C}$  in the atmosphere, driven by the interaction of the high energy cosmic rays with  $^{14}\text{N}$ , and its gradual depletion due to radioactive decay. The newly produced  $^{14}\text{C}$  in the upper atmosphere oxidises into  $\text{CO}_2$  and mixes with the atmospheric  $\text{CO}_2$ . It is in a constant state of exchange within the various carbon reservoirs in living entities. When these entities cease to participate in the exchange process – whether due to natural causes or artificial reasons – the  $^{14}\text{C}$  present in them at the point of disconnection from the atmosphere begins decaying with a half-life of 5730 years, resulting in the formation of  $^{14}\text{N}$  (Hua et al., 2009).

The age of a sample can be determined with the information of the current ratio of  $^{14}\text{C}$  to  $^{12}\text{C}$ , along with the half-life of  $^{14}\text{C}$ . The specific activity in pre-industrial times is taken as a reference value for modern activity. This value is  $13.56 \text{ dpm (gC)}^{-1}$ , where dpm is decay per minute.

$$(^{14}\text{C}/^{12}\text{C})_t = (^{14}\text{C}/^{12}\text{C})_0 e^{-\lambda t}$$

Where  $(^{14}\text{C}/^{12}\text{C})_t$  is the residual abundance ratio at time ‘t’ and  $(^{14}\text{C}/^{12}\text{C})_0$  is the initial ratio. ‘t’ is the age of the sample, and ‘ $\lambda$ ’ is the characteristic decay constant ( $\lambda = 0.693/5730 \text{ yr}^{-1}$ ).

We measured  $^{14}\text{C}/^{12}\text{C}$  in milligram-level carbon with our in-house highly sensitive technique of Accelerator Mass Spectrometry (AMS) (Bhushan et al., 2019) at PRL Ahmedabad. With this technique, a sample can be dated up to the past 50,000–55,000 years (~8–10 half-lives).

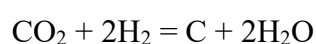
The Radiocarbon ( $^{14}\text{C}$ ) dating by AMS is a two-step process:

### (i) Graphitisation:

$^{14}\text{C}$  measurements by AMS require the sample to be converted into elemental carbon or graphite (a stable form of carbon) for producing stable and intense ion beams with a negligible memory effect in the ion source of AMS. Sample carbon needs to be converted to pure  $\text{CO}_2$  before the graphitisation process, and in this thesis work, we used cleaned planktonic foraminifera (fossils having shells of calcite) species *Globigerinoides ruber* and *Trilobatus sacculifer* for radiocarbon dating.

To perform radiocarbon measurement on foraminifera shells, around 10 mg of specimen were placed into 12 ml glass tubes sealed with screw caps equipped with butyl septa within a Carbonate Handling System (CHS) (Wacker et al., 2013). The glass tubes were flushed with a continuous flow of helium for 10 minutes to eliminate any atmospheric gases that may be present in the tubes. After flushing, 0.5 ml of phosphoric acid was injected into the glass tube using a gas-tight syringe. Subsequently, the samples were heated at  $850^\circ\text{C}$  for nearly one hour for the complete decomposition of foraminifera shells and the release of  $\text{CO}_2$ . The produced  $\text{CO}_2$  ( $\sim 1$  mg of carbon) was then carried through a helium stream to the Automated Graphitisation Equipment (AGE) for graphitisation, with any residual moisture being trapped by a phosphorus pentoxide trap along the way.

During the graphitisation process,  $\text{CO}_2$  is converted into graphite using hydrogen and iron (Wacker et al., 2010). The  $\text{CO}_2$  gas initially passes through a zeolite trap (equipped with a thermocouple-controlled heating wire) that absorbs and subsequently thermally releases  $\text{CO}_2$  into the reactors until the desired pressure is reached. After each set of samples, the trap is cleansed by heating it to  $500^\circ\text{C}$  while purging it with helium before loading the next batch of samples. The  $\text{CO}_2$  is then transferred to quartz reactor tubes (4.4 ml) that are vertically mounted to facilitate efficient gas mixing. Iron powder that acts as a catalyst in the graphitisation process is placed in the tubes. Before sample loading, the iron catalyst is conditioned and activated by heating with air, followed by reduction using pure hydrogen to remove any existing carbon species. The reactors are placed above a vertically adjustable electric oven. Optimal graphitisation conditions include a temperature of  $580^\circ\text{C}$  and an  $\text{H}_2/\text{CO}_2$  ratio of 2.3 (achieved by carefully introducing hydrogen) (Wacker et al., 2010). A simplified graphitisation process can be represented by Bosch reaction.



In summary, iron reduces  $\text{CO}_2$ , and hydrogen subsequently reduces the resulting  $\text{Fe}_3\text{O}_4$  back to Fe. This hydrogen-driven reduction regenerates iron within the system, enabling it to

function as a catalyst. Ultimately, graphite is coated on the iron powder during this graphitisation process. The water generated during graphitisation is frozen by a Peltier thermoelectric cooler. The sample graphite is later pressed into aluminium sample holder targets with copper pins and subsequently prepared for measurement in the AMS at PRL, Ahmedabad (AURiS) (Bhushan et al., 2019).

**(ii) Radiocarbon ( $^{14}\text{C}$ ) measurement by AMS:**

The radiocarbon measurement was performed with the 1MV AMS (PRL-AURiS) (**Figure 2.4**). This instrument can measure a  $^{14}\text{C}/^{12}\text{C}$  ratio up to  $3.9 \times 10^{-16}$  in a small carbon sample ( $\sim 0.3$  to  $1\text{mg C}$ ). Multiple standards and blanks were prepared and measured with the samples. Radiocarbon reference materials FIRI-E, IAEA-C2, and FIRI-C were measured along with samples to check the efficiency of the graphitisation process and isotopic measurement.

Graphite prepared from the samples and standards was then pressed into a cylindrical cavity of an aluminium holder called a target. These targets were affixed to the sample carousel, located in the source part of the AMS, and subsequently subjected to evacuation to achieve high vacuum levels within the range of  $10^{-5}$  to  $10^{-6}$  millibar.

It is widely recognised that the radiocarbon dating of marine shells can be affected by the reservoir effect of the ocean, leading to radiocarbon ages significantly older than terrestrial samples in most regions. On a global scale, marine fossils' radiocarbon ages of the surface ocean (up to  $\sim 200$  m depth) are observed to be 400 years. This age discrepancy arises because the carbon source for these foraminifera shells has lower  $^{14}\text{C}/^{12}\text{C}$  ratios than the atmosphere. This discrepancy is due to mixing the deeper ocean waters with depleted  $^{14}\text{C}$  content with surface waters (Stuiver & Braziunas, 1993). It is important to note that the reservoir ages can vary from one basin to another; therefore, when calibrating AMS radiocarbon ages, a reservoir age correction is necessary to estimate sample ages accurately.

We calibrated the AMS radiocarbon ages of SK-364/03 and SK-364/13 to calendar ages by CALIB 8.2 (Stuiver et al., 2021) with a reservoir age correction  $\Delta R$  as  $78 \pm 18$  years (Dutta et al., 2001; von Rad et al., 1999) and  $-30 \pm 64$  years (Southon et al., 2002), respectively. Bayesian age-depth models for both cores were developed using the 'Bacon' software, which operates in the R environment and employs Markov Chain Monte Carlo (MCMC) sampling techniques to assess calibrated age distributions. Sedimentation rates were also determined from the same calibrated ages. For SK-364/03, the sample resolution is 440 years. Whereas the sample resolution for SK-364/13 is 700 years.

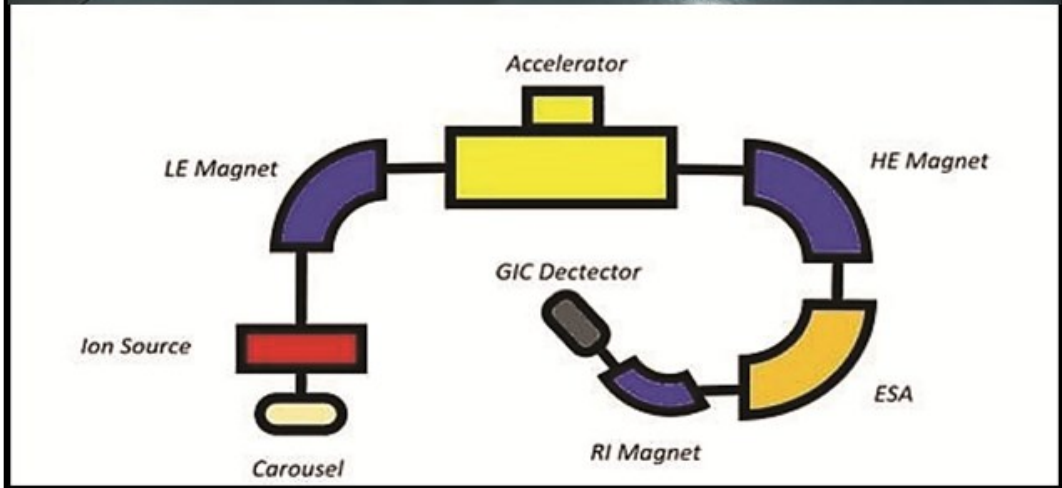


**Figure 2.4:** Photograph of AMS facility at Physical Research Laboratory, Ahmedabad, India (top). Schematic of the PRL–AURiS (bottom) (Bhushan et al., 2019).

## 2.6 Elemental and isotopic analysis of Total Organic Carbon and Total Nitrogen

We have measured the elemental and isotopic composition of TOC and total nitrogen (TN) for the sediment cores SK-364/03 and SK-364/13 in an Elemental analyzer (Flash, 2000) interfaced with a Delta V Isotope Ratio Mass Spectrometer (Thermo Scientific) through Conflo IV (**Figure 2.5**) in Geosciences-Stable Isotopes Laboratory (GeoSIL) at the Physical Research Laboratory, Ahmedabad, India. The sample processing for TOC and TN concentration and their isotopic composition follows different protocols.



**Figure 2.5:** Photograph of Flash 2000 elemental analyzer interfaced with Delta V IRMS through Conflo IV at GeoSIL, PRL, Ahmedabad, India (Photo Credit: Deepak Kumar Rai).

### 2.6.1 Sample processing:

We initially dried the sediment samples at 50°C to be analysed for their elemental and isotopic composition. We then powdered and homogenised the dried sediment samples using

an agate mortar and pestle. For TOC and its isotopic analysis ( $\delta^{13}\text{C}_{\text{org}}$ ), inorganic carbon (carbonates) has to be removed from the bulk sediment sample. Removal of inorganic carbon was achieved by decarbonating the bulk sediment samples using 1N HCl. For this purpose, an aliquot (around 1 g) of the powdered sediment sample was taken into centrifuge tubes and treated with 1 N HCl. Each sample was then ultra-sonicated for around 1 hour at 80°C with manual shaking after every 10 – 15 minutes. After removing carbonates from the sample, it was rinsed with ultrapure water (Milli-Q) 3 – 4 times. The acidified supernatant was removed by centrifuging each sample at 4500 rpm. The decarbonated sample was then dried at 50°C and homogenised using an agate mortar and pestle. For TN and its isotopic analysis ( $\delta^{15}\text{N}$ ), powdered and homogenised sample was directly used without decarbonating.

### 2.6.2 $\delta^{15}\text{N}$ and $\delta^{13}\text{C}_{\text{org}}$ measurements of the bulk sediments

For  $\delta^{15}\text{N}$  and  $\delta^{13}\text{C}_{\text{org}}$  analysis in the bulk sediments, we tightly packed around 5 – 10 mg of decarbonated sample for carbon and around 70 – 110 mg of bulk sediment sample for nitrogen into ultraclean tin capsules. Packed samples are introduced inside a heated reactor (at 1020°C) containing specialised reagents like chromium oxide and silver cobaltous oxide. The samples are flash combusted in this oxidation reactor in the presence of pure  $\text{O}_2$  pulse under inert conditions. The released gas, while passing through the oxidation reactor, produces carbon dioxide ( $\text{CO}_2$ ), water ( $\text{H}_2\text{O}$ ), nitrogen ( $\text{N}_2$ ), and various oxides of nitrogen ( $\text{NO}_x$ ). These gases further pass through a reduction quartz reactor (containing pure copper granules) with the help of helium gas (carrier gas), where oxides of nitrogen are reduced to  $\text{N}_2$ . Later, after passing through a moisture trap (containing magnesium perchlorate), the final output will be a mixture of  $\text{N}_2$  and  $\text{CO}_2$ . This gas mixture then passes through a GC column, separating gases based on their properties and retention time. The separated gases are later injected into the Delta V IRMS through ConFlo IV, and the isotopic composition of the samples is measured—the nitrogen isotopic composition of a sample represented by  $\delta^{15}\text{N}$ .

$$\delta^{15}\text{N} (\text{‰}) = (\text{R}_{\text{sample}} / \text{R}_{\text{standard}} - 1) \times 1000;$$

where  $\text{R}_{\text{sample}}$  and  $\text{R}_{\text{standard}}$  refer to the  $^{15}\text{N}/^{14}\text{N}$  abundance ratio in the sample and standard, respectively. The Standard is atmospheric  $\text{N}_2$ .

In the present study, the reference gas cylinder was calibrated daily with IAEA-N-2 (Ammonium Sulphate);  $\delta^{15}\text{N} = 20.30 \pm 0.2\text{‰}$ ; N content ~ 21.2 %. Protein (Casein) was used as an in-house reference standard and ran after every four samples. Analytical precision based on the repeat analysis of protein standard was better than 0.2‰.

The carbon isotopic composition of a sample represented by  $\delta^{13}\text{C}$ .

$$\delta^{13}\text{C} (\text{‰}) = (\text{R}_{\text{sample}} / \text{R}_{\text{standard}} - 1) \times 1000;$$

where  $\text{R}_{\text{sample}}$  and  $\text{R}_{\text{standard}}$  refer to the  $^{13}\text{C}/^{12}\text{C}$  abundance ratio in the sample and standard, respectively. The standard is Vienna Pee Dee Belemnite (VPDB).

Cellulose (IAEA -CH-3;  $\delta^{13}\text{C} = -24.7 \pm 0.1\text{‰}$ ; C content  $\sim 44.4\%$ , and IAEA-C-3;  $\delta^{13}\text{C} = -24.62 \pm 0.1\text{‰}$ ; C content  $\sim 44.4\%$  (recalibrated with IAEA-CH-3) were used as standards for carbon isotopic analysis. Standards and blanks were run after every five samples. Analytical precision based on the repeat analysis of the reference standard was better than  $0.1\text{‰}$ .

### 2.6.3 TOC and TN concentration measurement

The TOC (weight %) and TN (weight %) in bulk sediment samples were calculated using a calibration curve (straight line) generated using standards of known %C (IAEA-CH-3 and IAEA-C-3 (cellulose standard): 44.4%) and %N (IVA-OAS protein: 13.32% and IAEA-N-2 (Ammonium sulphate); 21.2%) against total area under the curve for respective masses ( $\text{CO}_2$  and  $\text{N}_2$ ) using the same elemental analyser attached to IRMS. The analytical precisions for TOC (weight %) and TN (weight %) contents were better than 5 % for repeat measurements.

## 2.7 Element/Calcium ratio measurement on foraminiferal test

We measured various I/Ca, Mg/Ca, Sr/Ca, Cd/Ca, Ba/Ca, Na/Ca, Mn/Ca, Fe/Ca, and Al/Ca on *Trilobatus sacculifer* from both the sediment cores along with core-top sediments using Thermo<sup>®</sup> Element XR (HR-ICP-MS) (**Figure 2.6**). Due to paucity of abundant number of shells of any species of foraminifera from the plankton tow samples, element/calcium was measured on mixed species from the upper water column. Element/Calcium ratio measurement protocols were set up at the Physical Research Laboratory, Ahmedabad, India. From here on we will be using multi-element/calcium ratio (Me/Ca) for Mg/Ca, Sr/Ca, Cd/Ca, Ba/Ca, Na/Ca, Mn/Ca, Fe/Ca, and Al/Ca measured in acidic medium.



**Figure 2.6:** Thermo® Element XR (HR-ICP-MS) at PRL, Ahmedabad, India, used for trace elemental analysis in this study (Photo Credit: Deepak Kumar Rai).

### 2.7.1 Reagents and labware

We prepared all reagents and standards in a clean Laboratory under a laminar flow bench. Nalgene® Teflon® bottles that had been pre-cleaned by boiling in a solution of 7 M HNO<sub>3</sub> were used for storing standard solutions. Pre-cleaned polypropylene tubes (leached in 2 N HCl) were used for working standard preparation and sample analysis. We used 18.2 Mega-Ohm Milli-Q water with ultrapure HNO<sub>3</sub> (Optima Grade, Fisher Scientific) to prepare all the acids, ICP-MS standards, and samples. NH<sub>4</sub>OH (25%, Suprapur grade, Merck) was used as an iodine stabiliser. Sample cleaning and dissolution were carried out in 1.5 ml polypropylene microcentrifuge tubes, cleaned by leaching in 2N HCl and then thoroughly rinsed multiple times in ultrapure water.

### 2.7.2 I/Ca and multi-element/Ca standard preparation

External standards with fixed Ca concentration and variable Mg, Sr, Mn, Cd, Fe, Ba, Na, and Al concentrations were prepared gravimetrically using high-purity single-element standards (Certipur®, Merck). A high concentration (10,000 mg L<sup>-1</sup>) Ca standard was used for preparing the stock solutions. For other elements, standards having a concentration of 1000 mg L<sup>-1</sup> were utilised. Concentrated stock solutions were prepared at 200 ppm Ca in 2 % (v/v) HNO<sub>3</sub>

(Optima Grade, Fisher Scientific), with other element concentrations representing the typical oceanic ranges of foraminifera. Trace element impurities in the Ca solution are significant concerning foraminiferal concentrations. Therefore, all elements of interest were determined by standard addition and incorporated into the standard calculations. Calibration standards for ICP-MS analysis were prepared from the stock solutions by diluting to 25 ppm Ca using the same 2 % HNO<sub>3</sub> used for sample analysis on the day of sample analysis. Consistency and bracketing standards were also prepared in the same way.

Stock standard solution for iodine was gravimetrically prepared from trace metal basis Potassium iodate (99.995 %, Sigma–Aldrich) by dissolving in ultrapure water (Milli-Q) and adding up concentrated HNO<sub>3</sub> and NH<sub>4</sub>OH to make up 1 % HNO<sub>3</sub> and 0.5 % NH<sub>4</sub>OH in the final stock standard solution. The stock standard was used to prepare working standards after three steps of pre-dilutions. A 1:1 mix of 2 % HNO<sub>3</sub> and 1 % NH<sub>4</sub>OH was used for dilutions. Calibration, check, and bracketing standards were prepared directly in the analysis vials. Working standards (Calibration, check, and bracketing standards) were prepared by doping the multi-element standards prepared previously with the third dilution of the iodine standard in appropriate concentrations that mimic the typical values of foraminifera. These I/Ca analysis standards were prepared at 50 ppm Ca concentration for sediment core samples, and at 40 ppm Ca for the plankton tow and core-top planktic foraminifera due to less number of shells found. Every standard for iodine analysis was freshly prepared daily, just before analysis. Care was taken to matrix and pH match all the working standards with the samples.

### 2.7.3 Mass spectrometry

Iodine and other elements of interest were analysed at the PRL, Ahmedabad, India, on a Thermo® Element XR. It is a single collector sector field high-resolution inductively coupled plasma mass spectrometer (HR-ICP-MS). Instrumental settings for all the analyses are listed in **Table 2.4**.

Me/Ca ratio measurements by Element XR were done using a set of external calibration standards. Samples were analysed at a fixed calcium concentration of 25 ppm for Me/Ca, 50 ppm Ca for I/Ca of sediment core samples, and 40 ppm Ca for I/Ca of core-top and plankton tow foraminifera shells. Before ICP-MS Me/Ca and I/Ca analysis, samples were analysed for their calcium concentration and then appropriately diluted to a fixed Ca concentration to matrix match the samples and the standards. Me/Ca analysis was carried out in 2 % HNO<sub>3</sub>, while I/Ca

analysis was done in a basic medium (pH ~8.5) to stabilise iodine in the sample solution and also improve the washout of the spray chamber.

**Table 2.4:** ICP-MS settings for measuring Me/Ca and I/Ca.

Parameter	Trace element mode
Plasma RF power	1250 W
Nebulizer	MicroMist Nebulizer 200 $\mu\text{l min}^{-1}$
Spray chamber	Twinnabar Spray chamber with Helix CT
Injector	2.0 mm Quartz Injector
Sample cone	Ni
Skimmer cone	Ni
Sample matrix	2 % $\text{HNO}_3$ (for Me/Ca) and 2 % $\text{HNO}_3$ + 1 % $\text{NH}_4\text{OH}$ (for I/Ca)
Uptake time	70 s
Analysis time	150 s (for Me/Ca) and 120 s (for I/Ca)
Washout time	80 s
Mass resolution	Low and medium
Runs	3 (LR), 3 (MR)
Passes	15 (LR), 3 (MR)
Detection mode	Triple

The ICP-MS sensitivity was optimised daily in low mass resolution ( $\Delta m/m = 300$ ) mode using a one ppb/analyte multi-element tune solution. A minimum sensitivity of 1,500,000 cps/ppb on  $^{115}\text{In}$  was set as operational criteria. Medium resolution ( $\Delta m/m = 4000$ ) tuning was done using  $^{56}\text{Fe}$ . Detector cross-calibration was done daily between pulse and analog modes. Mass bias discrimination was done using a foraminiferal matrix-matched solution before sample analysis. Samples were analysed in blocks of six with a pair of acid blanks and internal bracketing standards bracketing each block. Internal consistency standards and external standards were also analysed with each block of samples. The detailed method for each isotope of the analytes for Me/Ca and I/Ca analysis are given in **Table 2.5** and **Table 2.6**, respectively.

**Table 2.5:** ICP-MS method for Me/Ca analysis in 2% HNO<sub>3</sub> medium.

Isotope	Mass Resolution	Mass Window	Sample Time (s)	Samples Per Peak	Integration Window	Detection Mode
<sup>25</sup> Mg	Low	10	0.01	50	5	Analog
<sup>27</sup> Al	Low	10	0.01	50	5	Analog
<sup>43</sup> Ca	Low	10	0.02	50	5	Analog
<sup>87</sup> Sr	Low	10	0.04	50	5	Analog
<sup>111</sup> Cd	Low	15	0.02	200	10	Counting
<sup>137</sup> Ba	Low	10	0.02	50	5	Triple
<sup>23</sup> Na	Medium	100	0.02	25	50	Triple
<sup>43</sup> Ca	Medium	100	0.01	25	50	Triple
<sup>55</sup> Mn	Medium	100	0.01	25	50	Triple
<sup>56</sup> Fe	Medium	100	0.05	25	50	Triple

**Table 2.6:** ICP-MS method for I/Ca analysis in basic medium (2 % HNO<sub>3</sub> + 1 % NH<sub>4</sub>OH).

Isotope	Mass Resolution	Mass Window	Sample Time (s)	Samples Per Peak	Integration Window	Detection Mode
<sup>25</sup> Mg	Low	20	0.03	50	20	Triple
<sup>27</sup> Al	Low	20	0.001	50	20	Triple
<sup>43</sup> Ca	Low	150	0.027	30	80	Triple
<sup>87</sup> Sr	Low	150	0.043	30	80	Triple
<sup>127</sup> I	Low	20	0.028	100	20	Triple

#### 2.7.4 Cleaning procedure for foraminifera tests

We manually picked foraminifera tests under a zoom-type stereo microscope with minimal or no signs of diagenetic alteration or authigenic mineral deposits. Around 100 shells of *Trilobatus sacculifer* from the 355-425 µm size fraction were picked. These shells were chemically cleaned following the oxidative cleaning protocol (Barker et al., 2003; Winkelbauer et al., 2021). Shells were gently cracked open between two glass slides and then loaded into acid-leached 1.5 ml microcentrifuge tubes for further cleaning in a clean laboratory under a laminar flow bench. Fragmented shells (in the microcentrifuge tubes) were ultra-sonicated for one minute in ultrapure (Milli-Q) water (four times), methanol (two times), and again in ultrapure (Milli-Q) water (two times) to remove any clay particles adhered to the shells. After the clay removal step, the shells were oxidatively cleaned. An oxidative reagent (an alkali

buffered 1 % H<sub>2</sub>O<sub>2</sub>) was added to the samples, and then samples were kept in boiling water for 15 minutes with intermittent ultra-sonication for 30 seconds. This step was repeated four times to remove any organic matter that may have adhered to the shells. Subsequently, the samples were rinsed (three times) with ultrapure (Milli-Q) water to remove any remaining oxidative reagent. Now, shells were transferred to new acid-leached microcentrifuge tubes. A weak acid (0.001 N HNO<sub>3</sub>) leach in assistance with ultrasonication was performed on each sample for 30 seconds to remove any chemisorbed elements from the surface of the calcite. Finally, samples were rinsed with ultrapure water (three times) to de-acidify the samples.

### 2.7.5 Foraminifera sample analysis

Cleaned samples were dissolved in 1 ml 2 % HNO<sub>3</sub> prepared from Ultrapure HNO<sub>3</sub> (Optima Grade, Fisher Scientific). Samples were ultra-sonicated for a few minutes to aid the sample dissolution process. After that, samples were centrifuged for 5 minutes at 10,000 rpm, and the supernatant was used for analysis. The first aliquot of 20 µl was used for the initial calcium concentration check using Indium as an internal standard. A second aliquot of 0.68 ml was used for I/Ca analysis, measuring <sup>127</sup>I and <sup>43</sup>Ca after diluting samples at a fixed calcium concentration of 50 ppm for sediment core planktic foraminifera tests and at 40 ppm Ca for the plankton tow and core-top planktic foraminifera due to less number of shells found. As Iodine is volatile in an acidic medium, it was stabilised using 0.68 ml of 1% NH<sub>4</sub>OH. I/Ca analysis was performed using pH and matrix matching of samples and freshly prepared Iodine calibration standards. 2% HNO<sub>3</sub> and 1% NH<sub>4</sub>OH mixture (1:1) was used to pH match (~8.5) both samples and standards. The third aliquot of 0.26 ml was used to measure Mg, Mn, Al, Fe, Cd, Ba, Sr, Na, and Ca at a fixed calcium concentration of 25 ppm in 2% HNO<sub>3</sub>. Rest all the supernatant was discarded. Al/Ca, Fe/Ca, and Mn/Ca were measured to evaluate whether foraminifera shells are free from clay, silicate and Mn-Fe hydroxide contamination that may interfere with the pristine foraminifera calcite.

In total, 164 (92 for SK-364/03 and 72 for SK-364/13) samples were analysed for Me/Ca ratios, and 110 (55 for SK-364/03 and 46 for SK-364/13) samples were analysed for I/Ca ratios. Al/Ca ratios below 100 µmol mol<sup>-1</sup> in most samples (144 out of 164), with no covariance of Al/Ca with Mg/Ca ratios, indicated that there was no clay and silicate contamination (**Figure 2.7** (a) and (d)). Fe/Ca ratios did not show any covariance with Mg/Ca ratios (**Figure 2.7** (b) and (e)), suggesting an effective cleaning of foraminiferal tests (Barker et al., 2003). In addition, Mn/Ca ratios were well below 1 mmol mol<sup>-1</sup> and showed no

covariance with the Mg/Ca ratios of SK-364/03 (**Figure 2.7 (c)**) and a weak negative covariance with Mg/Ca ratios of SK-364/13 (**Figure 2.7 (f)**), indicating efficient cleaning of foraminifera tests (Barker et al., 2003).

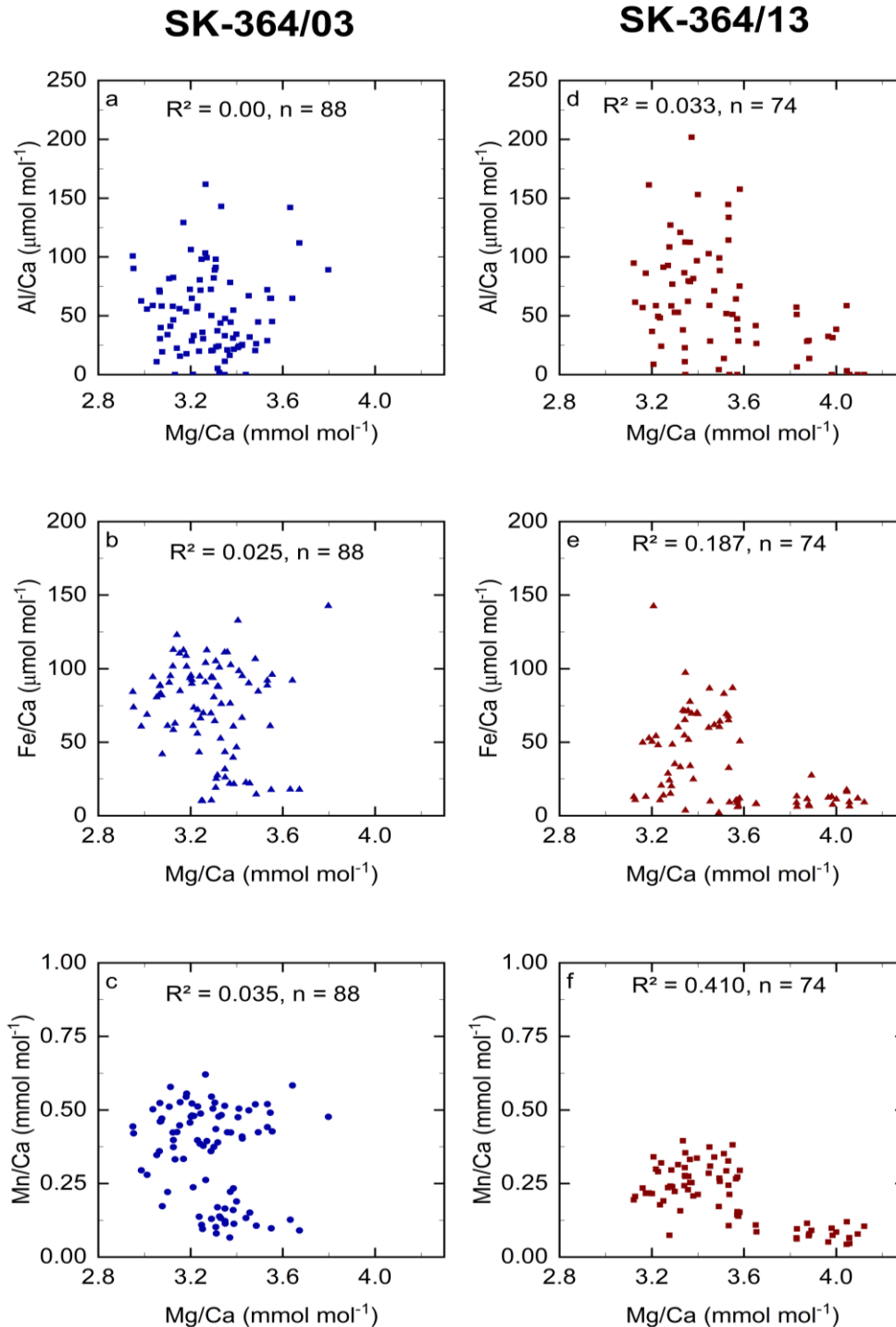


**Figure 2.7:** Correlation plots of (a,d) Mg/Ca with Al/Ca; (b,f) Mg/Ca with Fe/Ca; and (c,e) Mg/Ca with Mn/Ca of SK-364/03, and SK-364/13, respectively. The coefficient of variation ( $R^2$ ) and number of samples ( $n$ ) are shown in each panel. None of the positive correlations are significant at  $p < 0.05$  - suggesting effective cleaning of tests.

### 2.7.6 Analytical precision and accuracy

The long-term analytical precision of I/Ca and Me/Ca was obtained by measuring internal consistency standards at regular intervals (**Table 2.7** and **Table 2.8**).

**Table 2.7:** Long-term analytical precision of internal consistency standards for Me/Ca in 2% HNO<sub>3</sub> medium.

Me/Ca	Calculated Value	Measured Value (Mean)	Standard deviation ( $\pm 1\sigma$ ) (n=15)	% RSD
Mg/Ca (mmol mol <sup>-1</sup> )	4.05	4.05	0.02	0.43
Al/Ca ( $\mu\text{mol mol}^{-1}$ )	208.41	205.17	3.48	1.70
Sr/Ca (mmol mol <sup>-1</sup> )	1.70	1.70	0.01	0.44
Cd/Ca ( $\mu\text{mol mol}^{-1}$ )	0.26	0.26	0.00	1.27
Ba/Ca ( $\mu\text{mol mol}^{-1}$ )	10.06	10.22	0.38	3.68
Na/Ca (mmol mol <sup>-1</sup> )	6.87	6.83	0.04	0.64
Mn/Ca ( $\mu\text{mol mol}^{-1}$ )	276.20	284.39	1.28	0.45
Fe/Ca ( $\mu\text{mol mol}^{-1}$ )	101.41	99.38	1.34	1.35

**Table 2.8:** Long-term analytical precision of internal consistency standards for I/Ca in basic medium (2 % HNO<sub>3</sub> + 1 % NH<sub>4</sub>OH).

Me/Ca	Calculated Value	Measured Value (Mean)	Standard deviation ( $\pm 1\sigma$ ) (n=18)	% RSD
I/Ca ( $\mu\text{mol mol}^{-1}$ )	4.36	4.38	0.05	1.12

ECRM 752-1 is a limestone standard previously used for comparing Mg/Ca measurements and was analysed at regular intervals. Its analytical precision and accuracy are reported in **Table 2.9**.

**Table 2.9:** Mg/Ca ratios of an international standard measured with samples.

<b>Standard</b>	<b>Statistics</b>	<b>Mg/Ca (mmol mol<sup>-1</sup>)</b>
ECRM 752-1	Consensus value	3.749
	Measured Value	3.714
	( $\pm 1\sigma$ )	0.057
	% RSD	0.77
	(n=28)	

For I/Ca analysis, JCp-1 (coral, aragonite) has been previously used for comparability between laboratories, but it was never certified for I/Ca due to its heterogeneity. Also, Japan has banned its trade due to the Convention on International Trade in Endangered Species of Wild Fauna and Flora. So, due to its unavailability, it could not be used for this study.

# Chapter 3

## Proxy validation of iodine to calcium ratios from plankton tow and core-top foraminifera

### 3.1 Introduction

Ocean deoxygenation poses a serious threat to the marine ecosystems and may alter the pattern of biogeochemical processes (Breitburg et al., 2018). The existing studies as well as model projections indicate that OMZs will likely expand further in the future as global warming persists (Stramma et al., 2010). However, the exact knowledge about its magnitude and extent regulated by oceanographic or biogeochemical processes in the both contemporary and past ocean is still lacking. Consequently, it becomes imperative to employ sedimentary proxies to trace past OMZs, as this is vital for gaining insights into OMZ dynamics and enhancing the accuracy of future predictions.

Various proxies have been used to infer the O<sub>2</sub> levels in OMZ, such as the presence/absence of sedimentary laminations, redox-sensitive metals (e.g. U, Mo, Fe, Mn etc.), benthic foraminifera assemblages and morphology, and nitrogen isotopes (Erdem et al., 2020; Kast et al., 2019; Rathburn et al., 2018). However, most of these proxies are limited to continental margins immersed in low O<sub>2</sub> waters, limiting the areal extent of reconstruction. I/Ca ratios in planktic foraminifera is an emerging proxy that has the potential to infer the dissolved O<sub>2</sub> changes in the open ocean (Hoogakker et al., 2018; Lu et al., 2020; Lu et al., 2016; Zhou et al., 2014).

I/Ca ratios in planktic foraminifera is based on the redox-sensitive behavior of iodine in the ocean water column, which is incorporated in the carbonate shells of marine planktonic organisms (Lu et al., 2010). In the ocean, iodine mainly exists in two thermodynamically stable forms: Iodate (IO<sub>3</sub><sup>-</sup>), the oxidised form, whereas in low O<sub>2</sub> conditions, IO<sub>3</sub><sup>-</sup> is reduced to iodide (I<sup>-</sup>) (Lu et al., 2010; Rue et al., 1997). It has been suggested that only IO<sub>3</sub><sup>-</sup> is incorporated into the calcite crystal lattice (Lu et al., 2010). IO<sub>3</sub><sup>-</sup> in the calcite crystal is linked to three additional

O atoms and is incorporated through the charged coupled substitution  $\text{IO}_3^- + \text{Na}^+ \leftrightarrow \text{CO}_3^{2-} + \text{Ca}^{2+}$ , with the  $\text{Na}^+$  cation at the nearest  $\text{Ca}^{2+}$  site being the most energetically favourable configuration (Podder et al., 2017). This substitution causes local distortions of the structure over a length scale of around  $10 \text{ \AA}$  (Feng & Redfern, 2018).

Planktic foraminifera inhabit various depths in the ocean, from the mixed layer to the upper thermocline, and sometimes for specific species in the OMZs (Schiebel & Hemleben, 2017). As such, the planktic foraminifera living in the top layer can efficiently capture the I/Ca signature and thus can be used to assess ocean oxygenation in the upper water column in the open ocean. Previous core-top calibrations studies suggest that regions with extensive suboxia have very low planktic foraminifera I/Ca ratios ( $< 1 \mu\text{mol mol}^{-1}$ ) compared to well-oxygenated regions with I/Ca ratios  $> 4 \mu\text{mol mol}^{-1}$  (Lu et al., 2020; Lu et al., 2016).

Planktic foraminifera I/Ca have recently been utilised qualitatively or semi-quantitatively across various time scales (Hess et al., 2023; Hoogakker et al., 2018; Lu et al., 2016). Recently, based on the I/Ca ratio, it has been suggested that during the glacial times the Pacific sector of the Southern Ocean, which is well known for sustaining high  $\text{O}_2$  levels throughout the year, had  $\text{O}_2$  levels decreased up to  $70 \mu\text{mol kg}^{-1}$  in the subsurface waters (Lu et al., 2016) together with the downward expansion of the OMZ in the Eastern Tropical North Pacific (Hoogakker et al., 2018). Similarly, the I/Ca ratio also revealed that the Eastern Tropical Pacific, which is known for the prevalence of OMZ conditions in present times, was well-oxygenated and crossed over  $\sim 100 \mu\text{mol kg}^{-1}$  during the warm Miocene period (Hess et al., 2023). As such, the I/Ca ratio of planktonic foraminifera proved to be a reasonable proxy to reconstruct the paleo  $\text{O}_2$  levels of the past ocean on a range of decadal to geological time scale.

Until now, three core-top calibration studies have been attempted to determine the relationship between planktic foraminifera I/Ca and dissolved  $\text{O}_2$  (Lu et al., 2020; Lu et al., 2016; Winkelbauer, 2022). I/Ca values from the plankton tow samples have also been reported from the Eastern Tropical North Pacific, Benguela current region, and the North and South Atlantic Ocean (Winkelbauer et al., 2023). However, plankton tow I/Ca has been reported from only one location of the Eastern Tropical North Pacific, which has intense OMZ. Therefore, in terms of plankton tow I/Ca, intense OMZs remain less explored. The northern Indian Ocean, characterised by low dissolved  $\text{O}_2$  concentration in the intermediate depths, can be a suitable region for exploring plankton tow I/Ca in intense OMZ. Furthermore, planktic foraminifera I/Ca from core-top have been reported only for a few sites in the Arabian Sea (Winkelbauer,

2022). Thus, to understand the applicability of I/Ca in planktic foraminifera in the northern Indian Ocean, we measured I/Ca in planktic foraminifera from the core tops and plankton tows.

### 3.2 Methods

In this work, we have used samples from twelve locations in the northern Indian Ocean. The nine core-top sediments and eleven plankton tow samples were collected from the northern Indian Ocean (Figure 3.1).

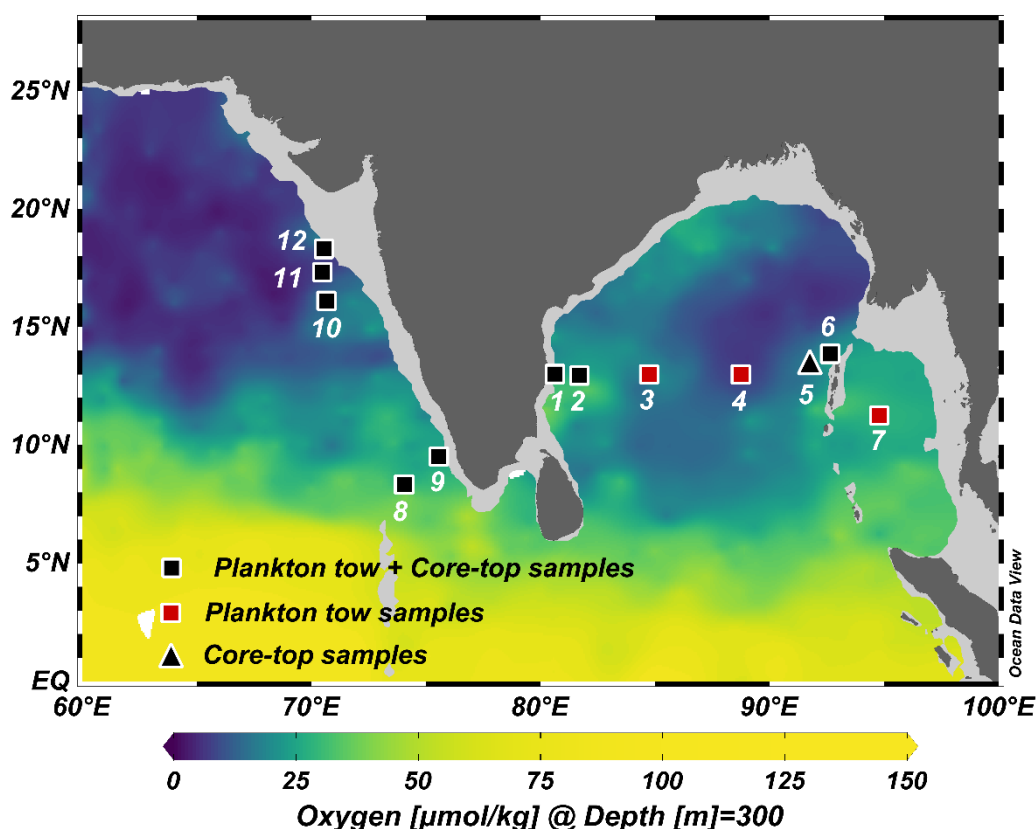


**Figure 3.1:** Map showing the sample locations of the core-top and plankton tow samples superimposed over dissolved O<sub>2</sub> concentrations at 300 m depth. The data source for dissolved O<sub>2</sub> is World Ocean Atlas 2018.

We measured I/Ca ratios on planktic foraminifera tests from both the core-top sediments and the plankton tow samples using HR-ICPMS. Due to the paucity of foraminifera tests in the plankton tow samples, we measured I/Ca on a single species wherever tests were abundant enough. For the rest of the locations with scarce samples, the I/Ca ratio in the plankton tow was determined based on mixed species (*Trilobatus sacculifer*, *Globigerina bulloides*, and

*Globorotalia menardii*). For core-top samples, we measured I/Ca on *Trilobatus sacculifer* as well on mixed species (*Trilobatus sacculifer*, *Globigerina bulloides*, and *Globorotalia menardii*). In mixed species, similar number of tests of each species were taken in each sample to avoid species-specific bias in I/Ca measurement. Since organic matter contamination can be a significant contributor of iodine in foraminifera shells, the oxidative cleaning step was repeated six times for both core-top and plankton tow foraminifera tests (Winkelbauer et al., 2023). The details of the sampling locations and analytical techniques adopted for I/Ca measurements are described in Chapter 2.

We have also compiled all the previous core-top I/Ca measurements with our new measurements and compared them with the minimum dissolved O<sub>2</sub> concentration in the water column for proxy validation purposes. We have incorporated the errors in both variables and performed the weighted linear regression. We have taken the objectively analysed climatological averaged dissolved O<sub>2</sub> concentration from the 1° gridded data of the World Ocean Atlas 2018. The in-situ O<sub>2</sub> measurements alongside the plankton tow samples couldn't be performed for the present work. The samples with exceptionally low I/Ca and high O<sub>2</sub> concentration that have been previously reported to be of older age are excluded from the study (Winkelbauer, 2022).

### 3.3 Results

#### 3.3.1 Plankton tow and core-top planktic foraminifera I/Ca

I/Ca ratios in plankton tow derived foraminifera varied from below the detection limit to 0.57  $\mu\text{mol mol}^{-1}$  in the northern Indian Ocean (**Table 3.1**). Except for four locations, all other locations have I/Ca values within one sigma standard deviation of the internal laboratory standard. This suggests that although these I/Ca values are detectable, they are not discernible from each other. I/Ca values for *Trilobatus sacculifer* and mixed species are similar. I/Ca values of the planktic foraminifera from the core-tops varied between 0.03 to 2.11  $\mu\text{mol mol}^{-1}$  (**Table 3.2**). Three out of nine locations have I/Ca values near the detection limit. I/Ca values of mixed planktic foraminifera are either similar or less than that of *Trilobatus sacculifer*. Plankton tow foraminifera I/Ca values are either similar or less than that of the core-top I/Ca (**Figure 3.2**).

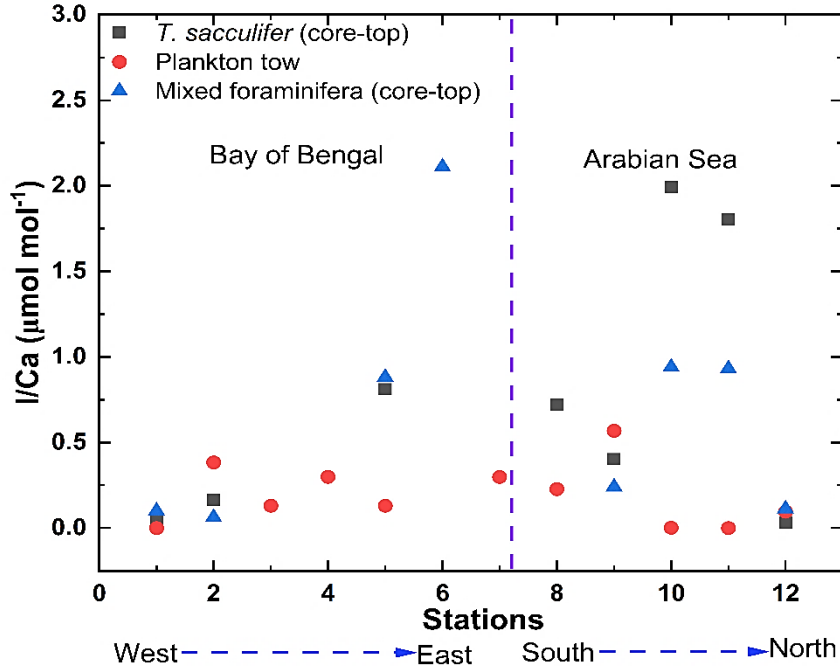


**Figure 3.2:** Plot showing I/Ca ( $\mu\text{mol mol}^{-1}$ ) ratios in plankton tow and core-top foraminifera.

**Table 3.1:** I/Ca values of the plankton tow derived planktic foraminifera.

S.No.	Sample ID	Species	I/Ca ( $\mu\text{mol mol}^{-1}$ )
1	SK-373/01	<i>Trilobatus sacculifer</i>	*
		Mixed	*
2	SK-373/02	<i>Trilobatus sacculifer</i>	0.13
		Mixed	0.02
3	SK-373/03	Mixed	0.30
4	SK-373/04	<i>Trilobatus sacculifer</i>	0.17
5	SK-373/05	Mixed	0.16
6	SK-373/06	Mixed	0.38
7	SK-374/01	Mixed	0.57
8	SK-374/02	Mixed	0.23
9	SK-374/03	Mixed	0.10
10	SK-374/04	<i>Trilobatus sacculifer</i>	*
		Mixed	*
11	SK-374/05	Mixed	*

\*Below detection limit.

**Table 3.2:** I/Ca values of the planktic foraminifera from the core-top sediments.

S.No.	Sample ID	Species	I/Ca ( $\mu\text{mol mol}^{-1}$ )
1	SK-373/SP-01	<i>Trilobatus sacculifer</i>	0.05
		Mixed	0.10
2	SK-373/SP-02	<i>Trilobatus sacculifer</i>	0.81
		Mixed	0.88
3	SK-373/SP-03	<i>Trilobatus sacculifer</i>	0.17
		Mixed	0.06
4	SK-373/GC-02	Mixed	2.11
5	SK-374/SP-01	<i>Trilobatus sacculifer</i>	0.40
		Mixed	0.24
6	SK-374/SP-02	Mixed	0.72
7	SK-374/SP-03	<i>Trilobatus sacculifer</i>	0.03
		Mixed	0.11
8	SK-374/SP-04	<i>Trilobatus sacculifer</i>	1.80
		Mixed	0.93
9	SK-374/SP-05	<i>Trilobatus sacculifer</i>	1.99
		Mixed	0.94

### 3.3.2 Core-top I/Ca vs Oxygen concentration

Previously, three studies compared the Holocene I/Ca in planktic foraminifera with  $\text{O}_2$  concentration in the water column (Lu et al., 2020; Lu et al., 2016; Winkelbauer, 2022). Here, we have added our northern Indian Ocean data to these previously recorded databases. The I/Ca ratios in planktic foraminifera from the core-tops varied from 0.03 to  $9 \mu\text{mol mol}^{-1}$  (**Figure 3.3**). I/Ca values span the minimum dissolved  $\text{O}_2$  concentration range of nearly 0 to  $270 \mu\text{mol kg}^{-1}$ . A significant correlation ( $r^2 = 0.75$ ,  $p < 0.05$ ) is found between I/Ca and minimum  $\text{O}_2$  concentrations. The uncertainty between I/Ca vs dissolved  $\text{O}_2$  is 0.01 for the intercept 0.12 and 0.00 for the slope 0.04 of the linear regression.

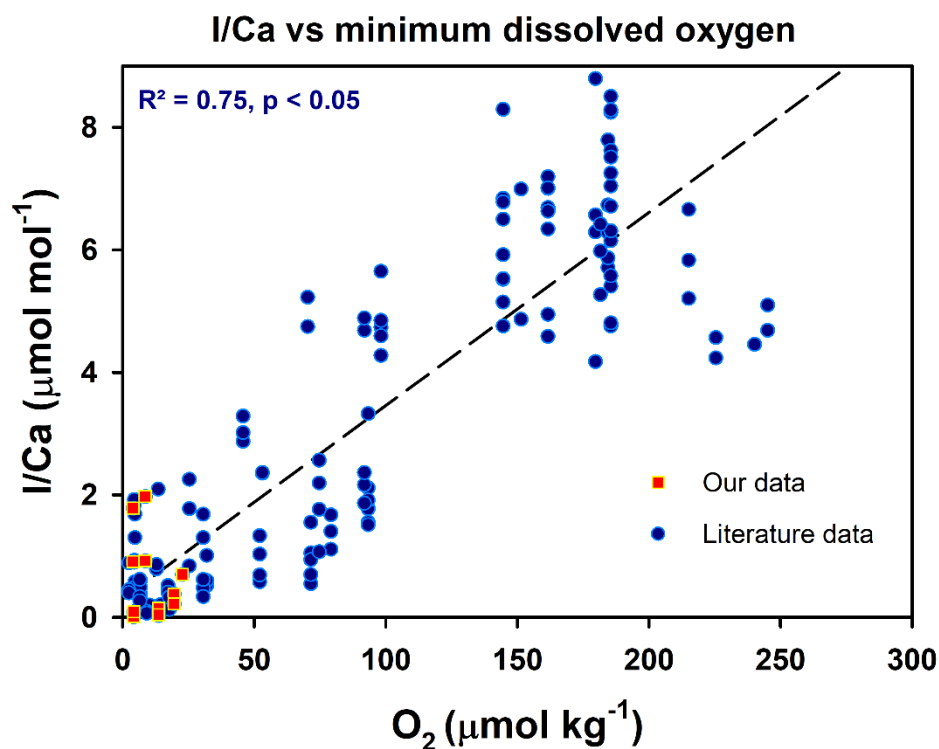


**Figure 3.3:** Correlation plot of I/Ca vs minimum oxygen concentration in the water column. The dissolved oxygen data is from World Ocean Atlas 2018. Red squares represent I/Ca data acquired in this study. Blue circles are literature data (Lu et al., 2020; Lu et al., 2016; Winkelbauer, 2022)

### 3.4 Discussion

As expected for the OMZ waters, our plankton tow I/Ca ratios from the northern Indian Ocean are extremely low, similar to those reported previously from the Eastern North Pacific OMZ (Winkelbauer et al., 2023). The relatively higher I/Ca ratios are from the southern Arabian Sea and the Andaman Sea, which are away from the highly deoxygenated central-eastern Arabian Sea. Although, we have not attempted to correlate our plankton tow I/Ca with dissolved  $\text{O}_2$  concentration due to the very narrow range of dissolved  $\text{O}_2$  concentration in the northern Indian Ocean along with the near detection limit of I/Ca values. Still, we can qualitatively infer from our observations that low I/Ca ratios reflect the presence of deoxygenated waters.

Similar to our plankton tow I/Ca ratios, the core-top I/Ca ratios are comparable to those reported from other OMZs (Lu et al., 2016; Winkelbauer et al., 2023). Relatively higher I/Ca are from the locations (SK-373/GC-02, SK-374/SP-04, and SK-374/SP-05) having depths >

2700 m, indicating that these samples are probably of relatively older age and having different dissolved O<sub>2</sub> concentrations. Moreover, relatively lower I/Ca ratios of the mixed foraminifera (having a population of relatively deeper living species) compared to *Trilobatus sacculifer*, are indicative of their depth habitat with deeper depths having less IO<sub>3</sub><sup>-</sup> concentration (Lu et al., 2016; Winkelbauer et al., 2023).

Winkelbauer et al. (2023) suggested that lower plankton tow I/Ca ratios compared to core-top I/Ca ratios are due to iodine gained post-mortem. This iodine could be of abiotic origin incorporated during sinking through the water column or after burial in the sediments (Winkelbauer et al., 2023). However, comparing plankton tow I/Ca with core-top planktic foraminifera I/Ca may not reflect the same population, as core-top sample deposition takes around hundreds to thousands of years. The short-term variability is averaged out in the core-top samples, and these changes could be significant as the average life span of planktic foraminifera is around 2 - 4 weeks. Meanwhile, the plankton tow foraminifera provides only a glimpse into a shorter time frame (a few days) compared to the entire lifespan of typical species, potentially missing the reproductive events. Our data further corroborates this observation, showing a greater difference between plankton tow I/Ca and core-top I/Ca in regions exceeding a depth of 2700 m (**Figure 3.4**). Additionally, Plankton-tow samples may also miss the gametogenic calcite which is formed by foraminifera at later stages of their life cycle (Schiebel & Hemleben, 2017). Winkelbauer et al. (2023)'s suggestion of iodine incorporation on the seafloor seems unlikely. Because if planktic I/Ca signal was from the seafloor, it should be similar to the benthic foraminifera I/Ca signal and other bottom water proxies ( $\Delta\delta^{13}\text{C}$  and aU), but this is not actually observed in data of ODP site 1242 (Eastern Equatorial Pacific) (Hoogakker et al., 2018; Lu et al., 2020). These pieces of evidence suggest that the planktic foraminifera are probably not gaining iodine post-mortem; instead, it is due to the different ages of samples pooled in core-top and plankton tows.

Our new core-top I/Ca data aligns with the previously reported I/Ca ratios in OMZ (Lu et al., 2016; Winkelbauer, 2022), indicating the reliability of our findings. Moreover, despite inherent uncertainties in the I/Ca proxy, the notable correlation observed between core-top I/Ca and minimum O<sub>2</sub> concentration reflects, in qualitative terms, the dissolved O<sub>2</sub> levels in subsurface waters, given that the minimum O<sub>2</sub> concentration typically occurs at intermediate ocean depths. The inclusion of new I/Ca measurements from intermediate OMZs could enhance our understanding of the association between core-top planktic I/Ca and seawater O<sub>2</sub> concentrations, providing a more comprehensive picture.

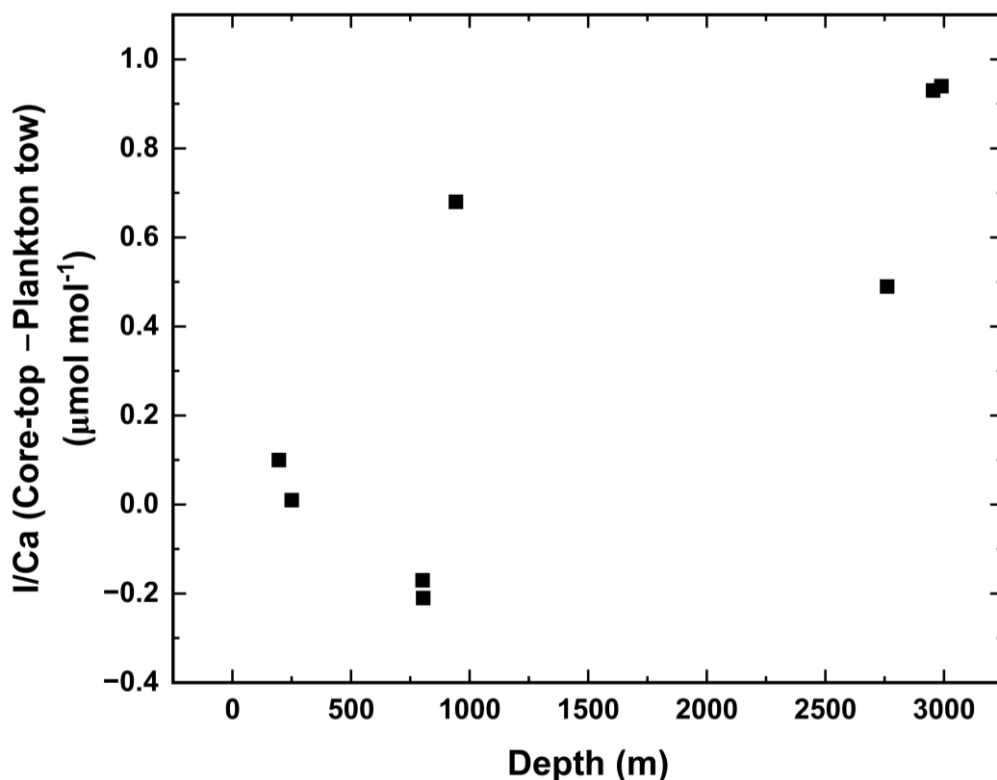


**Figure 3.4:** Plot of offset of I/Ca ( $\mu\text{mol mol}^{-1}$ ) ratios between core-top and plankton tow foraminifera with depth.

### 3.5 Conclusion

In this chapter, we have presented I/Ca ratios from plankton tow-derived and core-top planktic foraminifera from the northern Indian Ocean. We have observed low I/Ca ratios from plankton tow foraminifera, especially from the Arabian Sea OMZ, similar to Eastern North Pacific OMZ. Additionally, our core-top planktic foraminifera I/Ca ratios are low, agreeing with previous suggestions that low I/Ca ratios are indicative of low dissolved  $\text{O}_2$  waters. Lower I/Ca ratios found in mixed populations (having dominance of foraminifera tests from deeper depths) suggest that deeper foraminifera capture I/Ca signals from relatively deeper depths, probably having lower  $\text{IO}_3^-$  concentrations than the surface species. Moreover, the higher I/Ca ratios of core-top planktic foraminifera when compared to plankton tow foraminifera are probably due to the older age of the samples in the core-top compared to the plankton tow. Furthermore, the covariance observed between core-top I/Ca and minimum  $\text{O}_2$  concentrations reflects that the planktic foraminifera I/Ca is indicative of the dissolved  $\text{O}_2$  concentration in the intermediate depths.



# Chapter 4

## Glacial – interglacial subsurface oxygen variability in the Arabian Sea

### 4.1 Introduction

Oxygen (O<sub>2</sub>) is vital to all lives as it helps living organisms grow, reproduce, and turn food into energy. In the geological timescales, the ocean has played a great role in the oxygenation of the earth's atmosphere (Holland, 2006). The vertical distribution of O<sub>2</sub> in the ocean depends upon various biogeochemical processes operating at different depths (Shepherd et al., 2017). In the sunlit layer (~100 m), O<sub>2</sub> concentration is controlled by the O<sub>2</sub> produced through photosynthesis and air-sea gas exchange, which solubility is primarily influenced by temperature. O<sub>2</sub> concentrations in the intermediate layers (~100 –1500 m) are controlled by the respiration of organic matter and ventilation. In the deep ocean (>1500 m), dissolved O<sub>2</sub> concentrations are regulated by convective mixing of surface water masses in the higher latitudes and its subsequent ventilation in the low latitude regions. Additionally, the spatial distribution of O<sub>2</sub> is not uniform. The Atlantic Ocean is the most oxygenated, followed by the Pacific and the Indian Ocean (Schmidtko et al., 2017).

Over the past fifty years, there has been a drop in the ocean's O<sub>2</sub> content in both open and coastal seas due to increased anthropogenic disturbances that have resulted in a change in the pattern of marine productivity, biodiversity, and nutrient cycling (Breitburg et al., 2018). Maximum O<sub>2</sub> loss has been reported in the Equatorial Pacific, followed by the North Pacific. The Pacific Ocean contributes ~40% of the total O<sub>2</sub> loss, whereas the Indian Ocean is responsible for 8.5% of the global O<sub>2</sub> loss (Schmidtko et al., 2017). Lowering of O<sub>2</sub> concentration in the global ocean can reduce survival and growth, and may alter the behaviour of individual organisms, especially macrofauna thriving in O<sub>2</sub> depletion-prone environments (Breitburg, 2002; Breitburg et al., 2018; Rabalais et al., 2014).

With the ever-increasing human interventions, the management of ecosystems will depend on reliable future projections. By and large, the existing climate models agree well with the observations of O<sub>2</sub> loss from the ocean. However, these models disagree with the observed

extent of OMZs in the tropical ocean (Oschlies et al., 2018). This disagreement between models and observations challenges the reliability of future predictions, as these regions host large open ocean OMZs, where a further decrease in O<sub>2</sub> levels could adversely impact the marine ecosystem and biogeochemical pathways. In such a case, reconstructing the past O<sub>2</sub> levels in the geological past may provide insight into future deoxygenation. I/Ca in planktic foraminifera can be used to reconstruct past ocean O<sub>2</sub> levels (Lu et al., 2010).

I/Ca proxy relies on the covariation of iodine and oxygen in the ocean. Inorganic iodine exists in the ocean in two thermodynamically stable forms: iodate (IO<sub>3</sub><sup>-</sup>, oxidised form) and iodide (I<sup>-</sup>, reduced form). The standard reduction potential of IO<sub>3</sub><sup>-</sup>/I<sup>-</sup> is very close to that of O<sub>2</sub>/H<sub>2</sub>O, thus making it one of the first elements, along with Mn and N, to respond to changing O<sub>2</sub>. IO<sub>3</sub><sup>-</sup> is fully reduced to I<sup>-</sup> in anoxic waters and re-oxidised under well-oxygenated conditions (Rue et al., 1997). IO<sub>3</sub><sup>-</sup> is incorporated into the calcite structure (Lu et al., 2010) by substituting the CO<sub>3</sub><sup>2-</sup> ion in foraminifera. Thus, higher I/Ca values in foraminifera generally represent higher IO<sub>3</sub><sup>-</sup> concentrations in seawater, indicating oxygenated water conditions. Planktic foraminiferal I/Ca reflects upper ocean (0–500 m) O<sub>2</sub> levels (Lu et al., 2016; Zhou et al., 2014). On the basis of present-day core-top I/Ca vs [O<sub>2</sub>]<sub>min</sub> calibrations, I/Ca > 4 μmol mol<sup>-1</sup> values correspond to [O<sub>2</sub>] > 100 μmol kg<sup>-1</sup>, and I/Ca < 1.5 μmol mol<sup>-1</sup> values are indicative of regions with [O<sub>2</sub>] < μmol kg<sup>-1</sup> (Hardisty et al., 2021; Lu et al., 2016).

The Arabian Sea is one of the most intense perennial OMZ in the world ocean. This OMZ is formed due to poor ventilation and high overhead productivity, which leads to high respiration in the intermediate waters. While the monsoon-induced changes in surface hydrography control the productivity patterns across the Arabian Sea, the thermocline waters are affected by changes in global overturning circulations. Unlike other open-ocean hypoxic zones, the Arabian Sea is of particular interest, as it is developed in the relatively oligotrophic central-eastern part, away from the region of intense upwelling in the Oman-Somalia coast of the Arabian Sea (Banse et al., 2014; Rixen et al., 2020). There have been major changes in the OMZ intensity over decadal to millennial timescales in connection with global climate change (Reichart et al., 1998; Stramma et al., 2010). Nevertheless, the relative importance of atmospheric and deep-ocean circulations modulating the Arabian Sea OMZ through time and space is not well understood.

To assess the potential expansion and magnitude of the OMZ intensification, it is essential to study basin-wide changes in the OMZ in response to climate variability at different

time scales. For this purpose, we have generated two new records of I/Ca from the northern and the southeastern Arabian Sea to reconstruct the past dissolved O<sub>2</sub> levels in the basin and to decipher the processes controlling the OMZ variability.

## 4.2 Materials and Methods

We have collected two sediment cores from the Arabian Sea (**Figure 4.1**). The northern core lies in the core of the oxygen-deficient zone, and the southeastern core is located outside of the oxygen-deficient zone with a slightly different vertical profile of dissolved O<sub>2</sub> (**Figure 4.2**).

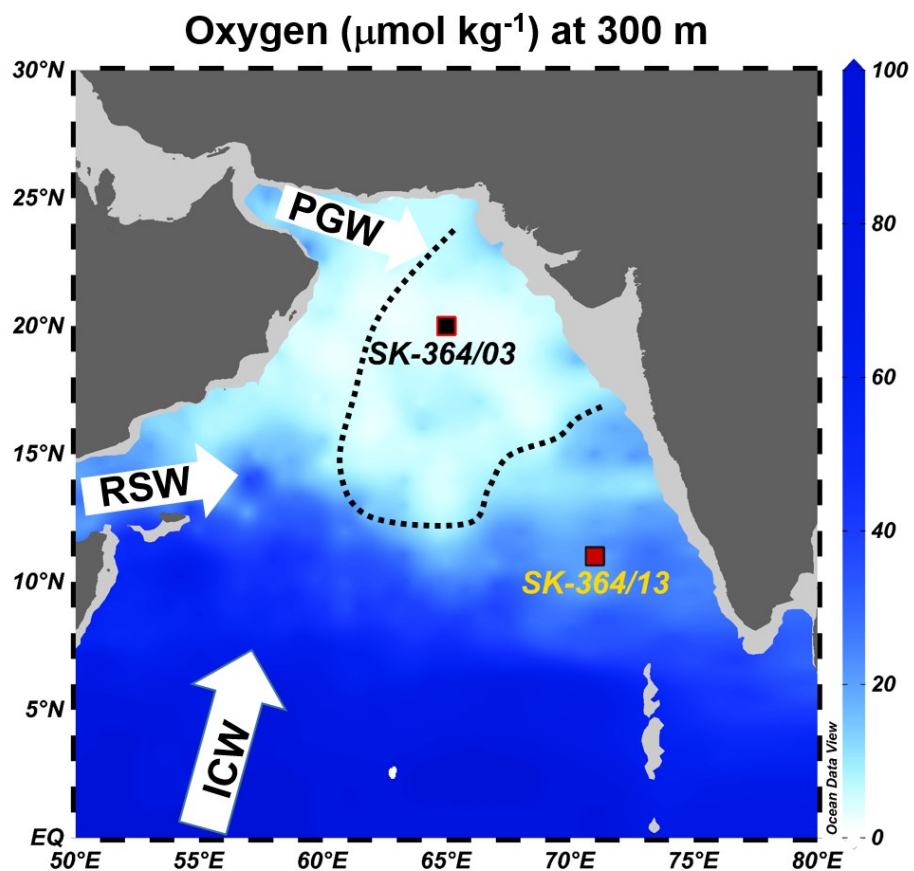


**Figure 4.1:** Map showing the core locations used in this study superimposed over the climatological dissolved oxygen (O<sub>2</sub>) concentration at 300 m depth. The Black curve shows the present-day oxygen-deficient zone in the Arabian Sea. Dissolved O<sub>2</sub> data taken from World Ocean Atlas 2018.

The Age models for both sediment cores were developed by radiocarbon dating of planktic foraminifera shells. We have measured I/Ca and Mg/Ca ratios in *Trilobatus sacculifer* along with total organic carbon in the bulk sediment. To convert Mg/Ca ratio of planktic foraminifera into temperature, a regional species-specific Mg/Ca vs temperature calibration

equation is required. But, no such regional calibration equation for the Arabian Sea exists. Given the fundamental limitations, an effort was made to choose the best possible calibration equation such that the core-top temperature is close to the present-day temperature. Hence, the Mg/Ca vs temperature calibration equation for *Trilobatus sacculifer* provided by Anand et al. (2003) was used. This calibration equation is as follows:

$$\text{Mg/Ca} = B \exp (AT),$$

Where,  $B = 0.347 (\pm 0.011)$ , and  $A = 0.090$  for *Trilobatus sacculifer*. By using this calibration equation, in the northern Arabian Sea, the core-top temperature is  $25.7^{\circ}\text{C}$ , with the present-day mixed layer temperature being  $26.1^{\circ}\text{C}$ . In the southeastern Arabian Sea, the core-top temperature is  $27.3^{\circ}\text{C}$ , with the present-day temperature being  $28.1^{\circ}\text{C}$ . The core-top temperature estimates using Mg/Ca ratio are within  $\sim \pm 1^{\circ}\text{C}$ , which is generally the accepted uncertainty in the temperatures obtained using Mg/Ca paleothermometry.

The Al/Ca, Fe/Ca, Mn/Ca ratios were also measured to trace the contaminations contributed by the clay/silicate fractions or during sample processing. However, the Al/Ca ratio was found to be less than  $100 \mu\text{mol mol}^{-1}$  in most samples (144 out of 164) and did not show any significant trend with Mg/Ca ratios, indicating that there was no clay or silicate contamination (Barker et al., 2003). Whereas, insignificant relations of Fe/Ca and Mn/Ca ratios with Mg/Ca ratio, suggesting an efficient cleaning of foraminiferal shells (Barker et al., 2003).

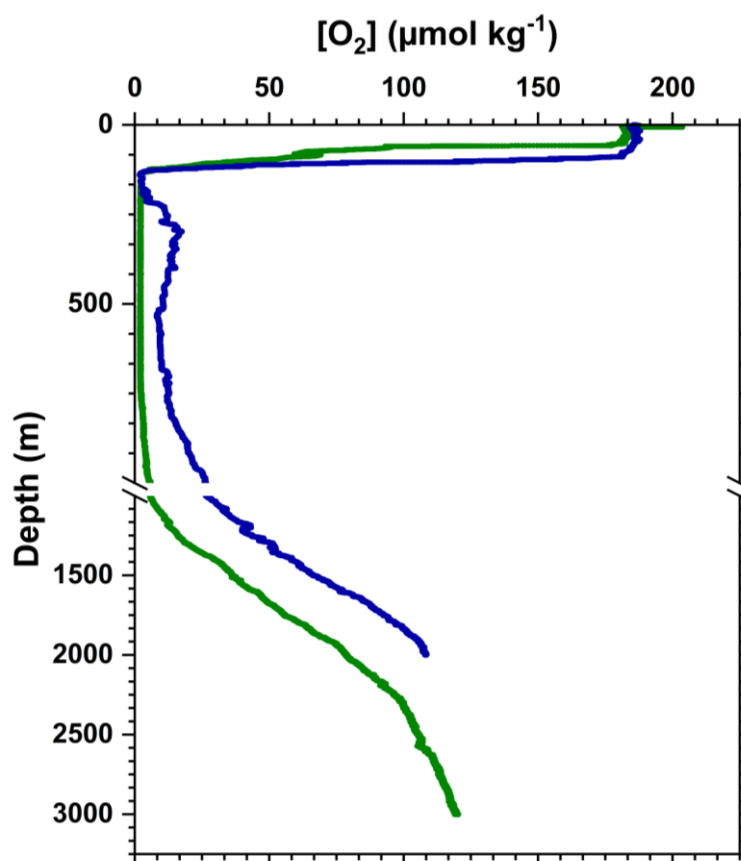


**Figure 4.2:** Vertical profile of dissolved  $O_2$  at the core locations. The dark green curve is for the northern Arabian Sea core (SK-364/03), and the dark blue curve represents dissolved  $O_2$  concentrations at the southeastern core location (SK-364/13). Please note the break in the y-axis.

## 4.3 Results

### 4.3.1 Chronology and Sedimentation Rate

A summary of the radiocarbon measurements of sediment cores SK-364/03 and SK-364/13 is given in **Table 4.1** and **Table 4.2**, respectively. The sediment core SK-364/03 covers the depositional history of the last  $\sim 37$  ka (**Figure 4.3** (a)) with an average sedimentation rate of  $5.52 \text{ cm ka}^{-1}$ . The sedimentation rate was highest from  $\sim 30.5$  to  $32$  ka BP and lowest from  $\sim 12$  to  $6.7$  ka BP (**Figure 4.4** (a)). The southeastern sediment core (SK-364/13) suggested an average sedimentation rate of  $3.29 \text{ cm ka}^{-1}$  with a depositional history of the last  $\sim 47$  ka (**Figure 4.3** (b)). The sedimentation remained almost similar throughout except for an excursion between  $\sim 40$  to  $\sim 42$  ka BP with a sedimentation rate of  $9.06 \text{ cm ka}^{-1}$  (**Figure 4.4** (b)).

**Table 4.1:** Radiocarbon age, calibrated age range, and median age of SK-364/03 sediment core.

S. No.	Lab ID	Mean depth (cm)	Species	Radiocarbon Age ( <sup>14</sup> C yr BP) (2σ)	Calendar Age Range (cal yr BP)	Median Age (cal yr BP)
1	AURIS-03619	10.5	<i>Globigerinoides ruber</i> and <i>Trilobatus sacculifer</i>	6413 ± 54	6459 - 7117	6772
2	AURIS-03620	21.5	<i>Globigerinoides ruber</i> and <i>Trilobatus sacculifer</i>	9915 ± 73	10345 - 11126	10717
3	AURIS-03621	31.5	<i>Globigerinoides ruber</i> and <i>Trilobatus sacculifer</i>	10991 ± 66	11854 - 12577	12233
4	AURIS-03622	41.5	<i>Globigerinoides ruber</i>	11938 ± 107	12994 - 13889	13349
5	AURIS-03623	61.5	<i>Globigerinoides ruber</i> and <i>Trilobatus sacculifer</i>	16451 ± 82	18477 - 19368	18952
6	AURIS-03624	80.5	<i>Globigerinoides ruber</i> and <i>Trilobatus sacculifer</i>	18856 ± 144	21390 - 22574	22001
7	AURIS-03625	103.5	<i>Globigerinoides ruber</i>	24632 ± 182	27364 - 28578	27949
8	AURIS-03626	120.5	<i>Globigerinoides ruber</i> and <i>Trilobatus sacculifer</i>	27532 ± 139	30192 - 31116	30752
9	AURIS-03627	140.5	<i>Globigerinoides ruber</i> and <i>Trilobatus sacculifer</i>	28791 ± 144	31747 - 33072	32310
10	AURIS-03628	160.5	<i>Globigerinoides ruber</i>	32117 ± 218	34854 - 36166	35603
11	AURIS-03629	180.5	<i>Globigerinoides ruber</i> and <i>Trilobatus sacculifer</i>	33554 ± 176	36905 - 38691	37523

**Table 4.2:** Radiocarbon age, calibrated age range, and median age of SK-364/13 sediment core.

S.No	Lab ID	Mean depth (cm)	Species	Radiocarbon Age ( $^{14}\text{C}$ yr BP) ( $2\sigma$ )	Calendar Age Range (cal yr BP)	Median Age (cal yr BP)
1	AURIS-03642	11.5	<i>Globigerinoides ruber</i>	6349 ± 64	6344 - 7123	6709
2	AURIS-03644	20.5	<i>Globigerinoides ruber</i>	8853 ± 62	8796 - 9939	9433
3	AURIS-03643	30.5	<i>Globigerinoides ruber</i>	11722 ± 73	12566 - 13677	13148
4	AURIS-03646	61.5	<i>Globigerinoides ruber</i> and <i>Trilobatus sacculifer</i>	20810 ± 85	22865 - 24365	24170
5	AURIS-03647	80.5	<i>Globigerinoides ruber</i>	29604 ± 131	32326 - 34111	33364
6	AURIS-03648	102.5	<i>Trilobatus sacculifer</i>	36121 ± 193	39446 - 40827	40146
7	AURIS-03649	121.5	<i>Globigerinoides ruber</i>	38950 ± 239	41850 - 42836	42244
8	AURIS-03650	140.5	<i>Trilobatus sacculifer</i>	44172 ± 411	44836 - 47074	45803

#### 4.3.2 Foraminiferal I/Ca variations

In the northern Arabian Sea (SK-364/03), I/Ca measured on *Trilobatus sacculifer* varied from 0.17 to 1.86  $\mu\text{mol mol}^{-1}$ . I/Ca remained mostly low ( $<1.5 \mu\text{mol mol}^{-1}$ ) but increased during MIS 1 around Younger Dryas (YD; 12 ka BP). I/Ca values remained almost unchanged from 37 ka to 19 ka BP (Figure 4.5 (a)).

In the southeastern Arabian Sea (SK-364/13), in most time periods, I/Ca values were higher than those observed over the northeastern Arabian Sea. I/Ca varied from 0.39 to 5.00  $\mu\text{mol mol}^{-1}$  in the southern region. Like in the northern location, I/Ca values were higher during MIS 1 around YD. I/Ca values remained below 1.5  $\mu\text{mol mol}^{-1}$  from ~47 ka BP till LGM except at the end of MIS 3. At the end of LGM, the I/Ca value increases until YD and decreases thereafter. I/Ca remained  $>4 \mu\text{mol mol}^{-1}$  from ~15 to ~8 ka BP. Although I/Ca values were higher in the north than in the south, both regions show similar trends with higher values after LGM. But the difference in I/Ca values in the north and south was large after deglaciation.

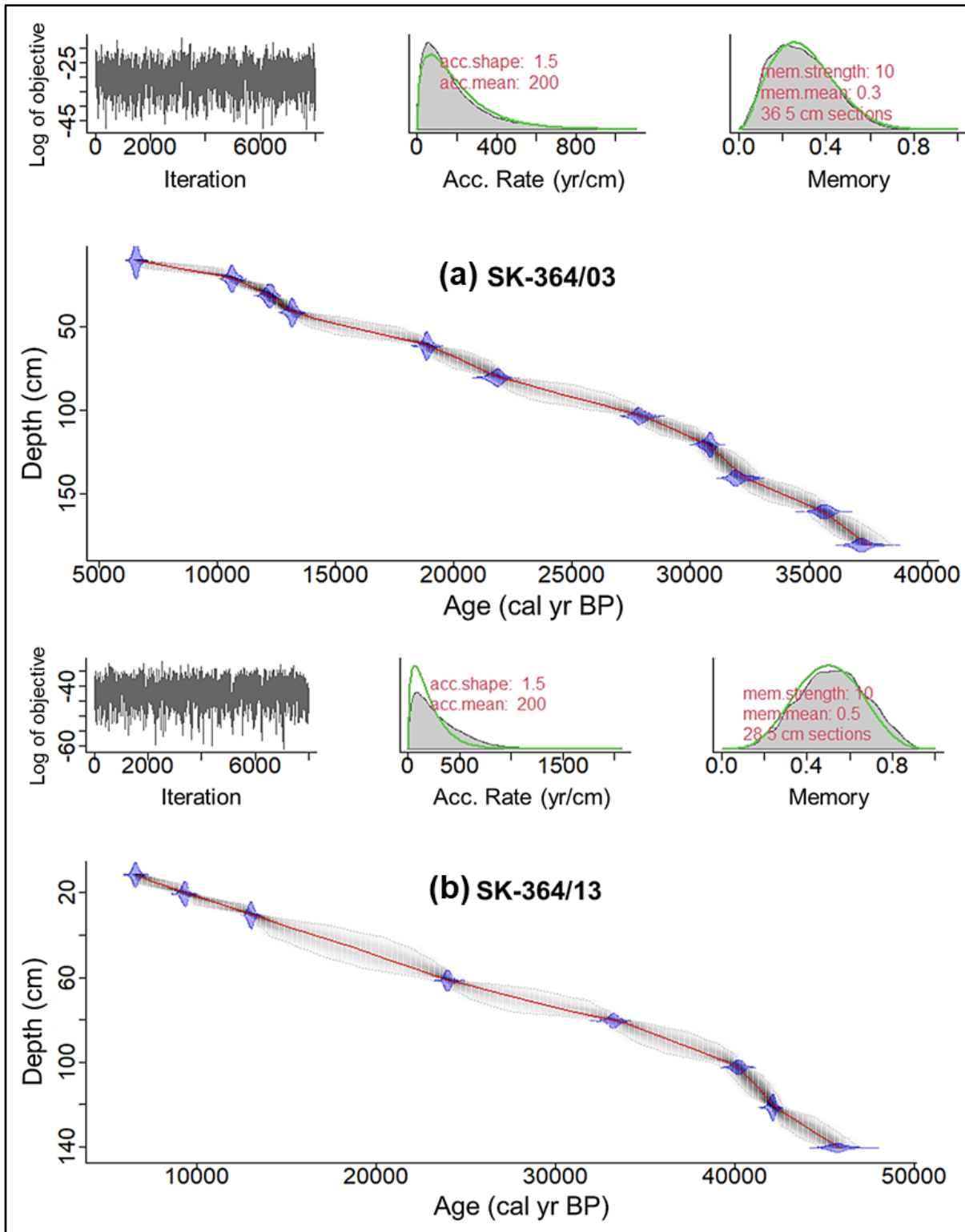


**Figure 4.3:** Age-depth model of (a) SK-364/03, and (b) SK-364/13. The upper panels show Markov Chain Monte – Carlo iteration history (left), prior (green lines), posterior (grey histograms), density functions for accumulation rate (middle), and memory (right). The lower panel shows the age-depth model with calibrated  $^{14}\text{C}$  dates in blue. The red line shows the modelled mean age at 95 % confidence interval (grey dotted lines).

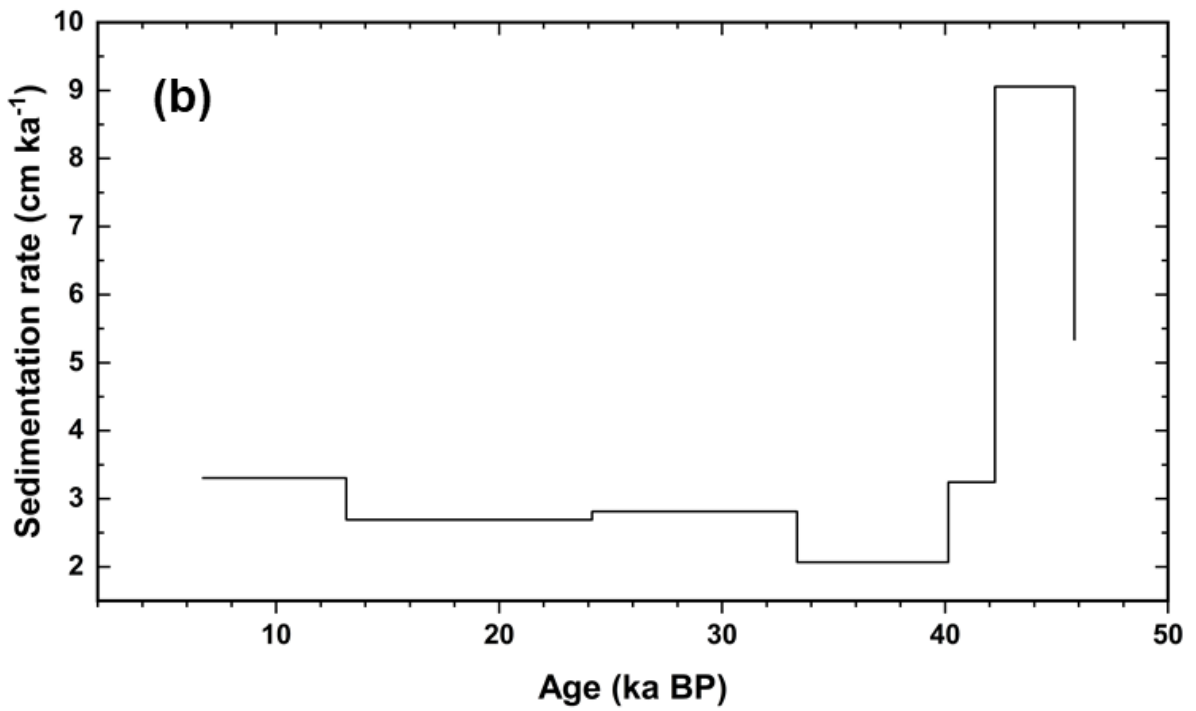
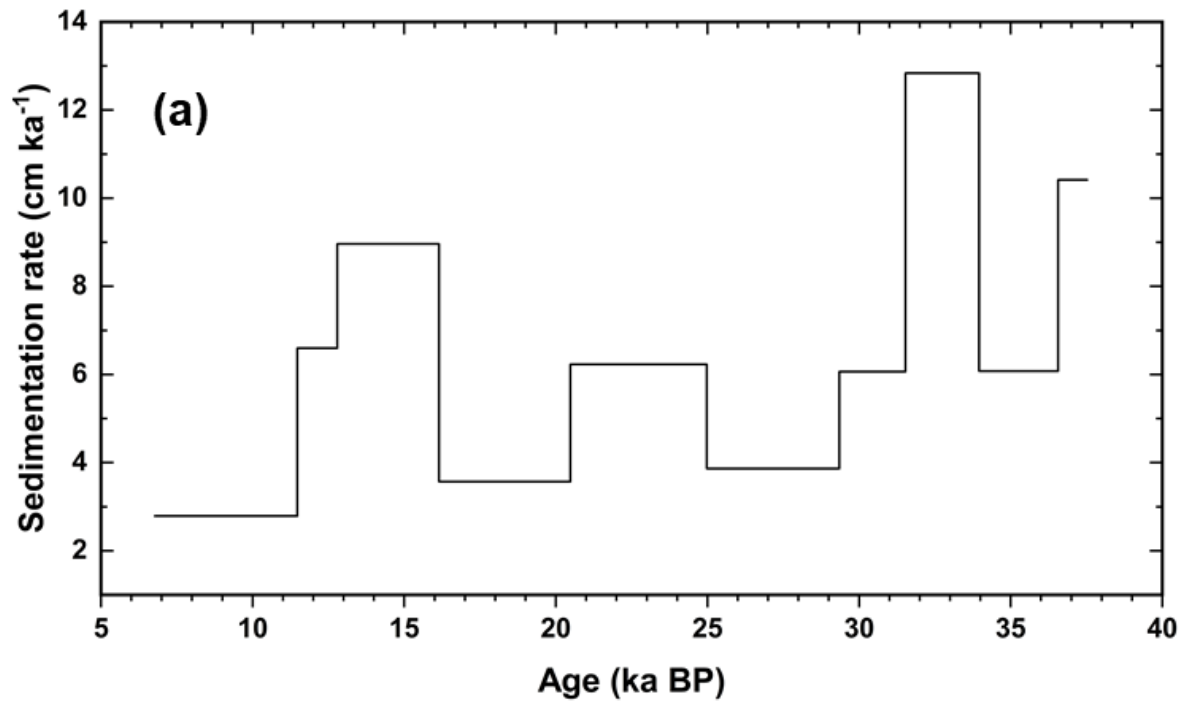


**Figure 4.4:** Sedimentation rate estimated using the data obtained from (a) SK-364/03, and (b) SK-364/13.

### 4.3.3 Temperature reconstruction

In the northern Arabian Sea, Mg/Ca-derived temperatures varied from 23.02 to 26.09 °C. The lowest temperatures are observed in MIS 2 during LGM. Temperature increased after the LGM to MIS 1. In the southeastern location, temperature varied from 24.26 to 27.43°C. The temperature in the MIS 3 did not vary much. Temperature started increasing in LGM to MIS 1. Temperature trends were similar at both locations, but the southeastern region was warmer than the northeastern except at the start of MIS 2, where both regions witnessed similar temperatures (**Figure 4.5 (b)**).

### 4.3.4 Total organic carbon (TOC) variations

TOC varied from 0.38 to 2.16 % in the northern Arabian Sea. The TOC was unusually high, around 37 ka BP. Barring this, TOC values were higher during the LGM compared to the deglaciation, with YD having the lowest TOC content. TOC content increased from 35 ka BP to LGM and then decreased during deglaciation, followed by a rise again in the Holocene after YD.

In the southeastern region, TOC varied between 0.41 and 0.94 %. TOC content was highest during LGM and lowest during the deglaciation. After LGM, the TOC content decreased in the deglaciation and increased in MIS 1. Both the locations showed similar trends (except at 37 ka) with higher TOC content during LGM (**Figure 4.5 (c)**).

## 4.4 Discussions

### 4.4.1 Oxygen variability during the glacial period

Based on current I/Ca vs  $[O_2]_{\min}$  core-top calibrations (Hardisty et al., 2021; Lu et al., 2020; Zhou et al., 2022), our I/Ca record suggests that both the northern and southeastern Arabian Sea persistently remained deoxygenated, with dissolved  $O_2$  concentrations  $< 7 \mu\text{mol kg}^{-1}$ .  $O_2$  concentration in the ocean depends upon three main factors: 1) temperature-related dissolved  $O_2$  solubility, 2) biological productivity-related  $O_2$  consumption in the intermediate depths, and 3) ventilation through ocean circulation. The direct effect of cooler temperatures would have been to increase oxygenation in the glacial northern Arabian Sea owing to increased  $O_2$  solubility (Garcia & Gordon, 1992). However, our I/Ca record suggests deoxygenated waters during glacial times in the northern Arabian Sea, indicating that the role of cooler temperatures was overshadowed for this deoxygenation. Thus, the changes in biological productivity and ventilation through ocean circulation might explain the

deoxygenation observed during the last glacial period. Two mechanisms that could reduce O<sub>2</sub> concentrations during colder climates: (1) decreased ventilation from higher latitude water masses and/or (2) increased biological primary productivity, which can be attributed to enhanced winter monsoon convective mixing in the Arabian Sea, especially in the northern Arabian Sea.

Previous records indeed suggest a stronger winter monsoon during the LGM (Sarkar et al., 1990). This might have led to higher primary productivity in the northern Arabian Sea (Zhou et al., 2022). Naik et al. (2017) utilized *G. bulloides* abundance, % CaCO<sub>3</sub>, and % TOC from various cores from the southeastern Arabian Sea and suggested higher primary productivity in the region. To the same effect, our TOC content also shows higher values during the LGM. Although % TOC is a function of both surface primary productivity and preservation conditions (Calvert et al., 1995; Canfield, 1994), high primary productivity coupled with deoxygenated conditions during the glacial might have resulted in better preservation of organic carbon in the sediments. High primary productivity has also been reported in the eastern Arabian Sea during the last glacial period using different cores in this region (Kumar et al., 2005; Banakar et al., 2005). High primary productivity has been attributed to enhanced winter monsoon during the glacial period. During glacial times, the temperature gradient between the central Asian landmasses and the ocean increased, leading to enhanced dry northeasterly winds in the Arabian Sea. These winds lead to enhanced evaporation in the Arabian Sea, resulting in cold, denser surface waters, which give rise to intense convective mixing in the region. Intensified winter convective mixing entrains subsurface nutrients to the surface, fuelling primary productivity in the region, which in turn might be responsible for the intense subsurface O<sub>2</sub> consumption by microbial respiration. Presently, winter convective mixing is effective above 15°N (Kumar & Prasad, 1996; Madhupratap et al., 1996). However, it is possible that winter convective mixing would have been effective even in the southeastern region during the glacial period due to increased thermal gradient. Additionally, the reduced influx of the low salinity Bay of Bengal water in the south-eastern region may have also contributed to reducing the stratification (Mahesh & Banakar, 2014). Moreover, the cold and dry conditions during the last glacial period would have led to more Aeolian inputs from the adjoining regions to the Arabian Sea, providing bio-available nutrients to the surface layer, especially in the northern region (Zhou et al., 2022).

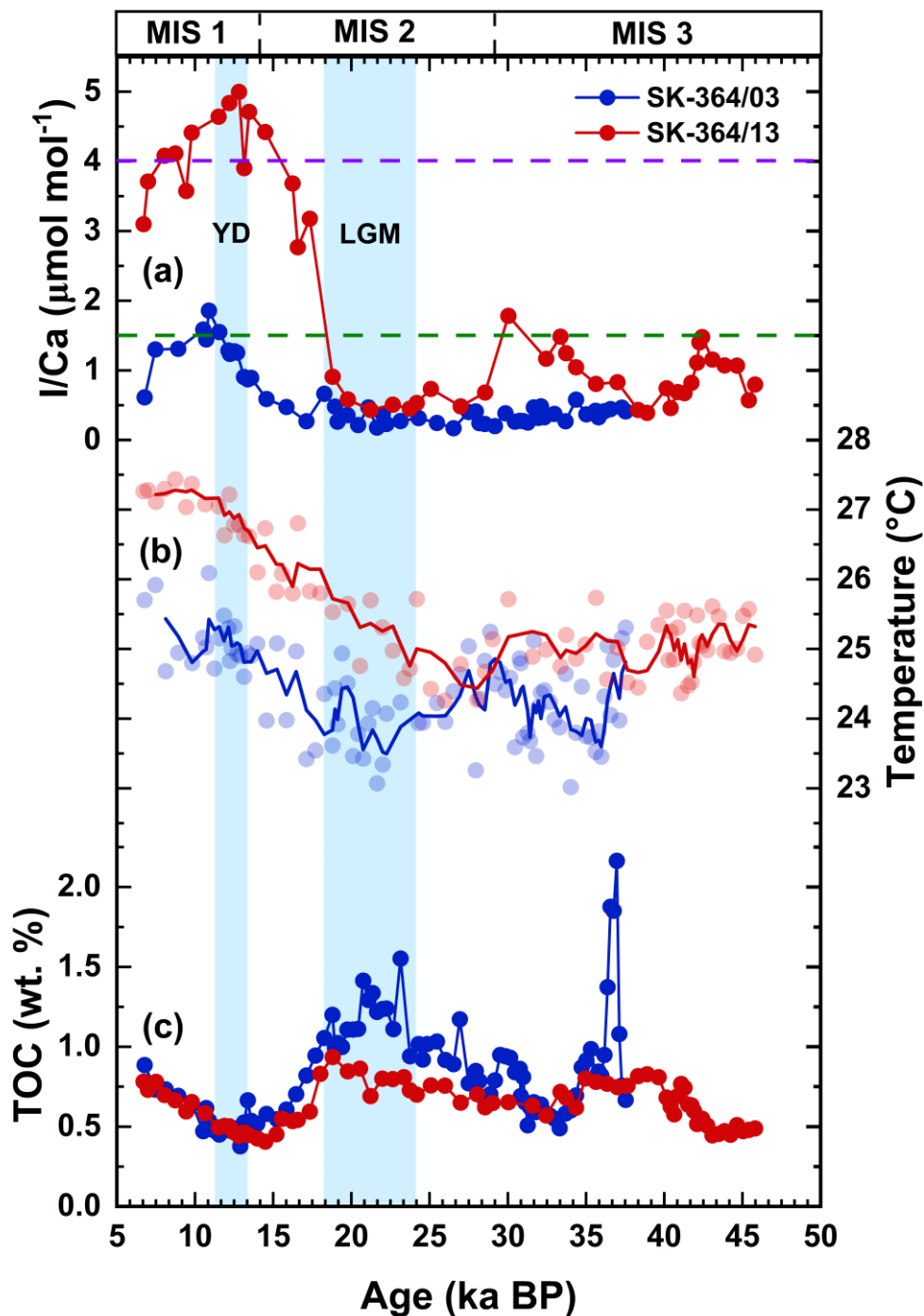


**Figure 4.5:** Temporal variations of (a) I/Ca measured in *Trilobatus sacculifer*; Violet and green dashed horizontal lines indicates I/Ca values corresponding to 100  $\mu\text{mol kg}^{-1}$  and 7  $\mu\text{mol kg}^{-1}$  dissolved  $\text{O}_2$  concentrations, respectively; (b) temperature reconstructed from Mg/Ca measurements in *Trilobatus sacculifer*; filled circles show the data point, and the superimposed curves show the three-point running average; and (c) total organic carbon (TOC) contents.

Model simulations suggest that during the last glacial period, the ventilation of the intermediate layers of the Arabian Sea was reduced due to its separation from the marginal seas due to reduced sea levels (the Red Sea and the Persian Gulf), which led to the intensification of deoxygenation (Lachkar et al., 2019). The contribution of the southern sourced intermediate water masses may have also decreased during the glacial period, as indicated by lower  $\delta^{13}\text{C}$  of benthic foraminifera (Naik & Naik, 2022). Thus, deoxygenated waters persisted in the studied region, with the interplay of enhanced winter convective mixing inducing high primary productivity and less ventilation in the intermediate waters.

#### 4.4.2 Oxygen variability during the deglaciation

Our I/Ca records indicate a sudden increase in the dissolved  $\text{O}_2$  concentrations in the basin after LGM. The dissolved  $\text{O}_2$  concentrations in the northern region increased above  $7 \mu\text{mol kg}^{-1}$  around YD. But, interestingly, the dissolved  $\text{O}_2$  concentration in the south-eastern Arabian Sea rose well above  $100 \mu\text{mol kg}^{-1}$  in the deglaciation, with YD time being the most oxygenated. Increasing temperatures during the deglaciation would result in a decrease in  $\text{O}_2$  concentration due to a decrease in temperature-related solubility of  $\text{O}_2$ . However, during the LGM, our records suggest that temperature-related  $\text{O}_2$  solubility must have been overshadowed by other dominant processes. So, similar to glacial times, we must turn to surface primary productivity changes and intermediate water ventilation changes.

Zhou et al. (2022), by using *Coccolithophore* assemblage, suggest lower primary productivity in the northern Arabian Sea. (Naik et al., 2017) utilized *G.bulloides* abundance, %  $\text{CaCO}_3$ , and % TOC from various cores from the south-eastern Arabian Sea, suggesting relatively lower primary productivity in the region. Our % TOC values also show a decreasing trend during the deglaciation. This decrease in primary productivity is in accordance with the decreasing strength of the winter monsoon. Weakened winter convective mixing entrains less subsurface nutrients to the surface, resulting in decreased primary productivity in the region, which in turn might be responsible for the reduced subsurface  $\text{O}_2$  consumption by microbial respiration. Additionally, the enhanced influx of the low-salinity Bay of Bengal water in the southeastern region may have also contributed to stratification (Mahesh & Banakar, 2014).

Enhanced ventilation of the intermediate water masses has been suggested previously during the deglaciation, especially during YD (Bryan et al., 2010; Ma et al., 2020; Yu et al., 2018). High  $\delta^{13}\text{C}$  of benthic foraminifera from the Arabian Sea reflects the northward

expansion of Antarctic Intermediate Water (AAIW) (Ma et al., 2019). This has also been supported by a study conducted on Cd/Ca of benthic foraminifera from the Arabian Sea (Ma et al., 2022). An enhanced influx of O<sub>2</sub>-rich AAIW northward in the Arabian Sea could increase thermocline dissolved O<sub>2</sub> concentration (Böning & Bard, 2009).

The interplay of reduced primary productivity with enhanced ventilation from the southern sourced intermediate waters led to better-oxygenated conditions during the deglaciation with most oxygenation during the YD. The difference in the dissolved O<sub>2</sub> concentrations from our records with the southeastern region showing more oxygenated conditions indicates that this region received more O<sub>2</sub> due to ventilation, and as the water masses moved northward, the O<sub>2</sub> was utilised in the intermediate depths.

#### **4.4.3 Oxygen variability during the early Holocene**

Our I/Ca records indicate a transition from better-oxygenated conditions during the early Holocene to deoxygenated conditions in both regions during the late Holocene, with the northern Arabian Sea becoming highly deoxygenated. The warmer temperatures leading to less O<sub>2</sub> solubility during the Holocene might have also affected this decreasing dissolved O<sub>2</sub> concentration. Moreover, the decreasing trend of I/Ca is in antiphase with TOC content, suggesting a major role in primary productivity.

The surface primary productivity in both the northern and the southeastern Arabian Sea has been reported to be low during the early Holocene (Naik et al., 2017; Zhou et al., 2022). In the northern region, weaker winter monsoon conditions leading to weaker surface cooling-driven mixing along with reduction of aeolian activity and, overall, lower nutrient inputs in the surface layers are the main reasons behind the lower primary productivity in the region in the late Holocene. On the other hand, the low productivity in the southeastern region has been attributed to enhanced freshwater influx due to a stronger summer monsoon (Naik et al., 2017).

Even though surface primary productivity in the basin was lower during the early Holocene, we observed an increasing TOC content trend. This may be explained by the reduction in the ventilation of intermediate layers, resulting in lower dissolved O<sub>2</sub> concentrations in the water column and better preservation of the organic carbon in the sediments. It has been suggested that due to the increase in the sea level, the contribution of the intermediate water masses from the marginal seas increased. This might have hindered the northward movement of the southern sourced intermediate waters, which led to the reduction in the dissolved O<sub>2</sub> concentrations in the region.

## 4.5 Conclusion

In this chapter, we have presented reconstruction of the dissolved O<sub>2</sub> concentrations in the Arabian Sea using I/Ca measurements in planktic foraminifera *Trilobatus sacculifer* from two sediment cores. I/Ca measurements are paired with Mg/Ca derived temperature reconstructions and the total organic carbon measurements in the bulk sediment samples.

Here, we have observed low O<sub>2</sub> conditions both in the northern Arabian Sea as well as in the southeastern Arabian Sea until the LGM. After LGM, O<sub>2</sub> concentrations in both regions gradually increases until YD, followed by a decreasing trend in the Holocene. The O<sub>2</sub> increase beyond LGM during deglaciation is higher in the southeastern Arabian Sea as compared to the northern region with values >100 μmol kg<sup>-1</sup> in the water column, suggesting a well-oxygenated water column during YD. The lower dissolved O<sub>2</sub> levels during the glacial are probably due to enhanced primary productivity owing to strengthened winter monsoon-driven convective mixing, and increased input of bioavailable nutrients from dust inputs. This high primary productivity is accompanied by the reduction of ventilation from the southern sourced waters. The increasing trend in deglaciation is due to the lower primary productivity coupled with intense ventilation of the intermediate waters from southern sources waters (e.g., AAIW). High dissolved O<sub>2</sub> concentrations during YD are possibly due to the reduced surface primary productivity accompanied with higher subsurface ventilation by the intermediate water masses from the adjacent Red Sea, Persian Gulf, and southern sourced water masses. During the early Holocene, the gradual decrease in the dissolved O<sub>2</sub> levels is best explained by the reduction of ventilation from the southern sourced water masses.



# Chapter 5

## Paleo-nitrogen cycling in the Arabian Sea

### 5.1 Introduction

Nitrogen is an essential element and considered to be one of the basic building blocks of all living organisms. Despite the abundant dissolved  $N_2$  gas in the ocean, its bioavailable forms (e.g.,  $NO_3^-$  and  $NH_4^+$ ) are limited for primary productivity in the sunlit ocean. This limitation imposes a significant nutrient scarcity in marine ecosystems. Despite occupying only ~4 % of the ocean's volume, oxygen deficient zones play an important role in the nitrogen cycle. Within these zones, the denitrification process leads to substantial losses of  $NO_3^-$ , leaving behind excess phosphorus in the surrounding waters. This excess phosphorus, upon entering the euphotic zone, stimulates nitrogen fixation, effectively influencing the availability of nitrogen for marine life (Deutsch et al., 2007; Gruber & Galloway, 2008). Denitrification enriches the residual nitrate pool with  $^{15}NO_3^-$  (Sigman et al., 2009), while  $N_2$  fixation introduces new bioavailable nitrogen characterized by low  $\delta^{15}N$  values (Capone et al., 1997), thus restoring nitrogen balance in the ocean.

The Arabian Sea is one of the most intense perennial OMZs in the world ocean. This OMZ is formed due to poor ventilation and high overhead productivity, which leads to high respiration in the intermediate waters (Kamykowski & Zentara, 1990; McCreary et al., 2013; Morrison et al., 1998). While the monsoon-induced changes in surface hydrography control the productivity patterns across the Arabian Sea, the thermocline waters are affected by global overturning circulations. The Arabian Sea accounts for at least one-third of the global loss of marine fixed nitrogen (Codispoti & Christensen, 1985). In addition, the nitrogen cycle influences the radiative properties of the atmosphere by generating a potent greenhouse gas,  $N_2O$  (Ravishankara et al., 2009) and by assisting the biological sequestration of  $CO_2$  in the ocean (Altabet et al., 2002; Falkowski, 1997; Ganeshram et al., 1995).

Human activities are altering the nitrogen cycle by increasing terrestrial  $N_2$  fixation rates through the Haber-Bosch process and introducing bioavailable nitrogen to the ocean surface through rivers and the atmosphere (Gruber & Galloway, 2008). Additionally, present-

day warming is projected to accelerate denitrification rates by expanding OMZ in the water column (Gruber & Galloway, 2008) and altering nitrate supply routes through changes in ocean circulation (Schmittner et al., 2008). However, the observational history of oceanic  $\text{NO}_3^-$  concentrations is relatively short compared to the residence time of bioavailable nitrogen, hindering the detection of climatic trends (Deutsch et al., 2011). In contrast, the geological records provide a detailed account of climate fluctuations like glacial-interglacial cycles. The nitrogen stable isotope ratios ( $\delta^{15}\text{N}$ ) of sinking organic matter preserved in sediments can provide insights into the changes in the paleo nitrogen cycle (Altabet et al., 1995; R. S. Robinson et al., 2012). The  $\delta^{15}\text{N}$  of sedimentary organic matter serves as an indicator of biological processes in the water column, such as denitrification (Altabet et al., 1995; Ganeshram et al., 1995) and nitrogen fixation (Haug et al., 1998).

Previous sediment records of  $\delta^{15}\text{N}$  in the Arabian Sea suggest that the monsoon-driven surface productivity and associated  $\text{O}_2$  consumption were the main drivers of the variation in water column denitrification in the past (Altabet et al., 1995, 2002). Additionally, the  $\text{O}_2$  supplied to intermediate waters by AAIW may have regulated the denitrification rates in the northern Arabian Sea (Pichevin et al., 2007). Notably, all these records are from the continental margins that could have been compromised by terrestrial inputs. Moreover, the  $\delta^{15}\text{N}$  of sedimentary organic matter has been interpreted to reflect only denitrification, reducing the influence of other lessening the role of other biological processes, mainly  $\text{N}_2$  fixation, influencing the nitrogen isotopic composition of the sinking organic matter. It has been suggested that a balance is needed between nitrogen inputs (primarily  $\text{N}_2$  fixation), and losses (mainly denitrification) on the timescale of the residence time of bioavailable nitrogen in the ocean. Therefore, changes in denitrification should be linked to and thus signify changes in  $\text{N}_2$  fixation (Gruber & Galloway, 2008)

In this study, we aimed to investigate the paleo nitrogen cycle by analysing the  $\delta^{15}\text{N}$  of bulk sediment samples collected from the northern and southeastern Arabian Sea. Additionally, we explored the potential correlation between nitrogen fixation and denitrification over both space and time. We examined how fluctuations in dissolved  $\text{O}_2$  levels influence various nitrogen cycle processes. Moreover, we cross-referenced our  $\delta^{15}\text{N}$  findings with those from previous research work to construct a comprehensive understanding of the paleo nitrogen cycle in the basin.

## 5.2 Material and Methods

We have measured the % TOC and its isotopic composition ( $\delta^{13}\text{C}_{\text{org}}$ ) on decarbonated sediments in the two sediment cores that are discussed in Chapter 4. Sedimentary organic matter, when acidified to remove carbonates, results in bias in nitrogen content and its isotopic composition (Brodie et al., 2011). To avoid this issue with acidified sediments, we measured TN and its isotopic composition ( $\delta^{15}\text{N}$ ) on the untreated bulk sediments. A detailed description of the carbon, nitrogen and isotopic measurements is provided in Chapter 2.

## 5.3 Results

### 5.3.1 Variations in $\delta^{13}\text{C}_{\text{org}}$ , and TOC (wt. %)

$\delta^{13}\text{C}_{\text{org}}$  varied from -21.64 to -19.53 ‰ in the northern Arabian Sea. The  $\delta^{13}\text{C}_{\text{org}}$  values were higher ( $> -20$  ‰) during early Holocene, LGM and around 37 ka BP, while the lowest  $\delta^{13}\text{C}_{\text{org}}$  were observed during YD. The  $\delta^{13}\text{C}$  increased from 35 ka BP to LGM and then decreased during the deglaciation, followed by a rise in the Holocene after YD (**Figure 5.1**). In the southeastern region,  $\delta^{13}\text{C}_{\text{org}}$  varied between -21.03 to -18.20 ‰ (**Figure 5.2**). The  $\delta^{13}\text{C}_{\text{org}}$  was highest around 25 ka BP and lowest during the early Holocene. After LGM, there was a continuous decrease in  $\delta^{13}\text{C}_{\text{org}}$ . Both locations showed a similar decreasing trend after LGM (**Figure 5.1** and **Figure 5.2**). The % TOC variation in both locations was discussed previously in Chapter 4 (section 4.3.4).

### 5.3.2 Variations in $\delta^{15}\text{N}$ , and TN (wt %)

$\delta^{15}\text{N}$  varied between 6.41 to 9.79 ‰ in the northern Arabian Sea (**Figure 5.1**). The highest  $\delta^{15}\text{N}$  was observed during the early Holocene. The  $\delta^{15}\text{N}$  was unusually high, around 37 ka BP. In addition, the  $\delta^{15}\text{N}$  values were higher during the LGM compared to the deglaciation. Similar to deglaciation, lower values were observed around 30 ka BP. The  $\delta^{15}\text{N}$  values increased from 27 ka BP to LGM, then decreased in the deglaciation, followed by a rise after YD in the early Holocene (**Figure 5.1**). In the southeastern region,  $\delta^{15}\text{N}$  varied between 6.39 to 8.69 ‰ (**Figure 5.2**). High  $\delta^{15}\text{N}$  values were observed around 40 ka BP during the early Holocene – consistent with the observations in the northern region. The low  $\delta^{15}\text{N}$  values were observed during the LGM and YD. After 40 ka BP,  $\delta^{15}\text{N}$  values gradually decreased until 20 ka BP in the LGM and then increased until 15 ka BP in the deglaciation. The  $\delta^{15}\text{N}$  again decreased until YD, followed by a rise in the Holocene. Although both the locations exhibited

similar  $\delta^{15}\text{N}$  trends, the  $\delta^{15}\text{N}$  values in the northern region were consistently higher than those in the southeast during the corresponding periods (**Figure 5.5 (a)**).

TN varied from 0.04 to 0.13 % in the northern Arabian Sea. In addition to the highest values around 37 ka BP, high TN content was observed during the LGM compared to the deglaciation. After 35 ka BP, the TN content increased from 35 ka BP to LGM and then decreased during the deglaciation, followed by a slight rise in the Holocene after YD. In the southeastern region, TN values varied between 0.03 to 0.06 %. TN content was highest during LGM and lowest during the deglaciation. After LGM, the TN content decreased in the deglaciation and increased minimally in the early Holocene. Both the locations showed similar trends (except at 37 ka) with higher TN content during LGM.

## 5.4 Discussion

### 5.4.1 No Influence of Terrestrial Organic Input and Diagenetic Changes on $\delta^{15}\text{N}$

Before using  $\delta^{15}\text{N}$  to reconstruct the past nitrogen cycle, it is essential to determine the origin of the sedimentary organic matter.  $\delta^{13}\text{C}_{\text{org}}$  helps to ascertain the source of the sedimentary organic matter. The average  $\delta^{13}\text{C}_{\text{org}}$  value of sedimentary organic matter of marine origin is -20‰ (Meyers, 1994). However, the terrestrial organic matter produced through the C3 and C4 pathways has a  $\delta^{13}\text{C}_{\text{org}}$  value of -27‰ and -14‰, respectively (Meyers, 1994). In the present study,  $\delta^{13}\text{C}_{\text{org}}$  has an average value of  $-20.3 \pm 0.48$ ‰ in the northern Arabian Sea and  $-19.1 \pm 0.62$ ‰ in the southeastern Arabian Sea.  $\delta^{13}\text{C}_{\text{org}}$  values in both locations imply that the sedimentary organic matter is of marine origin. Due to the considerable distance of the sampling locations from the coast, terrestrial inputs were *a priori* unexpected.

We examined the influence of any early diagenetic changes on the  $\delta^{15}\text{N}$  values through relationships among  $\delta^{15}\text{N}$ , % TOC and % TN. Early diagenetic degradation will increase  $\delta^{15}\text{N}$  values with a rise in % TOC and % TN, resulting in an anti-covariance trend (Agnihotri et al., 2003). However, we could not observe any such trends in this study. We do not find any correlation for the northern location between  $\delta^{15}\text{N}$  and % TN ( $r^2 = 0.004$ ,  $n = 92$ , **Figure 5.3 (a)**) and %TOC ( $r^2 = 0.05$ ,  $n = 92$ , **Figure 5.3 (b)**). Similarly, we do not find any correlation in the southeast between  $\delta^{15}\text{N}$  and % TN ( $r^2 = 0.007$ ,  $n = 73$ , **Figure 5.4 (a)**), and %TOC ( $r^2 = 0.12$ ,  $n = 73$ , **Figure 5.4 (b)**) either. This suggests that there is no significant influence of diagenesis on  $\delta^{15}\text{N}$ .

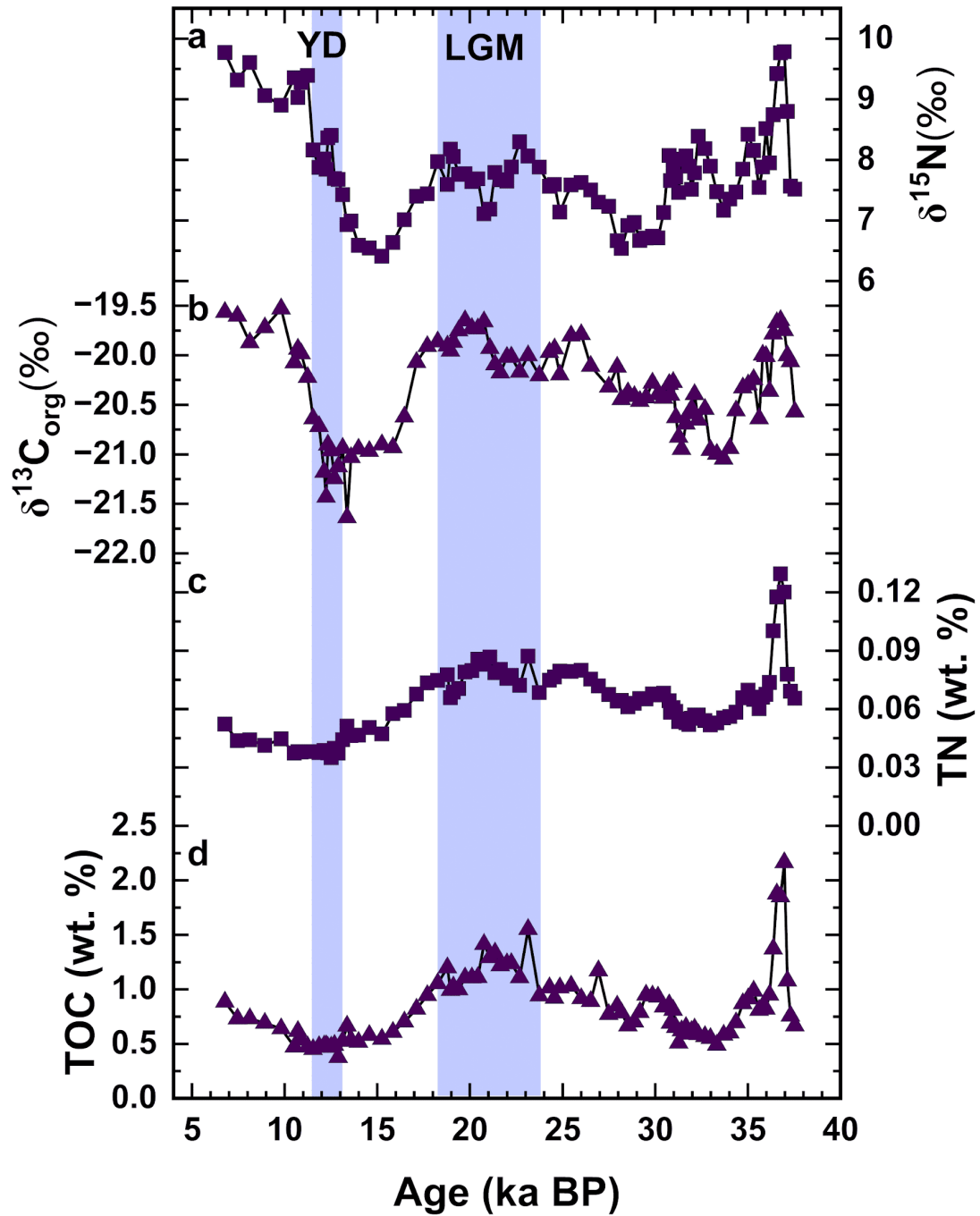


**Figure 5.1:** Temporal variations of (a)  $\delta^{15}\text{N}$  in the bulk sediments; (b)  $\delta^{13}\text{C}_{\text{org}}$  of the total organic carbon in the sediments; (c) total nitrogen (TN) content; and (d) total organic carbon (TOC) content in SK-364/03 (northern Arabian Sea).

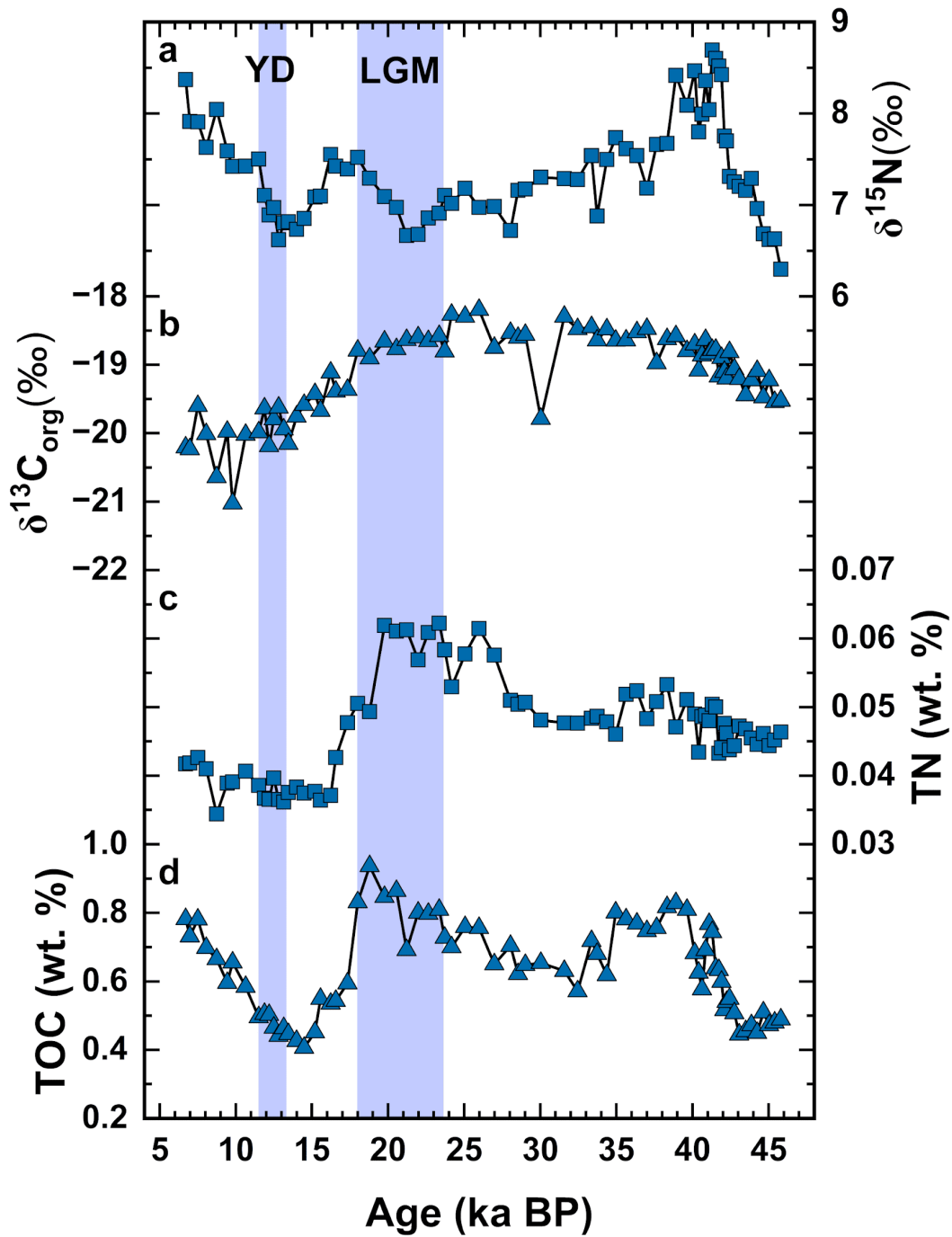


**Figure 5.2:** Temporal variations of (a)  $\delta^{15}\text{N}$  in the bulk sediments; (b)  $\delta^{13}\text{C}_{\text{org}}$  of the total organic carbon in the sediments; (c) total nitrogen (TN) content; and, (d) total organic carbon (TOC) contents in SK-364/13 (southeastern Arabian Sea).

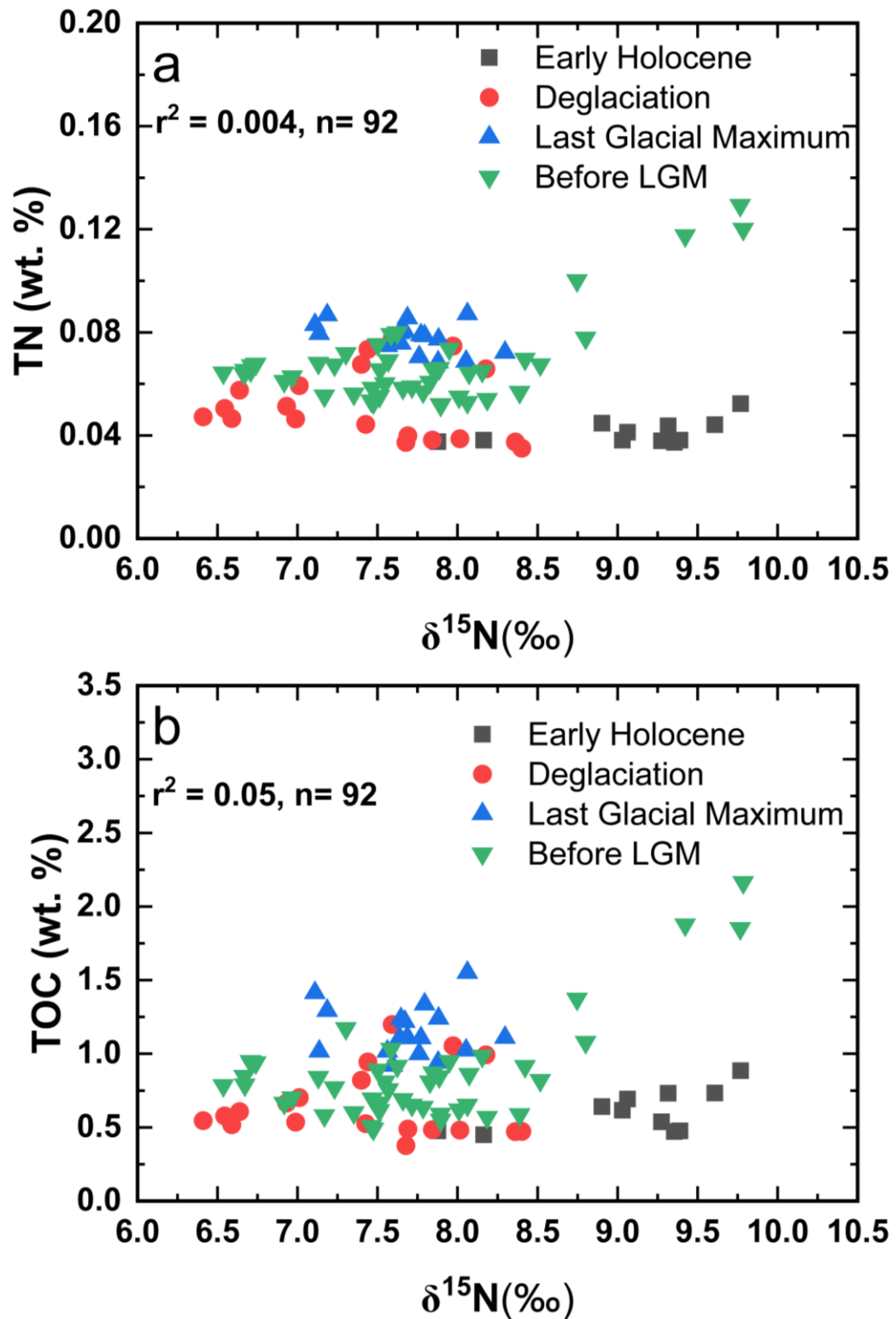


**Figure 5.3:** Correlation plots of (a)  $\delta^{15}\text{N}$  with TN (wt. %); and (b)  $\delta^{15}\text{N}$  with TOC (wt. %) in the sediment core SK-364/03. Different colours show data points belonging to four different times periods viz. the early Holocene, deglaciation, the last glacial maximum, and those before LGM.

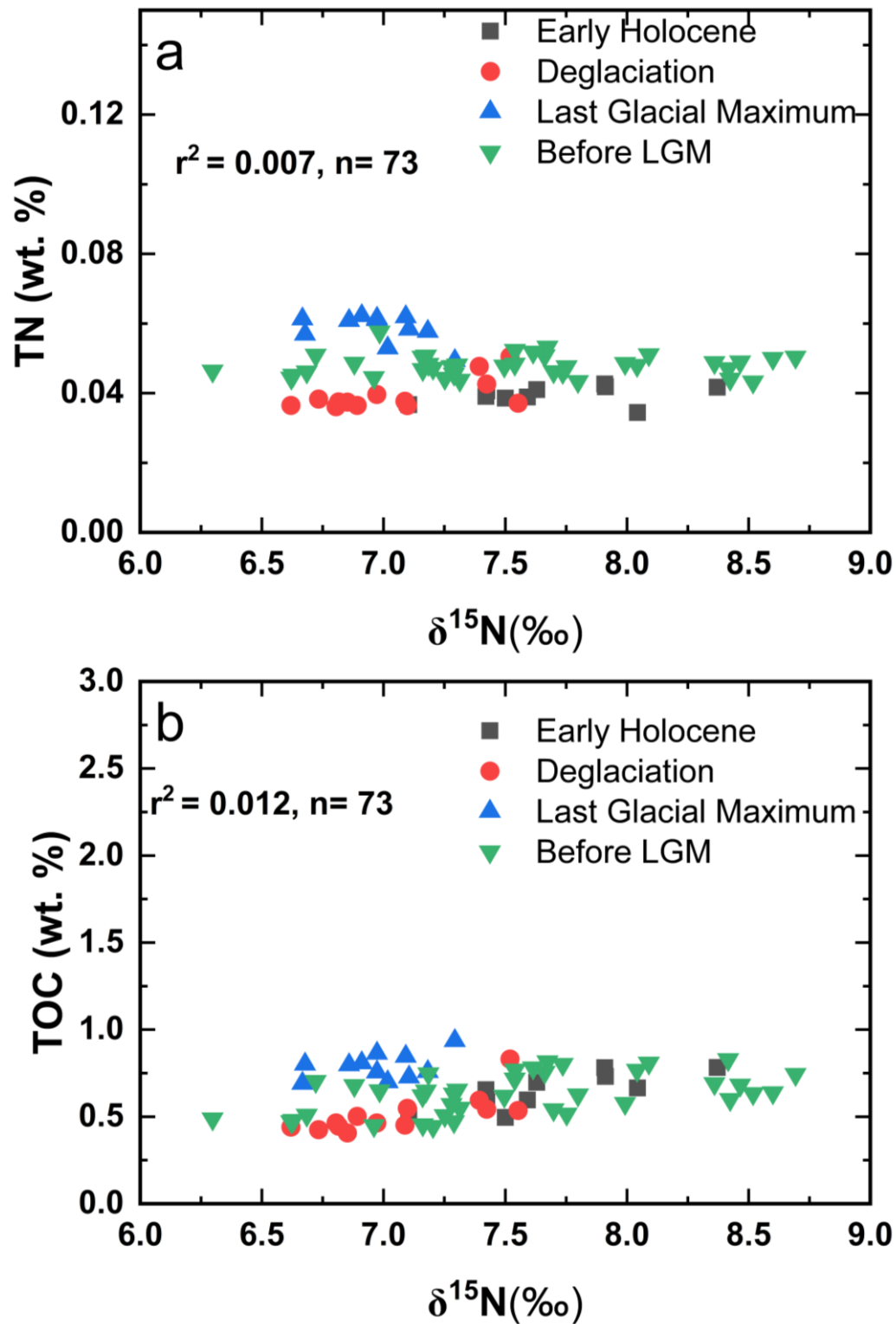


**Figure 5.4:** Correlations plots of (a)  $\delta^{15}\text{N}$  with TN (wt. %); and (b)  $\delta^{15}\text{N}$  with TOC (wt. %) in the sediment core SK-364/13. Different colours show data points belonging to four different time periods viz. the early Holocene, deglaciation, the last glacial maximum, and those before LGM.

#### 5.4.2 Nitrogen cycling during the glacial period

The  $\delta^{15}\text{N}$  of sinking particles collected from the five sediment traps in the Arabian Sea ranges from 5.1 to 8.5 ‰ (Gaye-Haake et al., 2005). These  $\delta^{15}\text{N}$  values largely coincide with  $\delta^{15}\text{N}$  of  $\text{NO}_3^-$  (7-9 ‰) at 100 – 150 m depth rather than in the subsurface, where denitrification persists. Denitrification enriches the residual  $\text{NO}_3^-$  in  $^{15}\text{N}$ , resulting in higher  $\delta^{15}\text{N}_{\text{NO}_3^-}$ . (Altabet et al., 1999; Naqvi et al., 2006). This similarity between the  $\delta^{15}\text{N}$  of the sinking particles and  $\delta^{15}\text{N}_{\text{NO}_3^-}$  at 100 -150 m indicates that the sinking particles acquire  $\text{NO}_3^-$  from this depth rather than from the denitrification-affected subsurface. The relatively low values of  $\delta^{15}\text{N}_{\text{NO}_3^-}$  are likely due to the introduction of new nitrogen to the euphotic zone through various processes, such as remineralization, nitrification and  $\text{N}_2$  fixation. This is further supported by relatively less negative  $\text{N}^*$  ( $\text{NO}_3^- - \text{PO}_4^{3-}/16$ ), a proxy to understand N cycling processes, indicating the presence of  $\text{N}_2$  fixation. The  $\text{N}_2$  fixation adds  $\delta^{15}\text{N} = 0$  ‰ endmember into the reservoir, counteracting the isotopic enrichment caused by denitrification during transport to the euphotic zone (Kao et al., 2015). This implies that  $\text{N}_2$  fixation and denitrification co-occur but at different depths in the Arabian Sea.

Water column denitrification starts when the dissolved  $\text{O}_2$  concentration is  $< 6 \mu\text{mol kg}^{-1}$  (Rixen et al., 2020). Our dissolved  $\text{O}_2$  reconstruction in both locations of the Arabian Sea (Chapter 4) indicates the presence of persistently deoxygenated waters with  $< 7 \mu\text{mol kg}^{-1}$  dissolved  $\text{O}_2$  till the LGM. These highly deoxygenated waters are conducive to denitrification with an enriched  $^{15}\text{N}$  signal. However, our records with lower  $\delta^{15}\text{N}$  in both regions indicate the suppression of the high denitrification  $\delta^{15}\text{N}$  signal by low  $\delta^{15}\text{N}$  signature of  $\text{N}_2$  fixation. Relatively lower  $\delta^{15}\text{N}$  values in the southeastern Arabian Sea as compared to the north suggest either less intensified denitrification in the southeast and/or intensification of  $\text{N}_2$  fixation. The former is more likely, as the southeastern region was relatively better oxygenated, as suggested by our I/Ca records (**Figure 5.5 (b)**). High rates of water column denitrification will, in turn, lead to an excess supply of phosphorus ( $\text{N/P} < 16$ ) to the surface for autotrophs to consume. In the northern Arabian Sea, upwelling would bring low N/P water to the surface. Assuming complete stoichiometric consumption of nutrients, the excess phosphorus will fuel  $\text{N}_2$  fixation. The remaining phosphorus will be advected to the south by surface ocean circulation. Along with the advected phosphorus, the subsurface excess phosphorus in the southeast will intensify  $\text{N}_2$  fixation in the southeastern Arabian Sea. The high denitrification during the glacial was probably due to enhanced primary productivity as evidenced by a high % TOC (**Figure 5.5 (c)**). Strengthened winter monsoon-driven convective mixing might have resulted in high

productivity during LGM, and this is further accompanied by a reduction of ventilation from the southern sourced waters leading the deoxygenation.

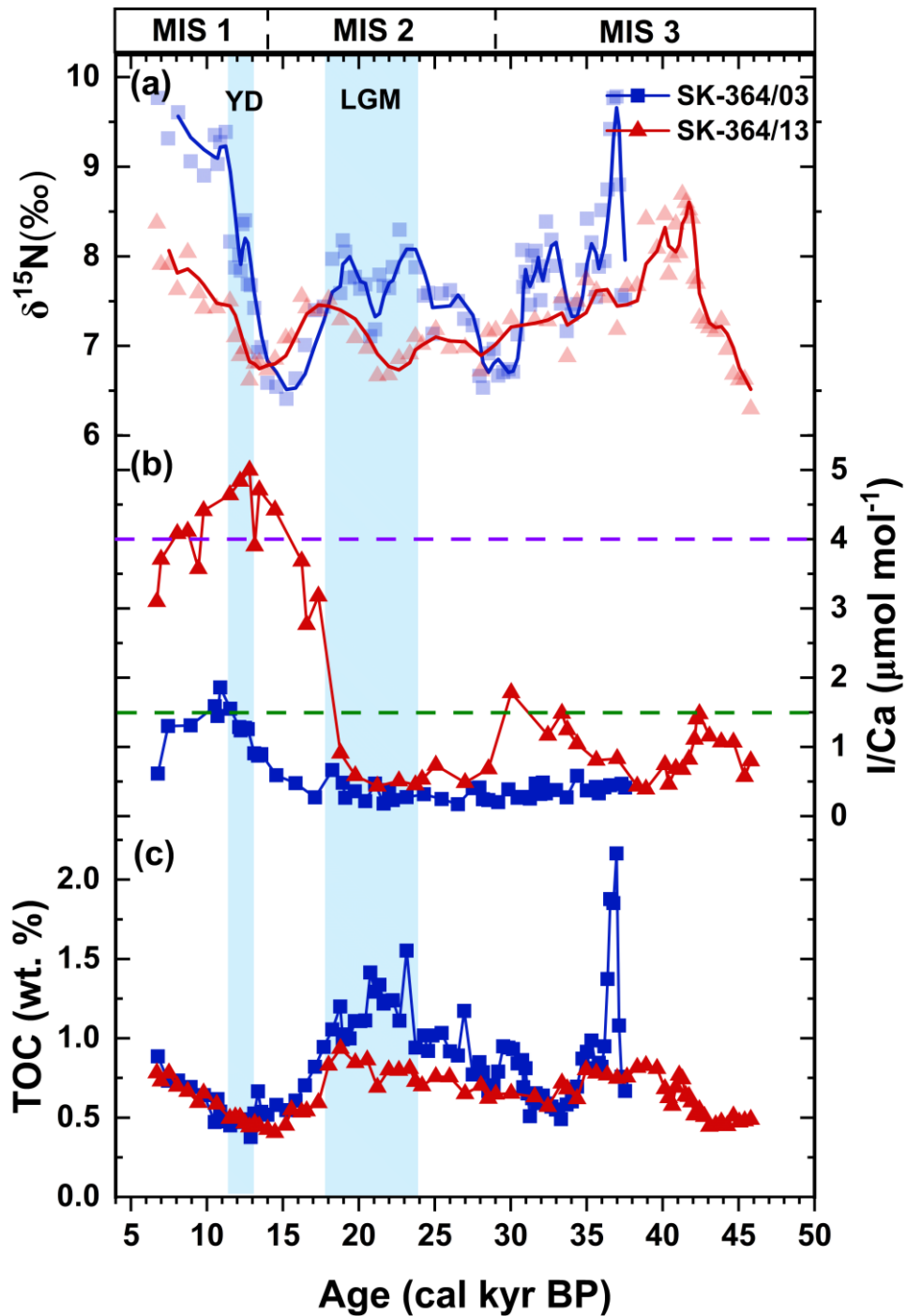


**Figure 5.5:** Temporal variations of (a) bulk sediments  $\delta^{15}\text{N}$ ; filled symbols (squares and triangles) show the data point, and the superimposed curves show the three-point running average; (b)  $\text{I}/\text{Ca}$  measured in *Trilobatus sacculifer*; Purple and green dashed horizontal lines indicate  $\text{I}/\text{Ca}$  values corresponding to  $100 \mu\text{mol kg}^{-1}$  and  $7 \mu\text{mol kg}^{-1}$  dissolved  $\text{O}_2$  concentrations, respectively; and (c) total organic carbon (TOC) contents.

#### 5.4.3 Nitrogen cycling during the deglaciation

Our  $\delta^{15}\text{N}$  records from both regions indicate a sudden decrease in denitrification after LGM, which agrees with the increase in dissolved  $\text{O}_2$  levels in both regions. Low denitrification during deglaciation was mainly due to the decreased surface primary productivity and increased ventilation from southern sourced waters like AAIW. During YD, denitrification was more intensified in the northern Arabian Sea than the south-eastern Arabian Sea, primarily due to the less oxygenated conditions in the northern Arabian Sea, evident by the lower I/Ca values in the north.

#### 5.4.4 Nitrogen cycling during the early Holocene

Our  $\delta^{15}\text{N}$  records from both regions indicate a transition from low denitrification into high denitrification during the late Holocene. This high denitrification is due to the lowering of dissolved  $\text{O}_2$  in the basin, which is shown by our I/Ca record (**Figure 5.5** (b)). Furthermore, denitrification in the north was more intense than in the southeast, likely due to more deoxygenated waters in the northern Arabian Sea. High denitrification in both regions is due to the low ventilation of the intermediate layers in the basin. Additionally, it has been suggested that due to the increase in sea level, the contribution of the intermediate water masses from the marginal seas increased. This might have hindered the northward movement of the southern-sourced intermediate waters and limited them to the south only.

#### 5.4.5 Comparison with previous studies in the Arabian Sea

We compared our records with  $\delta^{15}\text{N}$  records from the northern, eastern and southernmost records from the Arabian Sea (**Figure 5.6**). All records show similar trends with varying intensity of process incorporated by  $\delta^{15}\text{N}$  except the southernmost core (**Figure 5.7**). The southernmost core shows a decreasing trend of  $\delta^{15}\text{N}$  in the Holocene, opposite to other regions. This opposite trend is due to the predominance of  $\text{N}_2$  fixation (Kao et al., 2015). This high  $\text{N}_2$  fixation is probably due to the excess phosphorus from the north through the clockwise surface circulation. This high excess phosphorus is probably due to intensified water column denitrification and/ or enhanced upwelling in the northern Arabian. The  $\delta^{15}\text{N}$  patterns in the north during the Holocene suggest that synergetic processes are possible. All records suggest relatively higher denitrification during the LGM with prominent  $\text{N}_2$  fixation. Low  $\delta^{15}\text{N}$  values in the deglaciation indicate a reduction or absence of denitrification in the basin mainly due to the better-oxygenated conditions. In the Holocene, denitrification was intensified in the basin

except in the southern region. Slight offsets in these records suggest that the local process might interfere with the  $\delta^{15}\text{N}$  signal, modifying the basin-wide signals. All records show reduced denitrification during the Heinrich events 1 and 2. However, denitrification intensified during Heinrich event 3 (H3). This high denitrification during H3 might be due to the highly deoxygenated conditions observed. On the contrary, during H1 and H2, the water column was better oxygenated.

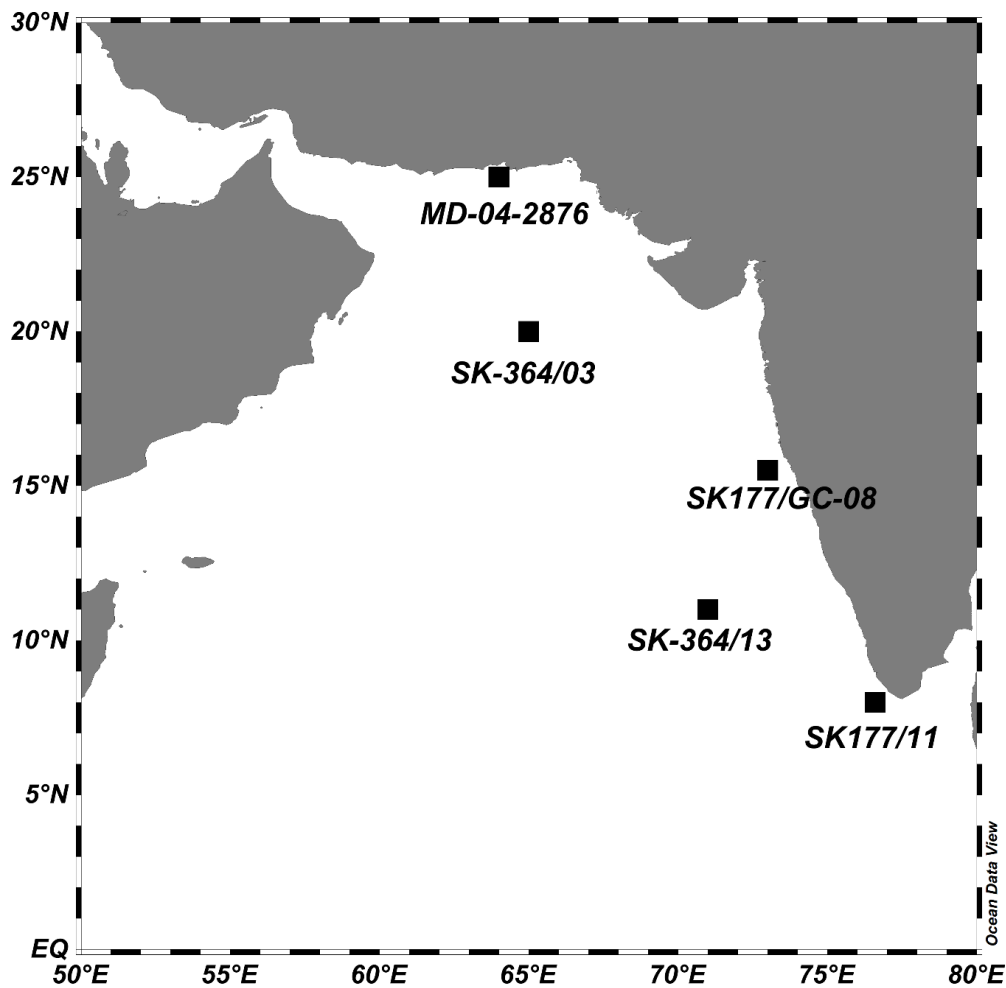


**Figure 5.6:** Map showing the locations of the sediment cores discussed. SK-364/03 & SK-364/13 (this study); MD-04-2876 (Pichevin et al. (2007)); SK177/GC-08 (Banakar et al. (2005)); SK177/11 (Kao et al. (2015)).

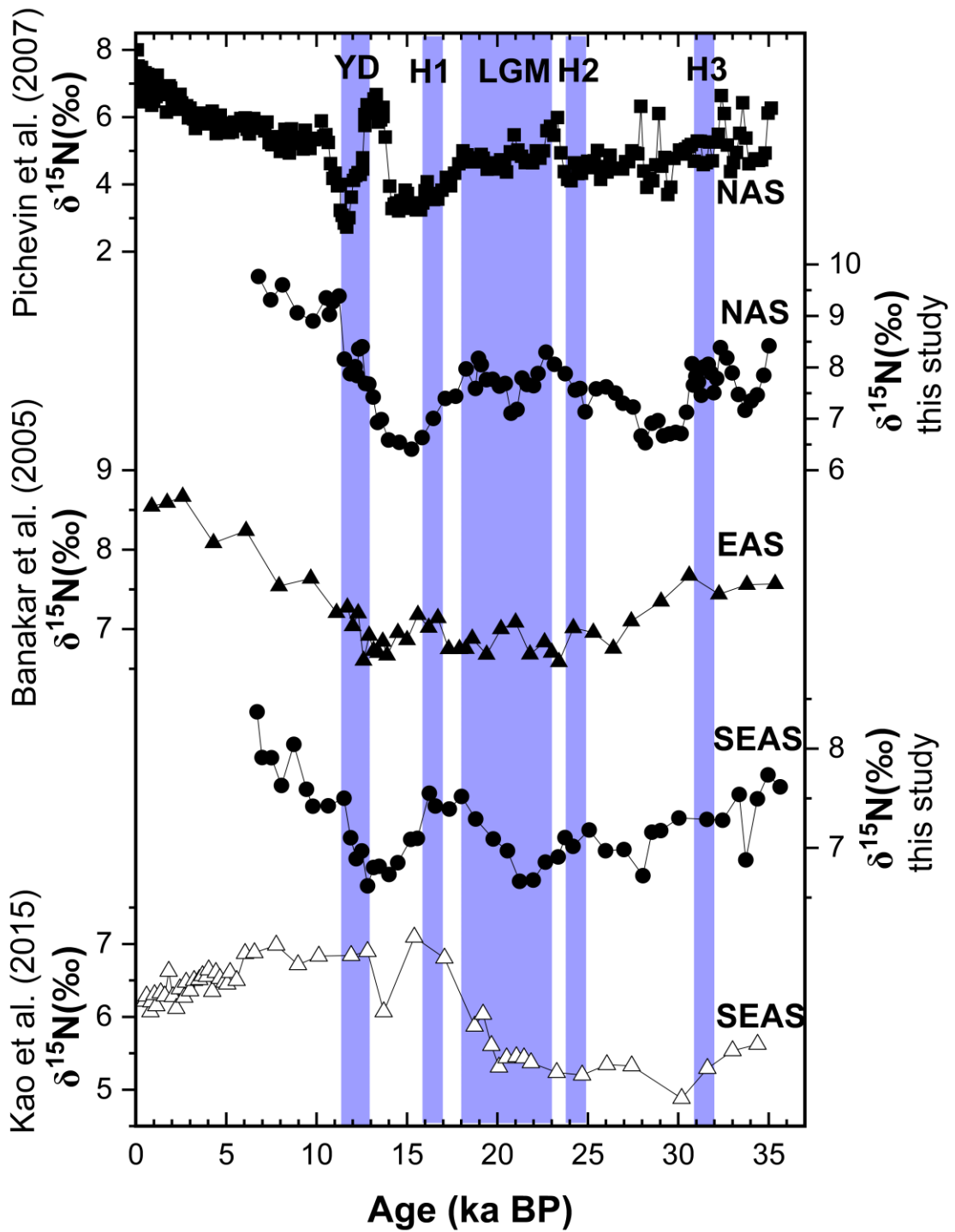


**Figure 5.7:** Comparison of our  $\delta^{15}\text{N}$  with other records from the basin.  $\delta^{15}\text{N}$  records are arranged longitudinally, with the northernmost record on top. H1, H2 and H3 are the Heinrich events. YD is the Younger Dryas event, and LGM is the Last Glacial Maxima.

## 5.5 Conclusion

In this chapter, we have presented a reconstruction of the past nitrogen cycle in the Arabian Sea using  $\delta^{15}\text{N}$  measurement on bulk sediments from two sediment cores.  $\delta^{15}\text{N}$  measurements are paired with  $\delta^{13}\text{C}_{\text{org}}$ , TN (wt. %), TOC (wt. %).

Here, we have observed higher denitrification with high  $\text{N}_2$  fixation in both the northern Arabian Sea and the southeastern Arabian Sea in the last glacial period.  $\text{N}_2$  fixation was higher in the southeastern Arabian Sea. Reduction or absence of denitrification was observed during the deglaciation, followed by intensification of denitrification in the early Holocene. In addition, denitrification was more intense in the north during the early Holocene. The intensified denitrification, along with the prominence of  $\text{N}_2$  fixation, might be due to the low dissolved  $\text{O}_2$  concentration in the intermediate depths, which creates a niche for  $\text{N}_2$  fixation in both regions during the glacial period. However, the presence of better-oxygenated conditions during deglaciation resulted in reduced or absence of denitrification. Furthermore, a decrease in dissolved  $\text{O}_2$  might have fuelled intensified denitrification in both regions. Other records from the Arabian Sea concur with our records, except the record from the southern tip of India, which shows a predominance of  $\text{N}_2$  fixation in the Holocene.

# Chapter 6

## Summary, limitations, and scope for future works

### 6.1 Summary

Present-day Arabian Sea has an intense OMZ in the intermediate depths, owing to the high surface primary productivity and poor ventilation. It is different from other OMZs in the sense that the oxygen-depleted conditions are found in the relatively oligotrophic central-eastern Arabian Sea, away from the highly productive western Arabian Sea. This is likely due to ventilation by intermediate water masses in the west. The Arabian Sea is fascinating, as the  $O_2$  variability on different timescales, linked to long-term climate variation, ocean, and atmospheric circulation, can be studied. This thesis investigated and reconstructed the spatio-temporal variation of dissolved  $O_2$  concentration on glacial-interglacial timescale and its potential drivers. The main findings of this work are summarized below.

#### 6.1.1 Proxy validation of iodine to calcium ratios from plankton tow and core-top foraminifera

- i. We have observed low I/Ca ratios from plankton tow foraminifera, especially from the Arabian Sea OMZ, similar to Eastern North Pacific OMZ.
- ii. Our core-top planktic foraminifera I/Ca ratios are low, agreeing with previous suggestions that low I/Ca ratios indicate low dissolved  $O_2$  waters.
- iii. Lower I/Ca ratios found in mixed populations (dominating foraminifera tests from deeper depths) suggest that deeper foraminifera capture I/Ca signals from relatively deeper depths.
- iv. The covariance observed between core-top I/Ca and minimum  $O_2$  concentrations reflects that the planktic foraminifera I/Ca indicates the dissolved  $O_2$  concentration in the intermediate depths.

### **6.1.2 Glacial – interglacial subsurface oxygen variability in the Arabian Sea**

- i. I/Ca, Mg/Ca, and % TOC measured on two sediment cores from the Arabian Sea show that the last glacial period was deoxygenated, probably due to enhanced primary productivity owing to strengthened winter monsoon-driven convective mixing and poor ventilation from the southern sourced intermediate waters.
- ii. An increasing dissolved O<sub>2</sub> trend in the deglaciation is due to the lower primary productivity coupled with intense ventilation of the intermediate waters from southern sourced waters (e.g., AAIW).
- iii. High dissolved O<sub>2</sub> during Younger Dryas was possibly due to the reduced surface primary productivity and higher subsurface ventilation by the intermediate water masses from the adjacent Red Sea, Persian Gulf, and southern sourced water masses.
- iv. During the early Holocene, the gradual decrease in the dissolved O<sub>2</sub> concentration is best explained by the reduction of ventilation from the southern sources of water masses.
- v. The O<sub>2</sub> increase beyond the Last Glacial Maximum during deglaciation is higher in the southeastern Arabian Sea as compared to the northern region, with values >100 μmol kg<sup>-1</sup> in the water column, suggesting a well-oxygenated water column during Younger Dryas in the southeast, primarily due to the more ventilation of the southeast.

### **6.1.3 Paleo-nitrogen cycling in the Arabian Sea**

- i. In the glacial period, higher denitrification is coupled with high N<sub>2</sub> fixation in the north and southeastern Arabian Sea. N<sub>2</sub> fixation was higher in the southeast compared to the northern Arabian Sea.
- ii. During the deglaciation, denitrification was reduced or absent in both regions of the Arabian Sea due to the better-oxygenated conditions in the basin.
- iii. In the early Holocene, denitrification was enhanced in both regions but was more intense in the northern Arabian Sea, probably due to decreased dissolved O<sub>2</sub>.

## **6.2 Limitations**

While this study significantly contributes to the understanding of paleo oxygenation in the Arabian Sea, several limitations should be acknowledged. The following are the limitations:

- i. The unavailability of in-situ dissolved O<sub>2</sub> measurements alongside plankton tows hindered the comparison of plankton tow foraminifera I/Ca with dissolved O<sub>2</sub>.

- ii. The sample size in terms of the geographical locations sampled for plankton tow and core-top samples was relatively small, which may limit the generalization of the findings.
- iii. The plankton tow foraminifera tests abundance was very low at discrete depths, due to which limited species-specific measurements were made.
- iv. The Plankton tow samples are only from a single year and season. Multi-year and seasonal sampling is required to make a more suitable comparison with the core-top foraminifera I/Ca.
- v. For paleo reconstructions, sediment cores from only the north and southeastern Arabian Sea were used in the present work. Samples from other locations in the Arabian Sea can help provide a more comprehensive picture of the whole basin.
- vi. Also, no I/Ca measurements on deeper dwelling species were performed, which limits our inferences about the vertical expansion or shrinking of the OMZ.

### **6.3 Scope for future works**

This thesis presented significant findings related to past processes in the Arabian Sea. However, further work must be carried out to improve our understanding of the dynamics of the northern Indian Ocean OMZ. We suggest to carry out the following in the future:

- i. The vertical extent of the OMZ of the Arabian Sea remains unexplored. This can be done by complimenting the present data with proxy reconstructions from sediment cores from the continental shelves, like in the eastern Arabian Sea.
- ii. The spatial and temporal evolution of the OMZ of the Bay of Bengal has not been studied in relation to the changing monsoonal conditions in the past.
- iii. The threshold behaviour of the I/Ca proxy is not well understood. This can be achieved by simultaneously measuring water column iodine species and dissolved O<sub>2</sub>.



# References

- Agnihotri, R., Bhattacharya, S. K., Sarin, M. M., & Somayajulu, B. L. K. (2003). Changes in surface productivity and subsurface denitrification during the Holocene: a multiproxy study from the eastern Arabian Sea. *The Holocene*, *13*(5), 701–713. <https://doi.org/10.1191/0959683603hl656rp>
- Altabet, M. A. (2007). Constraints on oceanic N balance/imbalance from sedimentary  $^{15}\text{N}$  records. *Biogeosciences*, *4*(1), 75–86. <https://doi.org/10.5194/bg-4-75-2007>
- Altabet, M. A., & Francois, R. (1994). Sedimentary nitrogen isotopic ratio as a recorder for surface ocean nitrate utilization. *Global Biogeochemical Cycles*, *8*(1), 103–116. <https://doi.org/10.1029/93GB03396>
- Altabet, M. A., & Francois, R. (2001). Nitrogen isotope biogeochemistry of the Antarctic Polar Frontal Zone at 170°W. *Deep Sea Research Part II: Topical Studies in Oceanography*, *48*(19), 4247–4273. [https://doi.org/10.1016/S0967-0645\(01\)00088-1](https://doi.org/10.1016/S0967-0645(01)00088-1)
- Altabet, M. A., Deuser, W. G., Honjo, S., & Stienen, C. (1991). Seasonal and depth-related changes in the source of sinking particles in the North Atlantic. *Nature*, *354*(6349), 136–139. <https://doi.org/10.1038/354136a0>
- Altabet, M. A., Francois, R., Murray, D. W., & Prell, W. L. (1995). Climate-related variations in denitrification in the Arabian Sea from sediment  $^{15}\text{N}/^{14}\text{N}$  ratios. *Nature*, *373*(6514), 506–509. <https://doi.org/10.1038/373506a0>
- Altabet, M. A., Murray, D. W., & Prell, W. L. (1999). Climatically linked oscillations in Arabian Sea denitrification over the past 1 m.y.: Implications for the marine N cycle. *Paleoceanography*, *14*(6), 732–743. <https://doi.org/10.1029/1999PA900035>
- Altabet, M. A., Higginson, M. J., & Murray, D. W. (2002). The effect of millennial-scale changes in Arabian Sea denitrification on atmospheric  $\text{CO}_2$ . *Nature*, *415*(6868), 159–162. <https://doi.org/10.1038/415159a>

- Anand, P., Elderfield, H., & Conte, M. H. (2003). Calibration of Mg/Ca thermometry in planktonic foraminifera from a sediment trap time series. *Paleoceanography*, *18*(2). <https://doi.org/10.1029/2002PA000846>
- Anil Kumar, A., Rao, V. P., Patil, S. K., Kessarkar, P. M., & Thamban, M. (2005). Rock magnetic records of the sediments of the eastern Arabian Sea: Evidence for late Quaternary climatic change. *Marine Geology*, *220*(1), 59–82. <https://doi.org/10.1016/j.margeo.2005.06.038>
- Bali, K., Mishra, A. K., Singh, S., Chandra, S., & Lehahn, Y. (2019). Impact of dust storm on phytoplankton bloom over the Arabian Sea: a case study during March 2012. *Environmental Science and Pollution Research*, *26*(12), 11940–11950. <https://doi.org/10.1007/s11356-019-04602-7>
- Banakar, V. K., Oba, T., Chodankar, A. R., Kuramoto, T., Yamamoto, M., & Minagawa, M. (2005). Monsoon related changes in sea surface productivity and water column denitrification in the Eastern Arabian Sea during the last glacial cycle. *Marine Geology*, *219*(2), 99–108. <https://doi.org/10.1016/j.margeo.2005.05.004>
- Bange, H., Naqvi, S. W. A., & Codispoti, L. A. (2005). The nitrogen cycle in the Arabian Sea. Retrieved from <http://drs.nio.org/drs/handle/2264/898>
- Bange, H., Freing, A., Kock, A., & Löscher, C. (2010). Marine pathways to Nitrous Oxide. *Nitrous Oxide and Climate Change*, 36–62. <https://doi.org/10.4324/9781849775113>
- Banse, K., Naqvi, S. W. A., Narvekar, P. V., Postel, J. R., & Jayakumar, D. A. (2014). Oxygen minimum zone of the open Arabian Sea: variability of oxygen and nitrite from daily to decadal timescales. *Biogeosciences*, *11*(8), 2237–2261. <https://doi.org/10.5194/bg-11-2237-2014>
- Barker, S., Greaves, M., & Elderfield, H. (2003). A study of cleaning procedures used for foraminiferal Mg/Ca paleothermometry. *Geochemistry, Geophysics, Geosystems*, *4*(9). <https://doi.org/10.1029/2003GC000559>
- Bartolacci, D. M., & Luther, M. E. (1999). Patterns of co-variability between physical and biological parameters in the Arabian Sea. *Deep Sea Research Part II: Topical Studies in Oceanography*, *46*(8), 1933–1964. [https://doi.org/10.1016/S0967-0645\(99\)00049-1](https://doi.org/10.1016/S0967-0645(99)00049-1)

- Bhushan, R., Yadava, M. G., Shah, M. S., & Raj, H. (2019). Performance of a new 1MV AMS facility (AURiS) at PRL, Ahmedabad, India. *Nuclear Instruments and Methods in Physics Research Section B: Beam Interactions with Materials and Atoms*, 439, 76–79. <https://doi.org/10.1016/j.nimb.2018.12.003>
- Bialik, O. M., Auer, G., Ogawa, N. O., Kroon, D., Waldmann, N. D., & Ohkouchi, N. (2020). Monsoons, Upwelling, and the Deoxygenation of the Northwestern Indian Ocean in Response to Middle to Late Miocene Global Climatic Shifts. *Paleoceanography and Paleoclimatology*, 35(2), e2019PA003762. <https://doi.org/10.1029/2019PA003762>
- Böning, P., & Bard, E. (2009). Millennial/centennial-scale thermocline ventilation changes in the Indian Ocean as reflected by aragonite preservation and geochemical variations in Arabian Sea sediments. *Geochimica et Cosmochimica Acta*, 73(22), 6771–6788. <https://doi.org/10.1016/j.gca.2009.08.028>
- Bopp, L., Resplandy, L., Orr, J. C., Doney, S. C., Dunne, J. P., Gehlen, M., et al. (2013). Multiple stressors of ocean ecosystems in the 21st century: projections with CMIP5 models. *Biogeosciences*, 10(10), 6225–6245. <https://doi.org/10.5194/bg-10-6225-2013>
- Bower, A. S., Hunt, H. D., & Price, J. F. (2000). Character and dynamics of the Red Sea and Persian Gulf outflows. *Journal of Geophysical Research: Oceans*, 105(C3), 6387–6414. <https://doi.org/10.1029/1999JC900297>
- Brandes, J. A., & Devol, A. H. (2002). A global marine-fixed nitrogen isotopic budget: Implications for Holocene nitrogen cycling. *Global Biogeochemical Cycles*, 16(4), 671–684. <https://doi.org/10.1029/2001GB001856>
- Breitburg, D. (2002). Effects of hypoxia, and the balance between hypoxia and enrichment, on coastal fishes and fisheries. *Estuaries*, 25(4), 767–781. <https://doi.org/10.1007/BF02804904>
- Breitburg, D., Levin, L. A., Oschlies, A., Grégoire, M., Chavez, F. P., Conley, D. J., et al. (2018). Declining oxygen in the global ocean and coastal waters. *Science*, 359(6371). <https://doi.org/10.1126/science.aam7240>
- Brewer, P. G., & Peltzer, E. T. (2017). Depth perception: the need to report ocean biogeochemical rates as functions of temperature, not depth. *Philosophical*

*Transactions of the Royal Society A: Mathematical, Physical and Engineering Sciences*, 375(2102), 20160319. <https://doi.org/10.1098/rsta.2016.0319>

- Bryan, S. P., Marchitto, T. M., & Lehman, S. J. (2010). The release of <sup>14</sup>C-depleted carbon from the deep ocean during the last deglaciation: Evidence from the Arabian Sea. *Earth and Planetary Science Letters*, 298(1), 244–254. <https://doi.org/10.1016/j.epsl.2010.08.025>
- Calvert, S., Pedersen, T., Naidu, P. D., & Stackelberg, U. (1995). On the organic carbon maximum on the continental slope of the eastern Arabian Sea. <https://doi.org/10.1357/0022240953213232>
- Canfield, D. E. (1994). Factors influencing organic carbon preservation in marine sediments. *Chemical Geology*, 114(3), 315–329. [https://doi.org/10.1016/0009-2541\(94\)90061-2](https://doi.org/10.1016/0009-2541(94)90061-2)
- Canfield, D. E. (2015, December 1). Oxygen | Princeton University Press. Retrieved February 11, 2024, from <https://press.princeton.edu/books/paperback/9780691168364/oxygen>
- Canfield, D. E., & Thamdrup, B. (2009). Towards a consistent classification scheme for geochemical environments, or, why we wish the term ‘suboxic’ would go away. *Geobiology*, 7(4), 385–392. <https://doi.org/10.1111/j.1472-4669.2009.00214.x>
- Capone, D. G., Zehr, J. P., Paerl, H. W., Bergman, B., & Carpenter, E. J. (1997). *Trichodesmium*, a Globally Significant Marine Cyanobacterium. *Science*, 276(5316), 1221–1229. <https://doi.org/10.1126/science.276.5316.1221>
- Chance, R., Baker, A. R., Carpenter, L., & Jickells, T. D. (2014). The distribution of iodide at the sea surface. *Environmental Science: Processes & Impacts*, 16(8), 1841–1859. <https://doi.org/10.1039/C4EM00139G>
- Chatterjee, A., Shankar, D., McCreary, J. P., Vinayachandran, P. N., & Mukherjee, A. (2017). Dynamics of Andaman Sea circulation and its role in connecting the equatorial Indian Ocean to the Bay of Bengal. *Journal of Geophysical Research: Oceans*, 122(4), 3200–3218. <https://doi.org/10.1002/2016JC012300>

- Codispoti, L. A., & Christensen, J. P. (1985). Nitrification, denitrification and nitrous oxide cycling in the eastern tropical South Pacific ocean. *Marine Chemistry*, *16*(4), 277–300. [https://doi.org/10.1016/0304-4203\(85\)90051-9](https://doi.org/10.1016/0304-4203(85)90051-9)
- Deutsch, C., Sigman, D. M., Thunell, R. C., Meckler, A. N., & Haug, G. H. (2004). Isotopic constraints on glacial/interglacial changes in the oceanic nitrogen budget. *Global Biogeochemical Cycles*, *18*(4). <https://doi.org/10.1029/2003GB002189>
- Deutsch, C., Sarmiento, J. L., Sigman, D. M., Gruber, N., & Dunne, J. P. (2007). Spatial coupling of nitrogen inputs and losses in the ocean. *Nature*, *445*(7124), 163–167. <https://doi.org/10.1038/nature05392>
- Deutsch, C., Brix, H., Ito, T., Frenzel, H., & Thompson, L. (2011). Climate-Forced Variability of Ocean Hypoxia. *Science*, *333*(6040), 336–339. <https://doi.org/10.1126/science.1202422>
- Diaz, R. J. (2016). Anoxia, Hypoxia, And Dead Zones. In M. J. Kennish (Ed.), *Encyclopedia of Estuaries* (pp. 19–29). Dordrecht: Springer Netherlands. [https://doi.org/10.1007/978-94-017-8801-4\\_82](https://doi.org/10.1007/978-94-017-8801-4_82)
- Diaz, R. J., & Rosenberg, R. (2008). Spreading Dead Zones and Consequences for Marine Ecosystems. *Science*, *321*(5891), 926–929. <https://doi.org/10.1126/science.1156401>
- Dickson, R. R., & Brown, J. (1994). The production of North Atlantic Deep Water: Sources, rates, and pathways. *Journal of Geophysical Research: Oceans*, *99*(C6), 12319–12341. <https://doi.org/10.1029/94JC00530>
- Dueser, W. G., Ross, E. H., & Mlodzinska, Z. J. (1978). Evidence for and rate of denitrification in the Arabian Sea. *Deep Sea Research*, *25*(5), 431–445. [https://doi.org/10.1016/0146-6291\(78\)90551-9](https://doi.org/10.1016/0146-6291(78)90551-9)
- Dutta, K., Bhushan, R., & Somayajulu, B. L. K. (2001).  $\Delta R$  Correction Values for the Northern Indian Ocean. *Radiocarbon*, *43*(2A), 483–488. <https://doi.org/10.1017/S0033822200038376>
- Erdem, Z., Schönfeld, J., Rathburn, A. E., Pérez, M.-E., Cardich, J., & Glock, N. (2020). Bottom-water deoxygenation at the Peruvian margin during the last deglaciation

recorded by benthic foraminifera. *Biogeosciences*, 17(12), 3165–3182.  
<https://doi.org/10.5194/bg-17-3165-2020>

Fairbanks, R. G. (1989). A 17,000-year glacio-eustatic sea level record: influence of glacial melting rates on the Younger Dryas event and deep-ocean circulation. *Nature*, 342(6250), 637–642. <https://doi.org/10.1038/342637a0>

Falkowski, P. G. (1997). Evolution of the nitrogen cycle and its influence on the biological sequestration of CO<sub>2</sub> in the ocean. *Nature*, 387(6630), 272–275.  
<https://doi.org/10.1038/387272a0>

Falkowski, P. G., & Raven, J. A. (2007, February 11). *Aquatic Photosynthesis* | Princeton University Press. Retrieved February 12, 2024, from <https://press.princeton.edu/books/paperback/9780691115511/aquatic-photosynthesis>

Feng, X., & Redfern, S. A. T. (2018). Iodate in calcite, aragonite and vaterite CaCO<sub>3</sub>: Insights from first-principles calculations and implications for the I/Ca geochemical proxy. *Geochimica et Cosmochimica Acta*, 236, 351–360.  
<https://doi.org/10.1016/j.gca.2018.02.017>

Ganeshram, R. S., Pedersen, T. F., Calvert, S. E., & Murray, J. W. (1995). Large changes in oceanic nutrient inventories from glacial to interglacial periods. *Nature*, 376(6543), 755–758. <https://doi.org/10.1038/376755a0>

Garcia, H. E., & Gordon, L. I. (1992). Oxygen solubility in seawater: Better fitting equations. *Limnology and Oceanography*, 37(6), 1307–1312.  
<https://doi.org/10.4319/lo.1992.37.6.1307>

Gaye-Haake, B., Lahajnar, N., Emeis, K.-Ch., Unger, D., Rixen, T., Suthhof, A., et al. (2005). Stable nitrogen isotopic ratios of sinking particles and sediments from the northern Indian Ocean. *Marine Chemistry*, 96(3), 243–255.  
<https://doi.org/10.1016/j.marchem.2005.02.001>

Gomes, H., Goes, J. I., Matondkar, S. G. P., Buskey, E. J., Basu, S., Parab, S., & Thoppil, P. (2014). Massive outbreaks of *Noctiluca scintillans* blooms in the Arabian Sea due to spread of hypoxia. *Nature Communications*, 5(1), 4862.  
<https://doi.org/10.1038/ncomms5862>

- Gruber, N., & Galloway, J. N. (2008). An Earth-system perspective of the global nitrogen cycle. *Nature*, 451(7176), 293–296. <https://doi.org/10.1038/nature06592>
- Gruber, N., & Sarmiento, J. L. (1997). Global patterns of marine nitrogen fixation and denitrification. *Global Biogeochemical Cycles*, 11(2), 235–266. <https://doi.org/10.1029/97GB00077>
- Hardisty, D. S., Horner, T. J., Wankel, S. D., Blusztajn, J., & Nielsen, S. G. (2020). Experimental observations of marine iodide oxidation using a novel sparge-interface MC-ICP-MS technique. *Chemical Geology*, 532, 119360. <https://doi.org/10.1016/j.chemgeo.2019.119360>
- Hardisty, D. S., Horner, T. J., Evans, N., Moriyasu, R., Babbin, A. R., Wankel, S. D., et al. (2021). Limited iodate reduction in shipboard seawater incubations from the Eastern Tropical North Pacific oxygen deficient zone. *Earth and Planetary Science Letters*, 554, 116676. <https://doi.org/10.1016/j.epsl.2020.116676>
- Haug, G. H., Pedersen, T. F., Sigman, D. M., Calvert, S. E., Nielsen, B., & Peterson, L. C. (1998). Glacial/interglacial variations in production and nitrogen fixation in the Cariaco Basin during the last 580 kyr. *Paleoceanography*, 13(5), 427–432. <https://doi.org/10.1029/98PA01976>
- Helm, K. P., Bindoff, N. L., & Church, J. A. (2011). Observed decreases in oxygen content of the global ocean. *Geophysical Research Letters*, 38(23). <https://doi.org/10.1029/2011GL049513>
- Hess, A. V., Auderset, A., Rosenthal, Y., Miller, K. G., Zhou, X., Sigman, D. M., & Martínez-García, A. (2023). A well-oxygenated eastern tropical Pacific during the warm Miocene. *Nature*, 1–5. <https://doi.org/10.1038/s41586-023-06104-6>
- van Heuven, S. M. A. C., Hoppema, M., Huhn, O., Slagter, H. A., & de Baar, H. J. W. (2011). Direct observation of increasing CO<sub>2</sub> in the Weddell Gyre along the Prime Meridian during 1973–2008. *Deep Sea Research Part II: Topical Studies in Oceanography*, 58(25), 2613–2635. <https://doi.org/10.1016/j.dsr2.2011.08.007>

- Holland, H. D. (2006). The oxygenation of the atmosphere and oceans. *Philosophical Transactions of the Royal Society of London. Series B, Biological Sciences*, 361(1470), 903–915. <https://doi.org/10.1098/rstb.2006.1838>
- Hoogakker, B. A. A., Lu, Z., Umling, N., Jones, L., Zhou, X., Rickaby, R. E. M., et al. (2018). Glacial expansion of oxygen-depleted seawater in the eastern tropical Pacific. *Nature*, 562(7727), 410–413. <https://doi.org/10.1038/s41586-018-0589-x>
- Hua, Q., Barbetti, M., Fink, D., Kaiser, K. F., Friedrich, M., Kromer, B., et al. (2009). Atmospheric  $^{14}\text{C}$  variations derived from tree rings during the early Younger Dryas. *Quaternary Science Reviews*, 28(25–26), 2982–2990. <https://doi.org/10.1016/j.quascirev.2009.08.013>
- Ito, T., Minobe, S., Long, M. C., & Deutsch, C. (2017). Upper ocean  $\text{O}_2$  trends: 1958–2015. *Geophysical Research Letters*, 44(9), 4214–4223. <https://doi.org/10.1002/2017GL073613>
- Jaccard, S. L., & Galbraith, E. D. (2012). Large climate-driven changes of oceanic oxygen concentrations during the last deglaciation. *Nature Geoscience*, 5(2), 151–156. <https://doi.org/10.1038/ngeo1352>
- Janssen, D. J., Conway, T. M., John, S. G., Christian, J. R., Kramer, D. I., Pedersen, T. F., & Cullen, J. T. (2014). Undocumented water column sink for cadmium in open ocean oxygen-deficient zones. *Proceedings of the National Academy of Sciences*, 111(19), 6888–6893. <https://doi.org/10.1073/pnas.1402388111>
- Jenkyns, H. C. (2010). Geochemistry of oceanic anoxic events. *Geochemistry, Geophysics, Geosystems*, 11(3). <https://doi.org/10.1029/2009GC002788>
- Kamykowski, D., & Zentara, S.-J. (1990). Hypoxia in the world ocean as recorded in the historical data set. *Deep Sea Research Part A. Oceanographic Research Papers*, 37(12), 1861–1874. [https://doi.org/10.1016/0198-0149\(90\)90082-7](https://doi.org/10.1016/0198-0149(90)90082-7)
- Kao, S.-J., Wang, B.-Y., Zheng, L.-W., Selvaraj, K., Hsu, S.-C., Sean Wan, X. H., et al. (2015). Spatiotemporal variations of nitrogen isotopic records in the Arabian Sea. *Biogeosciences*, 12(1), 1–14. <https://doi.org/10.5194/bg-12-1-2015>

- Karim, A., & Veizer, J. (2002). Water balance of the Indus River Basin and moisture source in the Karakoram and western Himalayas: Implications from hydrogen and oxygen isotopes in river water. *Journal of Geophysical Research: Atmospheres*, *107*(D18), ACH 9-1-ACH 9-12. <https://doi.org/10.1029/2000JD000253>
- Karl, D., Letelier, R., Tupas, L., Dore, J., Christian, J., & Hebel, D. (1997). The role of nitrogen fixation in biogeochemical cycling in the subtropical North Pacific Ocean. *Nature*, *388*(6642), 533–538. <https://doi.org/10.1038/41474>
- Karstensen, J., & Tomczak, M. (1997). Ventilation processes and water mass ages in the thermocline of the southeast Indian Ocean. *Geophysical Research Letters*, *24*(22), 2777–2780. <https://doi.org/10.1029/97GL02708>
- Kast, E. R., Stolper, D. A., Auderset, A., Higgins, J. A., Ren, H., Wang, X. T., et al. (2019). Nitrogen isotope evidence for expanded ocean suboxia in the early Cenozoic. *Science*, *364*(6438), 386–389. <https://doi.org/10.1126/science.aau5784>
- Keeling, R. F., Körtzinger, A., & Gruber, N. (2010). Ocean Deoxygenation in a Warming World. *Annual Review of Marine Science*, *2*(1), 199–229. <https://doi.org/10.1146/annurev.marine.010908.163855>
- Kim, H., Franco, A. C., & Sumaila, U. R. (2023). A Selected Review of Impacts of Ocean Deoxygenation on Fish and Fisheries. *Fishes*, *8*(6), 316. <https://doi.org/10.3390/fishes8060316>
- Klöcker, R., Ganssen, G., Jung, S. J. A., Kroon, D., & Henrich, R. (2006). Late Quaternary millennial-scale variability in pelagic aragonite preservation off Somalia. *Marine Micropaleontology*, *59*(3), 171–183. <https://doi.org/10.1016/j.marmicro.2006.02.004>
- Kumar, S. P., & Prasad, T. G. (1996). Winter cooling in the northern Arabian Sea. *Current Science*, *71*.
- Kumar, S. P., Madhupratap, M., Kumar, M. D., Muraleedharan, P. M., de Souza, S. N., Gauns, M., & Sarma, V. V. S. S. (2001). High biological productivity in the central Arabian Sea during the summer monsoon driven by Ekman pumping and lateral advection. *Current Science*, *81*(12), 1633–1638.

- Kurian, J., & Vinayachandran, P. N. (2007). Mechanisms of formation of the Arabian Sea mini warm pool in a high-resolution Ocean General Circulation Model. *Journal of Geophysical Research: Oceans*, *112*(C5). <https://doi.org/10.1029/2006JC003631>
- Lachkar, Z., Lévy, M., & Smith, K. S. (2019). Strong Intensification of the Arabian Sea Oxygen Minimum Zone in Response to Arabian Gulf Warming. *Geophysical Research Letters*, *46*(10), 5420–5429. <https://doi.org/10.1029/2018GL081631>
- Lachkar, Z., Lévy, M., Hailegeorgis, D., & Vallivattathillam, P. (2023). Differences in recent and future trends in the Arabian Sea oxygen minimum zone: processes and uncertainties. *Frontiers in Marine Science*, *10*. Retrieved from <https://www.frontiersin.org/articles/10.3389/fmars.2023.1122043>
- Lambs, L., Balakrishna, K., Brunet, F., & Probst, J. L. (2005). Oxygen and hydrogen isotopic composition of major Indian rivers: a first global assessment. *Hydrological Processes*, *19*(17), 3345–3355. <https://doi.org/10.1002/hyp.5974>
- Lee, C. M., Jones, B. H., Brink, K. H., & Fischer, A. S. (2000). The upper-ocean response to monsoonal forcing in the Arabian Sea: seasonal and spatial variability. *Deep Sea Research Part II: Topical Studies in Oceanography*, *47*(7), 1177–1226. [https://doi.org/10.1016/S0967-0645\(99\)00141-1](https://doi.org/10.1016/S0967-0645(99)00141-1)
- Libby, W. F., Anderson, E. C., & Arnold, J. R. (1949). Age Determination by Radiocarbon Content: World-Wide Assay of Natural Radiocarbon. *Science*, *109*(2827), 227–228. <https://doi.org/10.1126/science.109.2827.227>
- Liu, K.-K., & Kaplan, I. R. (1989). The eastern tropical Pacific as a source of <sup>15</sup>N-enriched nitrate in seawater off southern California. *Limnology and Oceanography*, *34*(5), 820–830. <https://doi.org/10.4319/lo.1989.34.5.0820>
- Lourey, M. J., Trull, T. W., & Sigman, D. M. (2003). Sensitivity of  $\delta^{15}\text{N}$  of nitrate, surface suspended and deep sinking particulate nitrogen to seasonal nitrate depletion in the Southern Ocean. *Global Biogeochemical Cycles*, *17*(3). <https://doi.org/10.1029/2002GB001973>
- Lu, W., Dickson, A. J., Thomas, E., Rickaby, R. E. M., Chapman, P., & Lu, Z. (2020). Refining the planktic foraminiferal I/Ca proxy: Results from the Southeast Atlantic Ocean.

- Geochimica et Cosmochimica Acta*, 287, 318–327.  
<https://doi.org/10.1016/j.gca.2019.10.025>
- Lu, Z., Jenkyns, H. C., & Rickaby, R. E. M. (2010). Iodine to calcium ratios in marine carbonate as a paleo-redox proxy during oceanic anoxic events. *Geology*, 38(12), 1107–1110. <https://doi.org/10.1130/G31145.1>
- Lu, Z., Hoogakker, B. A. A., Hillenbrand, C.-D., Zhou, X., Thomas, E., Gutchess, K. M., et al. (2016). Oxygen depletion recorded in upper waters of the glacial Southern Ocean. *Nature Communications*, 7(1), 11146. <https://doi.org/10.1038/ncomms11146>
- Lyons, T. W., Reinhard, C. T., & Planavsky, N. J. (2014). The rise of oxygen in Earth's early ocean and atmosphere. *Nature*, 506(7488), 307–315. <https://doi.org/10.1038/nature13068>
- Ma, R., S epulcre, S., Licari, L., Bassinot, F., Liu, Z., Tisn erat-Laborde, N., et al. (2019). Changes in Intermediate Circulation in the Bay of Bengal Since the Last Glacial Maximum as Inferred From Benthic Foraminifera Assemblages and Geochemical Proxies. *Geochemistry, Geophysics, Geosystems*, 20(3), 1592–1608. <https://doi.org/10.1029/2018GC008179>
- Ma, R., S epulcre, S., Bassinot, F., Haurine, F., Tisn erat-Laborde, N., & Colin, C. (2020). North Indian Ocean Circulation Since the Last Deglaciation as Inferred From New Elemental Ratio Records for Benthic Foraminifera *Hoeglundina elegans*. *Paleoceanography and Paleoclimatology*, 35(6), e2019PA003801. <https://doi.org/10.1029/2019PA003801>
- Ma, R., S epulcre, S., Licari, L., Haurine, F., Bassinot, F., Yu, Z., & Colin, C. (2022). Changes in productivity and intermediate circulation in the northern Indian Ocean since the last deglaciation: new insights from benthic foraminiferal Cd/Ca records and benthic assemblage analyses. *Climate of the Past*, 18(8), 1757–1774. <https://doi.org/10.5194/cp-18-1757-2022>
- Macko, S. A., & Estep, M. L. F. (1984). Microbial alteration of stable nitrogen and carbon isotopic compositions of organic matter. *Organic Geochemistry*, 6, 787–790. [https://doi.org/10.1016/0146-6380\(84\)90100-1](https://doi.org/10.1016/0146-6380(84)90100-1)

- Madhupratap, M., Kumar, S. P., Bhattathiri, P. M. A., Kumar, M. D., Raghukumar, S., Nair, K. K. C., & Ramaiah, N. (1996). Mechanism of the biological response to winter cooling in the northeastern Arabian Sea. *Nature*, *384*(6609), 549–552. <https://doi.org/10.1038/384549a0>
- Mahesh, B. S., & Banakar, V. K. (2014). Change in the intensity of low-salinity water inflow from the Bay of Bengal into the Eastern Arabian Sea from the Last Glacial Maximum to the Holocene: Implications for monsoon variations. *Palaeogeography, Palaeoclimatology, Palaeoecology*, *397*, 31–37. <https://doi.org/10.1016/j.palaeo.2013.05.024>
- McCartney, M. S., & Talley, L. D. (1982). The Subpolar Mode Water of the North Atlantic Ocean. *Journal of Physical Oceanography*, *12*(11), 1169–1188. [https://doi.org/10.1175/1520-0485\(1982\)012<1169:TSMWOT>2.0.CO;2](https://doi.org/10.1175/1520-0485(1982)012<1169:TSMWOT>2.0.CO;2)
- McCreary, J. P., Yu, Z., Hood, R. R., Vinayachandran, P. N., Furue, R., Ishida, A., & Richards, K. J. (2013). Dynamics of the Indian-Ocean oxygen minimum zones. *Progress in Oceanography*, *112–113*, 15–37. <https://doi.org/10.1016/j.pocean.2013.03.002>
- Meyers, P. A. (1994). Preservation of elemental and isotopic source identification of sedimentary organic matter. *Chemical Geology*, *114*(3), 289–302. [https://doi.org/10.1016/0009-2541\(94\)90059-0](https://doi.org/10.1016/0009-2541(94)90059-0)
- Montoya, J. P. (1994). Nitrogen Isotope Fractionation in the Modern Ocean: Implications for the Sedimentary Record. In R. Zahn, T. F. Pedersen, M. A. Kaminski, & L. Labeyrie (Eds.), *Carbon Cycling in the Glacial Ocean: Constraints on the Ocean's Role in Global Change* (pp. 259–279). Berlin, Heidelberg: Springer. [https://doi.org/10.1007/978-3-642-78737-9\\_11](https://doi.org/10.1007/978-3-642-78737-9_11)
- Morrison, J. M., Codispoti, L. A., Gaurin, S., Jones, B., Manghnani, V., & Zheng, Z. (1998). Seasonal variation of hydrographic and nutrient fields during the US JGOFS Arabian Sea Process Study. *Deep Sea Research Part II: Topical Studies in Oceanography*, *45*(10), 2053–2101. [https://doi.org/10.1016/S0967-0645\(98\)00063-0](https://doi.org/10.1016/S0967-0645(98)00063-0)
- Naidu, P. D., Singh, A. D., Ganeshram, R., & Bharti, S. K. (2014). Abrupt climate-induced changes in carbonate burial in the Arabian Sea: Causes and consequences.

- Geochemistry, Geophysics, Geosystems*, 15(4), 1398–1406.  
<https://doi.org/10.1002/2013GC005065>
- Naik, D. K., Saraswat, R., Lea, D. W., Kurtarkar, S. R., & Mackensen, A. (2017). Last glacial-interglacial productivity and associated changes in the eastern Arabian Sea. *Palaeogeography, Palaeoclimatology, Palaeoecology*, 483, 147–156.  
<https://doi.org/10.1016/j.palaeo.2016.07.014>
- Naik, S. N., & Naik, S. S. (2022). Glacial–interglacial contrast in deep-water  $\delta^{13}\text{C}$  of the Arabian Sea. *Journal of Earth System Science*, 131(1), 49.  
<https://doi.org/10.1007/s12040-021-01796-8>
- Naqvi, S. W. A. (1994). Denitrification processes in the Arabian Sea. *Journal of Earth System Science*, 103(2), 279–300. <https://doi.org/10.1007/BF02839539>
- Naqvi, S. W. A., Naik, H., Pratihary, A., D'Souza, W., Narvekar, P. V., Jayakumar, D. A., et al. (2006). Coastal versus open-ocean denitrification in the Arabian Sea, 13.
- Naqvi, S. W. A., Bange, H. W., Farías, L., Monteiro, P. M. S., Scranton, M. I., & Zhang, J. (2010). Marine hypoxia/anoxia as a source of  $\text{CH}_4$  and  $\text{N}_2\text{O}$ . *Biogeosciences*, 7(7), 2159–2190. <https://doi.org/10.5194/bg-7-2159-2010>
- Norris, R. D., Turner, S. K., Hull, P. M., & Ridgwell, A. (2013). Marine Ecosystem Responses to Cenozoic Global Change. *Science*, 341(6145), 492–498.  
<https://doi.org/10.1126/science.1240543>
- Olson, D. B., Hitchcock, G. L., Fine, R. A., & Warren, B. A. (1993). Maintenance of the low-oxygen layer in the central Arabian Sea. *Deep Sea Research Part II: Topical Studies in Oceanography*, 40(3), 673–685. [https://doi.org/10.1016/0967-0645\(93\)90051-N](https://doi.org/10.1016/0967-0645(93)90051-N)
- Oschlies, A., Schulz, K. G., Riebesell, U., & Schmittner, A. (2008). Simulated 21st century's increase in oceanic suboxia by  $\text{CO}_2$ -enhanced biotic carbon export. *Global Biogeochemical Cycles*, 22(4). <https://doi.org/10.1029/2007GB003147>
- Oschlies, A., Duteil, O., Getzlaff, J., Koeve, W., Landolfi, A., & Schmidtko, S. (2017). Patterns of deoxygenation: sensitivity to natural and anthropogenic drivers. *Philosophical*

*Transactions of the Royal Society A: Mathematical, Physical and Engineering Sciences*, 375(2102), 20160325. <https://doi.org/10.1098/rsta.2016.0325>

- Oschlies, A., Brandt, P., Stramma, L., & Schmidtko, S. (2018). Drivers and mechanisms of ocean deoxygenation. *Nature Geoscience*, 11(7), 467–473. <https://doi.org/10.1038/s41561-018-0152-2>
- Paulmier, A., & Ruiz-Pino, D. (2009). Oxygen minimum zones (OMZs) in the modern ocean. *Progress in Oceanography*, 80(3), 113–128. <https://doi.org/10.1016/j.pocean.2008.08.001>
- Pichevin, L., Bard, E., Martinez, P., & Billy, I. (2007). Evidence of ventilation changes in the Arabian Sea during the late Quaternary: Implication for denitrification and nitrous oxide emission. *Global Biogeochemical Cycles*, 21(4). <https://doi.org/10.1029/2006GB002852>
- Piontkovski, S., & Al-Oufi, H. S. (2015). The Omani shelf hypoxia and the warming Arabian Sea. *International Journal of Environmental Studies*, 72. <https://doi.org/10.1080/00207233.2015.1012361>
- Podder, J., Lin, J., Sun, W., Botis, S. M., Tse, J., Chen, N., et al. (2017). Iodate in calcite and vaterite: Insights from synchrotron X-ray absorption spectroscopy and first-principles calculations. *Geochimica et Cosmochimica Acta*, 198, 218–228. <https://doi.org/10.1016/j.gca.2016.11.032>
- Prasad, T. G. (1997). Annual and seasonal mean buoyancy fluxes for the tropical Indian Ocean. Retrieved from <https://drs.nio.res.in/drs/handle/2264/2103>
- Prasad, T. G., Ikeda, M., & Kumar, S. P. (2001). Seasonal spreading of the Persian Gulf Water mass in the Arabian Sea. *Journal of Geophysical Research: Oceans*, 106(C8), 17059–17071. <https://doi.org/10.1029/2000JC000480>
- Prasanna Kumar, S., & Narvekar, J. (2005). Seasonal variability of the mixed layer in the central Arabian Sea and its implication on nutrients and primary productivity. *Deep Sea Research Part II: Topical Studies in Oceanography*, 52(14), 1848–1861. <https://doi.org/10.1016/j.dsr2.2005.06.002>

- Queste, B. Y., Vic, C., Heywood, K. J., & Piontkovski, S. A. (2018). Physical Controls on Oxygen Distribution and Denitrification Potential in the North West Arabian Sea. *Geophysical Research Letters*, 45(9), 4143–4152. <https://doi.org/10.1029/2017GL076666>
- Rabalais, N., Cai, W.-J., Carstensen, J., Conley, D., Fry, B., Hu, X., et al. (2014). Eutrophication-Driven Deoxygenation in the Coastal Ocean. *Oceanography*, 27(1), 172–183. <https://doi.org/10.5670/oceanog.2014.21>
- von Rad, U., Schaaf, M., Michels, K. H., Schulz, H., Berger, W. H., & Sirocko, F. (1999). A 5000-yr Record of Climate Change in Varved Sediments from the Oxygen Minimum Zone off Pakistan, Northeastern Arabian Sea. *Quaternary Research*, 51(1), 39–53. <https://doi.org/10.1006/qres.1998.2016>
- Ramesh, R., & Sarin, M. M. (1992). Stable isotope study of the Ganga (Ganges) river system. *Journal of Hydrology*, 139(1), 49–62. [https://doi.org/10.1016/0022-1694\(92\)90194-Z](https://doi.org/10.1016/0022-1694(92)90194-Z)
- Rashid, H., Gourlan, A. T., Marche, B., Sheppard, K., & Khélifi, N. (2019). Changes in Indian Summer Monsoon Using Neodymium (Nd) Isotopes in the Andaman Sea During the Last 24,000 years. *Earth Systems and Environment*, 3(2), 241–253. <https://doi.org/10.1007/s41748-019-00105-0>
- Rathburn, A. E., Willingham, J., Ziebis, W., Burkett, A. M., & Corliss, B. H. (2018). A New biological proxy for deep-sea paleo-oxygen: Pores of epifaunal benthic foraminifera. *Scientific Reports*, 8(1), 9456. <https://doi.org/10.1038/s41598-018-27793-4>
- Ravishankara, A. R., Daniel, J. S., & Portmann, R. W. (2009). Nitrous Oxide (N<sub>2</sub>O): The Dominant Ozone-Depleting Substance Emitted in the 21st Century. *Science*, 326(5949), 123–125. <https://doi.org/10.1126/science.1176985>
- Reichart, G. J., Lourens, L. J., & Zachariasse, W. J. (1998). Temporal variability in the northern Arabian Sea oxygen minimum zone (OMZ) during the last 225,000 years. *Paleoceanography*, 13(6), 607–621. <https://doi.org/10.1029/98PA02203>
- Resplandy, L., Lévy, M., Bopp, L., Echevin, V., Pous, S., Sarma, V. V. S. S., & Kumar, D. (2012). Controlling factors of the oxygen balance in the Arabian Sea's OMZ. *Biogeosciences*, 9(12), 5095–5109. <https://doi.org/10.5194/bg-9-5095-2012>

- Rixen, T., Cowie, G., Gaye, B., Goes, J., do Rosário Gomes, H., Hood, R. R., et al. (2020). Reviews and syntheses: Present, past, and future of the oxygen minimum zone in the northern Indian Ocean. *Biogeosciences*, 17(23), 6051–6080. <https://doi.org/10.5194/bg-17-6051-2020>
- Robinson, R. A. J., Bird, M. I., Oo, N. W., Hoey, T. B., Aye, M. M., Higgitt, D. L., et al. (2007). The Irrawaddy River Sediment Flux to the Indian Ocean: The Original Nineteenth-Century Data Revisited. *The Journal of Geology*, 115(6), 629–640. <https://doi.org/10.1086/521607>
- Robinson, R. S., Kienast, M., Albuquerque, A. L., Altabet, M., Contreras, S., Holz, R. D. P., et al. (2012). A review of nitrogen isotopic alteration in marine sediments. *Paleoceanography*, 27(4). <https://doi.org/10.1029/2012PA002321>
- Rue, E. L., Smith, G. J., Cutter, G. A., & Bruland, K. W. (1997). The response of trace element redox couples to suboxic conditions in the water column. *Deep Sea Research Part I: Oceanographic Research Papers*, 44(1), 113–134. [https://doi.org/10.1016/S0967-0637\(96\)00088-X](https://doi.org/10.1016/S0967-0637(96)00088-X)
- Sarkar, A., Ramesh, R., Bhattacharya, S. K., & Rajagopalan, G. (1990). Oxygen isotope evidence for a stronger winter monsoon current during the last glaciation. *Nature*, 343(6258), 549–551. <https://doi.org/10.1038/343549a0>
- Schiebel, R., & Hemleben, C. (2017). *Planktic Foraminifers in the Modern Ocean*. Berlin, Heidelberg: Springer. <https://doi.org/10.1007/978-3-662-50297-6>
- Schmidtko, S., Stramma, L., & Visbeck, M. (2017). Decline in global oceanic oxygen content during the past five decades. *Nature*, 542(7641), 335–339. <https://doi.org/10.1038/nature21399>
- Schmittner, A., Oschlies, A., Matthews, H. D., & Galbraith, E. D. (2008). Future changes in climate, ocean circulation, ecosystems, and biogeochemical cycling simulated for a business-as-usual CO<sub>2</sub> emission scenario until year 4000 AD. *Global Biogeochemical Cycles*, 22(1). <https://doi.org/10.1029/2007GB002953>

- Schott, F. A., & McCreary, J. P. (2001). The monsoon circulation of the Indian Ocean. *Progress in Oceanography*, 51(1), 1–123. [https://doi.org/10.1016/S0079-6611\(01\)00083-0](https://doi.org/10.1016/S0079-6611(01)00083-0)
- Shepherd, J. G., Brewer, P. G., Oschlies, A., & Watson, A. J. (2017). Ocean ventilation and deoxygenation in a warming world: introduction and overview. *Philosophical Transactions of the Royal Society A: Mathematical, Physical and Engineering Sciences*, 375(2102), 20170240. <https://doi.org/10.1098/rsta.2017.0240>
- Sigman, D. M., & Fripiat, F. (2019). Nitrogen Isotopes in the Ocean. In *Encyclopedia of Ocean Sciences* (pp. 263–278). Elsevier. <https://doi.org/10.1016/B978-0-12-409548-9.11605-7>
- Sigman, D. M., Karsh, K. L., & Casciotti, K. L. (2009). Nitrogen Isotopes in the Ocean. In J. H. Steele (Ed.), *Encyclopedia of Ocean Sciences (Second Edition)* (pp. 40–54). Oxford: Academic Press. <https://doi.org/10.1016/B978-012374473-9.00632-9>
- Sigman, D. M., Hain, M. P., & Haug, G. H. (2010). The polar ocean and glacial cycles in atmospheric CO<sub>2</sub> concentration. *Nature*, 466(7302), 47–55. <https://doi.org/10.1038/nature09149>
- Singh, A. D., Rai, A. K., Verma, K., Das, S., & Bharti, S. K. (2015). Benthic foraminiferal diversity response to the climate induced changes in the eastern Arabian Sea oxygen minimum zone during the last 30 ka BP. *Quaternary International*, 374, 118–125. <https://doi.org/10.1016/j.quaint.2014.11.052>
- Smerdon, J. E. (2017). What was Earth's climate like before we were measuring it? *Significance*, 14(1), 24–29. <https://doi.org/10.1111/j.1740-9713.2017.00999.x>
- Somes, C. J., Schmittner, A., Muglia, J., & Oschlies, A. (2017). A Three-Dimensional Model of the Marine Nitrogen Cycle during the Last Glacial Maximum Constrained by Sedimentary Isotopes. *Frontiers in Marine Science*, 4. <https://doi.org/10.3389/fmars.2017.00108>
- Southon, J., Kashgarian, M., Fontugne, M., Metivier, B., & Yim, W. W.-S. (2002). Marine Reservoir Corrections for the Indian Ocean and Southeast Asia. *Radiocarbon*, 44(1), 167–180. <https://doi.org/10.1017/S0033822200064778>

- Stainbank, S., Kroon, D., Rüggeberg, A., Raddatz, J., Leau, E. S. de, Zhang, M., & Spezzaferri, S. (2019). Controls on planktonic foraminifera apparent calcification depths for the northern equatorial Indian Ocean. *PLOS ONE*, *14*(9), e0222299. <https://doi.org/10.1371/journal.pone.0222299>
- Stramma, L., Johnson, G. C., Sprintall, J., & Mohrholz, V. (2008). Expanding Oxygen-Minimum Zones in the Tropical Oceans. *Science*, *320*(5876), 655–658. <https://doi.org/10.1126/science.1153847>
- Stramma, L., Schmidtko, S., Levin, L. A., & Johnson, G. C. (2010). Ocean oxygen minima expansions and their biological impacts. *Deep Sea Research Part I: Oceanographic Research Papers*, *57*(4), 587–595. <https://doi.org/10.1016/j.dsr.2010.01.005>
- Stramma, L., Oschlies, A., & Schmidtko, S. (2012). Mismatch between observed and modeled trends in dissolved upper-ocean oxygen over the last 50 yr. *Biogeosciences*, *9*(10), 4045–4057. <https://doi.org/10.5194/bg-9-4045-2012>
- Stuiver, M., & Braziunas, T. F. (1993). Modeling Atmospheric  $^{14}\text{C}$  Influences and  $^{14}\text{C}$  Ages of Marine Samples to 10,000BC. *Radiocarbon*, *35*(1), 137–189. <https://doi.org/10.1017/S0033822200013874>
- Stuiver, M., Reimer, P. J., & Reimer, R. W. (2021). CALIB (Version 8.2). Retrieved from <http://calib.org>, accessed 2021-8-3
- Suess, E. (1980). Particulate organic carbon flux in the oceans—surface productivity and oxygen utilization. *Nature*, *288*(5788), 260–263. <https://doi.org/10.1038/288260a0>
- Suthhof, A., Ittekkot, V., & Gaye-Haake, B. (2001). Millennial-scale oscillation of denitrification intensity in the Arabian Sea during the Late Quaternary and its potential influence on atmospheric  $\text{N}_2\text{O}$  and global climate. *Global Biogeochemical Cycles*, *15*(3), 637–649. <https://doi.org/10.1029/2000GB001337>
- Sverdrup, H. U. (1938). On the Explanation of the Oxygen Minima and Maxima in the Oceans1). *ICES Journal of Marine Science*, *13*(2), 163–172. <https://doi.org/10.1093/icesjms/13.2.163>
- Talley, L. D. (2011). *Descriptive Physical Oceanography: An Introduction*. Academic Press.

- Tomczak, M., & Godfrey, J. S. (2003). *Regional Oceanography: An Introduction*. Daya Books.
- Truesdale, V. W., & Bailey, G. W. (2000). Dissolved Iodate and Total Iodine During an Extreme Hypoxic Event in the Southern Benguela System. *Estuarine, Coastal and Shelf Science*, 50(6), 751–760. <https://doi.org/10.1006/ecss.2000.0609>
- Truesdale, V. W., Bale, A. J., & Woodward, E. M. S. (2000). The meridional distribution of dissolved iodine in near-surface waters of the Atlantic Ocean. *Progress in Oceanography*, 45(3), 387–400. [https://doi.org/10.1016/S0079-6611\(00\)00009-4](https://doi.org/10.1016/S0079-6611(00)00009-4)
- Van Raden, U. J., Groeneveld, J., Raitzsch, M., & Kucera, M. (2011). Mg/Ca in the planktonic foraminifera *Globorotalia inflata* and *Globigerinoides bulloides* from Western Mediterranean plankton tow and core top samples. *Marine Micropaleontology*, 78(3–4), 101–112. <https://doi.org/10.1016/j.marmicro.2010.11.002>
- Vaquer-Sunyer, R., & Duarte, C. M. (2008). Thresholds of hypoxia for marine biodiversity. *Proceedings of the National Academy of Sciences*, 105(40), 15452–15457. <https://doi.org/10.1073/pnas.0803833105>
- Vinayachandran, P. N., Masumoto, Y., Mikawa, T., & Yamagata, T. (1999). Intrusion of the Southwest Monsoon Current into the Bay of Bengal. *Journal of Geophysical Research: Oceans*, 104(C5), 11077–11085. <https://doi.org/10.1029/1999JC900035>
- Wacker, L., Němec, M., & Bourquin, J. (2010). A revolutionary graphitisation system: Fully automated, compact and simple. *Nuclear Instruments and Methods in Physics Research Section B: Beam Interactions with Materials and Atoms*, 268(7), 931–934. <https://doi.org/10.1016/j.nimb.2009.10.067>
- Wacker, L., Fülöp, R.-H., Hajdas, I., Molnár, M., & Rethemeyer, J. (2013). A novel approach to process carbonate samples for radiocarbon measurements with helium carrier gas. *Nuclear Instruments and Methods in Physics Research Section B: Beam Interactions with Materials and Atoms*, 294, 214–217. <https://doi.org/10.1016/j.nimb.2012.08.030>
- Wang, B., & Ding, Q. (2008). Global monsoon: Dominant mode of annual variation in the tropics. *Dynamics of Atmospheres and Oceans*, 44(3), 165–183. <https://doi.org/10.1016/j.dynatmoce.2007.05.002>

- Ward, B. B. (2008). Chapter 5 - Nitrification in Marine Systems. In D. G. Capone, D. A. Bronk, M. R. Mulholland, & E. J. Carpenter (Eds.), *Nitrogen in the Marine Environment (Second Edition)* (pp.199–261). San Diego: Academic Press. <https://doi.org/10.1016/B978-0-12-372522-6.00005-0>
- Watson, A. J. (2016). Oceans on the edge of anoxia. *Science*, *354*(6319), 1529–1530. <https://doi.org/10.1126/science.aaj2321>
- Winkelbauer, H. A. (2022, October). *Planktic foraminiferal I/Ca ratios as a proxy for past seawater oxygen concentrations* (Thesis). Heriot-Watt University. Retrieved from <https://www.ros.hw.ac.uk/handle/10399/4773>
- Winkelbauer, H. A., Cordova-Rodriguez, K., Reyes-Macaya, D., Scott, J., Glock, N., Lu, Z., et al. (2021). Foraminifera Iodine to Calcium Ratios: Approach and Cleaning. *Geochemistry, Geophysics, Geosystems*, *22*(11), e2021GC009811. <https://doi.org/10.1029/2021GC009811>
- Winkelbauer, H. A., Hoogakker, B. A. A., Chance, R. J., Davis, C. V., Anthony, C. J., Bischoff, J., et al. (2023). Planktic foraminifera iodine/calcium ratios from plankton tows. *Frontiers in Marine Science*, *10*. Retrieved from <https://www.frontiersin.org/articles/10.3389/fmars.2023.1095570>
- Wong, G. T. F., & Brewer, P. G. (1977). The marine chemistry of iodine in anoxic basins. *Geochimica et Cosmochimica Acta*, *41*(1), 151–159. [https://doi.org/10.1016/0016-7037\(77\)90195-8](https://doi.org/10.1016/0016-7037(77)90195-8)
- Wright, J., Konwar, K., & Hallam, S. (2012). Microbial ecology of expanding oxygen minimum zones. *Nature Reviews. Microbiology*, *10*, 381–94. <https://doi.org/10.1038/nrmicro2778>
- You, Y. (1998). Intermediate water circulation and ventilation of the Indian Ocean derived from water-mass contributions. *Journal of Marine Research*, *56*(5), 1029–1067. <https://doi.org/10.1357/002224098765173455>
- Yu, Z., Colin, C., Ma, R., Meynadier, L., Wan, S., Wu, Q., et al. (2018). Antarctic Intermediate Water penetration into the Northern Indian Ocean during the last deglaciation. *Earth and Planetary Science Letters*, *500*, 67–75. <https://doi.org/10.1016/j.epsl.2018.08.006>

- Zehr, J. P., & Capone, D. G. (2020). Changing perspectives in marine nitrogen fixation. *Science*, 368(6492). <https://doi.org/10.1126/science.aay9514>
- Zhang, X., Sigman, D. M., Morel, F. M. M., & Kraepiel, A. M. L. (2014). Nitrogen isotope fractionation by alternative nitrogenases and past ocean anoxia. *Proceedings of the National Academy of Sciences*, 111(13), 4782–4787. <https://doi.org/10.1073/pnas.1402976111>
- Zhou, Xiaoli, Thomas, E., Rickaby, R. E. M., Winguth, A. M. E., & Lu, Z. (2014). I/Ca evidence for upper ocean deoxygenation during the PETM. *Paleoceanography*, 29(10), 964–975. <https://doi.org/10.1002/2014PA002702>
- Zhou, Xiaoli, Hess, A. V., Bu, K., Sagawa, T., & Rosenthal, Y. (2022). Simultaneous Determination of I/Ca and Other Elemental Ratios in Foraminifera: Comparing Results From Acidic and Basic Solutions. *Geochemistry, Geophysics, Geosystems*, 23(11), e2022GC010660. <https://doi.org/10.1029/2022GC010660>
- Zhou, Xinquan, Duchamp-Alphonse, S., Kageyama, M., Bassinot, F., Doressoundiram, F., & Kissel, C. (2022). Variations of Primary Productivity in the Northwestern Arabian Sea During the Last 23,000 Years and Their Paleoclimatological Implications. *Paleoceanography and Paleoclimatology*, 37(10), e2022PA004453. <https://doi.org/10.1029/2022PA004453>



## List of Publications

- **Rai, D. K.**, Kumar, J., Qasim. A., Kumar, S., Bhushan, R., & Singh, A. Glacial – interglacial oxygen variability in the Arabian Sea (under preparation).
- **Rai, D. K.**, Kumar, S., Bhushan, R., & Singh, A. Glacial – interglacial variations in the nitrogen cycle in the Arabian Sea (under preparation).
- Saxena, H., Sahoo, D., Nazirahmed, S., **Rai, D. K.**, Khan, M. A., Sharma, N., Kumar, S., & Singh, A. (2022). Contribution of Carbon Fixation Toward Carbon Sink in the Ocean Twilight Zone. *Geophysical Research Letters*, 49(18), e2022GL099044. <https://doi.org/10.1029/2022GL099044>
- Saxena, H., Sahoo, D., Nazirahmed, S., Sharma, N., **Rai, D. K.**, Kumar, S., & Singh, A. (2024). Winter Convective Mixing Mediating Coupling of N-Gain and -Loss in the Arabian Sea. *Journal of Geophysical Research: Oceans*, 129(5), e2023JC020839. <https://doi.org/10.1029/2023JC020839>
- Sahoo, D., Saxena, H., Nazirahmed, S., Khan, M. A., **Rai, D. K.**, Sharma, N., Kumar, S., Sudheer, A. K., Bhushan, R., Singh, A. (2023). Winter convective mixing regulates the C:N:P ratios in the ocean. *Limnology and Oceanography* (accepted).

## Presentations at Conferences

- **Rai, D. K.**, Kumar, S., Bhushan, R., & Singh, A. Glacial - Interglacial variations of biogeochemical processes in the Arabian Sea. AGU fall meeting -2022.
- **Rai, D. K.**, Kumar, S., Bhushan, R., & Singh, A. Glacial - Interglacial variations in the intensity of denitrification in the south-eastern Arabian Sea. Frontiers in Geoscience Research (FGRC-2023) (*received best poster award*).